Molecular frame photoelectron angular distributions from resonant two-photon ionization of molecules in gas phase and in helium nanodroplets

PhD Thesis

Jacqueline Arlt

Supervisor: Henrik Stapelfeldt
Department of Chemistry
Aarhus University
April 2020

Acknowledgement

First and foremost, I would like to thank my supervisor Henrik Stapelfeldt for giving me the opportunity to join his group and work on a great and exciting research project. In Danish, a supervisor is called a "vejleder" and that's what Henrik does: He leads the way by sharing his vast experience and discussing new ideas of what to try next in the lab. His excitement for research is unprecedented and inspiring.

I am grateful I could rely on the expertise of Jan Thøgerson for any issues with the laser system. You know a laser is really beyond repair if Jan does not know a way to fix it.

I would like to thank Benjamin Shepperson for sharing his expertise on helium droplets and on the use of Autodesk Inventor. The many hours we spent together on building the experimental setup flew by quickly.

Lars Christiansen has been a great help on building parts of the laser setup. I am especially thankful to him for discussions on the conduct of the naphthalene and aniline experiments, even though he had already left the group.

I would also like to thank Adam Chatterley for joining me in the lab for building parts of the optical setup and conducting experiments. I also thank him for proof-reading large parts of this manuscript. I thank James Pickering for his comments on chapter 3.

Jeppe Mikkelsen and Erik Pedersen have manufactured a lot of the parts used to build the vacuum setup. I would like to thank them for a good collaboration and also for their insights on manufacturing. I thank Torben Thomsen and John Andersen for helpful discussions on vacuum setup design.

The good atmosphere made Femtolab a great place to work and I enjoyed our canoe trips, pie at π o'clock, Christmas symposiums and lunch discussions. Among fruitful discussions about scientific topics, it has always been a pleasure to converse also on subjects like your favourite greek letter. For this good atmosphere, I would like to thank in addition to the members I have already mentioned: Mette Rasmussen, Constant Schouder, Anders Jørgensen, Bjarke Hübschmann, Marlene Madsen, Mia Baastrup, Signe Thorsen, Dorte Plauborg, Mikael Alstrup, Hagbart Frandsen, Albert Munoz, Lorenz Kranabetter, Henrik Kristensen and Simon Albrechtsen.

I thank Paul Hockett for the ePolyScat calculations, sharing his ePSproc code and many discussions on their interpretation and use.

Furthermore, I would like to thank the ASPIRE network. It has been a privilege to be part of this network and I benefited from the vast experience accumulated here, as well as the stimulating discussions emerging on each ASPIRE meeting. Especially, I would like to thank Katharine Reid for receiving me for a secondment in her group in Nottingham. I very much enjoyed the collaboration and I learnt a lot about MFPADs. On the same account, I would like to thank Dhirendra Singh and James Thompson.

I am grateful to my parents for their love and support throughout my life. Last but not least, I would like to thank Vasco Wiering for cheering me up while I was recovering from the concussion – and the last decade.

This research has received funding from the European Union's Horizon 2020 research and innovation programme under the Marie Sklodowska-Curie grant agreement No 674960.

Résumé

English

The studies in my PhD thesis focus on molecular frame photoelectron angular distributions, realized by recording the emission direction of electrons following resonant two-photon ionization of molecules that have been fixed-in-space by laser-induced alignment techniques. Studies were conducted on both isolated molecules in the gas phase and molecules embedded in helium nanodroplets. To make the studies possible, I redesigned and reconstructed a vacuum setup allowing experiments on both isolated molecules and molecules in helium droplets.

The gas phase experiments concerned aniline and naphthalene molecules. The molecules were aligned either one-dimensionally or three-dimensionally with a moderately strong, non-resonant laser pulse. At the peak of this pulse, where the degree of aligment was strongest, the molecules were ionized through resonant two-photon absorption by a 6 ps long UV probe pulse.

For aniline, a mild anisotropy in the electron emission direction along the linearly polarized probe pulse is strongly enhanced when the molecules are one-dimensionally aligned with their C-N axis along the probe polarization. The experimental observations are rationalized by numerical calculations using the ePolyScat method. For naphthalene, the angular distribution of the photoelectrons changes from essentially isotropic into a distinct four-fold structure upon one- or three-dimensional alignment. These observations shows that electron emission is suppressed in the molecular plane of naphthalene.

Similar experiments were conducted on aniline molecules embedded in helium nanodroplets motivated by recent findings showing that the sharp alignment at the peak of the alignment pulse can be retained in a window of few picoseconds after rapid truncation of the alignment pulse. In this window, the intensity of the alignment pulse is reduced by 2-3 orders of magnitude and the unwanted perturbation of the ionization process by the probe pulse, observed for the gas phase molecules, should therefore be eliminated.

I did manage to complete experiments, but was challenged by a very high contribution to the electron signal from ionization of unsolvated molecules, i.e molecules that had diffused directly to the laser interaction point rather than being picked up by the droplets. Due to very limited time available for these measurements, it was not possible to improve the experimental conditions. Thus, it was not possible to conclude if molecules aligned almost field-free inside helium nanodroplets allow the observation of molecular frame photoelectron angular distributions.

Danish

Min ph.d. afhandling omhandler fotoelektroners vinkelfordelinger målt i det molekylfaste koordinatsystem. I praksis blev det opnået ved at detektere udsendelsesretningen af elektroner stammende fra resonant to-foton ionisation af molekyler, som var alignede ved hjælp af laserbaserede metoder udviklet i Femtolab. Jeg undersøgte både isolerede gasfase molekyler og molekyler indsat i helium nanodråber. For at kunne udføre målingerne omdesignede og ombyggede jeg et vakuum-instrument, hvori det er muligt både at studere isolerede molekyler og molekyler indsat i helium nanodråber. I gasfase eksperimenterne undersøgte jeg anilin og naftalen molekyler. Disse molekyler blev alignede ved hjælp af en tilpas stærk laserpuls med en bølgelængde på 800 nm. Alignment betyder, at de molekylære akser fastholdes langs akser i laboratoriet defineret af polarisationsgeometrien af alignmentpulsen. En 6 ps lang ultraviolet probepuls blev herefter sendt ind på molekylerne for at ionisere dem som følge af resonant absorption af to fotoner. Probepulsen blev sendt på det tidspunkt, hvor alignmentpulsen var stærkest, fordi der er det tidspunkt, hvor graden af alignment er højest. For tilfældigt orienterede anilin molekyler observerede jeg, at elektronerne udviste en svag anisotropi langs polarisationsretningen af den lineært polarisede probe puls. Denne anisotropi øgedes markant, når molekylerne var alignede med deres CN axis langs probepuls polarisationen. Målingerne blev sammenlignet med numeriske beregninger via ePolyScat metoden, og jeg fandt god overensstemmelse. For naftalen observerede jeg, at de næsten isotrope vinkelfordelinger, målt for tilfældigt orienterede molekyler, ændredes til en slående 4-sløjfe struktur svarende til, at elektron udsendelse undertrykkes i molekylets plan. Til allersidst i mit projekt gennemførte jeg tilsvarende ionisationseksperimenter på molekyler indsat i helium nanodråber. Motivationen for sådanne målinger er, at nye eksperimenter Femtolab har vist, at molekyler i heliumdråber kan alignes endnu bedre end i gasfase, og at det desuden er muligt at fastholde molekylerne stærkt alignede i cirka 10 picosekunder efter alignmentpulsen slukkes abrupt. I denne 10 ps periode er alignmentpulsens intensitet reduceret med over en faktor 100, og dermed undgår man, at alignmentpulsen perturberer den to-foton ionisation, som probepulsen inducerer. I gasfase målingerne, hvor det ikke er muligt at skabe et sådant felt-fri alignment vindue, observerede jeg, at alignmentpulsen forårsagede en markant perturbation af fotoelektronspektret. Det lykkedes mig at udføre målingerne på molekyler i heliumdråberne. Uheldigvis var der en meget stor baggrund af elektroner fra ionisation af molekyler, der var diffunderet direkte til laser vekslevirkningspunktet snarere end at blive opsamlet af heliumdråberne. På grund af tidsmangel kunne jeg ikke nå at forbedre de eksperimentelle betingelser, og det var således ikke muligt for mig at afgøre om, det er muligt at observere

vinkelfordelinger i det molekylfaste koordinatsystem ved at bruge næsten feltfri alignede molekyler i helium nanodråber.

Abbreviations

- AR – anti-reflective
- ASME – American Society of Mechanical Engineers
- ASPIRE – Angular Studies of Photoelectron in Innovative Research Environments
- a.u. – arbitrary units
- B3LYP – Becke, 3-parameter, Lee–Yang–Parr
- BBO – barium borate
- FWHM – full width at half maximum
- HeNe – helium-neon
- HF – Hartree-Fock
- HWP – half-wave plate
- IR – infrared
- GAMESS – General Atomic and Molecular Electronic Structure System
- KDP – potassium dihydrogen phosphate
- LF – laboratory frame
- LFPAD – laboratory frame photoelectron angular distribution
- MCP – microchannel plate
- MF – molecular frame
- MFPAD – molecular frame photoelectron angular distribution

- MFPMD – molecular frame photoelectron momentum distribution
- MPA – most polarizable axis
- OPA – optical parametric amplifier
- POP – polar onion peeling
- QWP – quarter-wave plate
- PAD – photoelectron angular distribution
- PES – photoelectron kinetic energy spectrum
- PMD – photoelectron momentum distribution
- R2PI – resonant two-photon ionization
- REMPI – resonance enhanced multiphoton ionization
- SFG – sum frequency generation
- SHG – second harmonic generation
- TFP – thin film polarizer
- UHV – ultra high vacuum
- UV – ultraviolet
- VMI – velocity map imaging
- VUV – vacuum ultraviolet

List of Publications

The work of this PhD project has led to the following publications and manuscripts:

J. Arlt, D. Singh, J. O. F. Thompson, A. S. Chatterley, P. Hockett, H. Stapelfeldt, K. L. Reid. "Photoelectron angular distributions from resonant two-photon ionization of adiabatically aligned aniline and naphthalene molecules", *working title, in preparation*, (2020)

Contents

Acknowledgement **i**

Résumé **iii**
English iii
Danish v

Abbreviations **vii**

List of Publications **ix**

Contents **x**

1 Introduction **1**

2 Background **3**
2.1 Helium nanodroplets 3
2.1.1 Droplet formation 4
2.1.2 Pickup process 6
2.1.3 Applications of helium droplets 8
2.1.4 Studies of helium droplets 10
2.2 Alignment 14
2.2.1 Theoretical description 15
2.2.2 Adiabatic alignment 17
2.2.3 Estimating the achievable alignment 18
2.2.4 Alignment in helium nanodroplets using truncated pulses 19
2.2.5 Non-adiabatic alignment 20
2.3 MFPADs 22
2.3.1 Theoretical motivation 23
2.3.2 MFPADs measured from electrons and ions in coincidence 24
2.3.3 Midrange photon energies (XUV) 25
2.3.4 High photon energies (XFEL) 26

2.3.5 Strong field regime 28
2.3.6 Time-resolved MFPADs 31

3 Experimental setup **33**
3.1 Vacuum setup 33
3.1.1 Difference between the new and the old experimental setup 35
3.1.2 Source chamber 37
The cryostat 38
3.1.3 Pickup chamber 39
3.1.4 Cold trap chamber 40
3.1.5 Target chamber 42
3.1.6 Supersonic source chamber 44
3.1.7 Pumping 45
3.2 Optical setup 47

4 Velocity map imaging **51**
4.1 Operating mode 52
4.2 Abel inversion 52
4.3 VMI calibration 54

5 Aniline **57**
5.1 Laser-induced alignment of aniline molecules 58
5.2 Ionization pathways 60
5.3 Gas phase experiments 61
5.3.1 R2PI 61
5.3.2 0^0 vibrational mode 65
5.3.3 Alignment intensity study 73
5.3.4 1^1 vibrational mode 80
5.3.5 $6a^1$ vibrational mode 87
5.4 Conclusion and discussion 93

6 Naphthalene **95**
6.1 Laser-induced alignment of naphthalene molecules 96
6.2 Ionization pathways 98
6.3 Gas phase experiments 100
6.3.1 R2PI 100
6.3.2 $\bar{8}^1 7^1 8^1$ vibrational mode 101
6.3.3 $\bar{8}^1 \bar{7}^1 8^1$ vibrational mode 109
6.3.4 3^1 vibrational mode 117
6.4 Conclusion and discussion 125

7 Molecules embedded in helium droplets **127**
7.1 Aniline molecules in helium nanodroplets 128
7.2 Conclusion and discussion 140

8 Conclusion and outlook **143**
8.1 Resonant two-photon photoionization of aniline molecules in gas phase 144
8.2 Resonant two-photon photoionization of naphthalene molecules in gas phase 145
8.3 Resonant two-photon photoionization of aniline molecules in helium droplets 145

Bibliography **147**

CHAPTER 1

Introduction

My PhD project was embedded in the EU-funded Marie Sklodowska-Curie Innovative Training Network “ASPIRE”, aiming for “Angular Studies of Photoelectron in Innovative Research Environments”. The overall purpose of my PhD project was to investigate molecular frame photoelectron angular distributions (MFPADs). MFPADs are interesting because they are a means to study photoionization dynamics, structures and distributions of isolated molecules and intramolecular dynamical processes [1, 2]. The photoelectrons are sensitive to the molecular structure, since they scatter of the atomic framework [3], referred to as shape resonances [4]. The angular distribution also depends on the (molecular) orbital, from which they were ejected [3,5,6]. An introduction to MFPADs, as well as an overview over previous research is given in chapter 2.3.

The overall goal of my PhD project has been divided into four milestones. The first milestone of my project was to establish a new vacuum setup, reusing parts from an old experimental setup for these purposes. This old setup in its existing form was not suitable for the objective. Once the new setup had been tested and benchmarked to our satisfaction, the second goal was to conduct [1+1]-photoionization experiments on aligned molecules and obtain MFPADs. In a third step, VUV light should have been used to single-photon ionize molecules with sufficiently low ionization potentials. For this step, the vacuum setup would have needed further modification, e.g. the addition of a baffle to lessen the backscattering of the VUV light and thus also minimize background signal from electrons created from the chamber walls. In addition, the VUV's vacuum setup and the vacuum chamber containing the laser interaction region need to be connected. Ultimately, I would have explored MFPADs from singly-ionized molecules embedded in helium nanodroplets. Unexpected challenges related to the laser system caused delays and prevented to conduct the aimed for experiment to examine MFPADs with single-photon-ionization using VUV light.

In the first half of my time as a PhD student, I designed, built and tested a vacuum setup for these experiments in collaboration with Benjamin Shepperson, while a Master student, Signe Thorsen, built and characterized a tunable VUV light source. Chapter 3 is dedicated to the description of the built vacuum setup.

In the second half of my PhD, I conducted experiments obtaining PADs from aligned molecules. For the pursuit of MFPADs, the molecular frame coordinate system and the laboratory frame coordinate system need to coincide as much as possible. One means to achieve that is laser-induced alignment, which is introduced in chapter 2.2. During my PhD project, another research project in Femtolab involved truncated alignment pulses using a longpass filter, see section 2.2.4. It has been shown, that applying this truncated alignment pulse to molecules solvated in helium nanodroplets, see chapter 2.1, leads to high degrees of alignment under (almost) field-free conditions. Therefore, it is an interesting technique for the study of MFPADs and I investigated if it is feasible to obtain MFPADs from molecules in helium droplets. The results are shown in chapter 7.

In addition to this, aniline and naphthalene molecules were also studied in the gas phase. The results are presented in the chapters 5 and 6. Both species have been ionized with a [1+1]-photoionization process using a UV light source tuned to a resonance wavelength. The resulting PADs were recorded as electron velocity map images using a velocity map imaging (VMI) spectrometer, which is explained in chapter 4.

Chapter 2

Background

The overall goal of this project is to obtain molecular frame photoelectron angular distributions (MFPADs) from aligned molecules inside helium nanodroplets. The experiments were conducted with molecules in the gas phase as well as in helium nanodroplets. The latter are explained in section 2.1. In the presented experiments, the molecules were aligned to unite the molecular with the laboratory frame as much as possible. Thus, laser-induced alignment of molecules is discussed in section 2.2. Section 2.3 gives an introduction to MFPADs as well as a few highlights of work done in the field without any claim of completeness.

2.1 Helium nanodroplets

Helium is a noble gas of which two stable isotopes are known: bosonic ^{4}He and fermionic ^{3}He. In the presented experiments ^{4}He was used and throughout this manuscript, "helium" is referring to ^{4}He. Below 2.18 K ^{4}He is in its superfluid phase, denoted as "Liquid Helium II" in fig 2.1, separated from its fluid phase "Liquid Helium I" by the λ-line. In this regime, its viscosity is approaching zero, while the thermal conductivity approaches infinity [7]. This makes helium an interesting solvant matrix. The droplets are chosen over bulk helium, because in the latter impurities as well as dopant molecules coagulate to the walls [7,8]. How helium nanodroplets can be formed is discussed in section 2.1.1. The doping of helium droplets is elucidated in section 2.1.2.

Because of their superfluidity, molecules inside a helium nanodroplet can rotate freely. Furthermore, the helium droplet is evaporatively cooling itself, reaching asymptotically 0.37 K in about 0.1 ms [9][1]. These properties render them an interesting solvent matrix especially for IR-spectroscopy. Such and other applications of nanodroplets are discussed in section 2.1.3. The study of helium droplets themselves is addressed in section 2.1.4.

2.1.1 Droplet formation

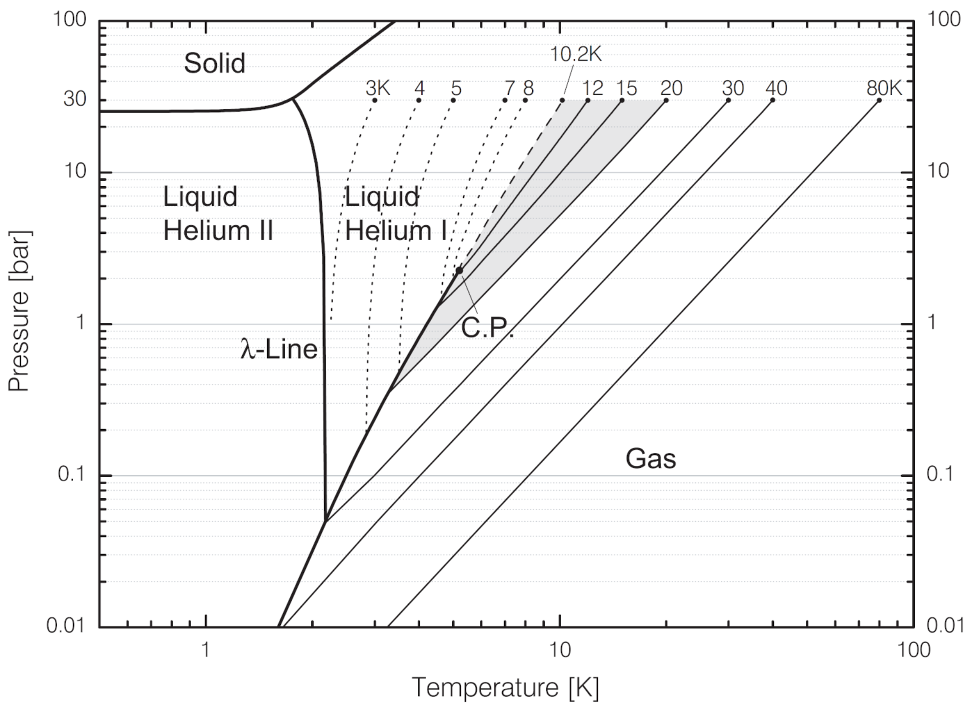

Figure 2.1: Phase diagram of helium: Phase boundaries in thick solid lines, isentrops starting in the liquid phase are dashed, isentropes starting in the gas phase are the thin solid lines, C.P. –critical point. Figure adopted from [10]

In order to form droplets, gas phase helium is expanded through the nozzle into the vacuum. There are two main domains on how the droplets form after the expansion: the subcritical and the supercritical regime [7, 9]. "Critical" refers to the critical point (C.P. in fig 2.1). The critical point marks the boundary above which with increasing pressure the liquid and the gas phase become indis-

[1]for a 5 μm nozzle, temperature below 20 K, backing pressure above 20 bar [9]

tinguishable. In the supercritical regime, helium initially exists in a liquid phase (Liquid Helium I) [10]. Thus, with the expansion into the vacuum chamber, the liquid fragments and forms the droplets, see also fig 2.2 middle section "Fragmentation of Liquid". In this regime the droplets have a size of 10^5 –10^7 atoms (several 10 nm) [8, 9]. Since the liquid is fragmenting further, these evaporated helium atoms can coagulate and form clusters [10]. The size distribution of the so-formed droplets is therefore broad [10]. Grisenti et al. also demonstrated larger droplets with more than 10^9 atoms (>0.25 µm [11]). These droplets are formed via a Rayleigh break-up of a liquid jet of either fluid or even superfluid helium, fig 2.2 upper section "Rayleigh Break-Up of Liquid Jet".

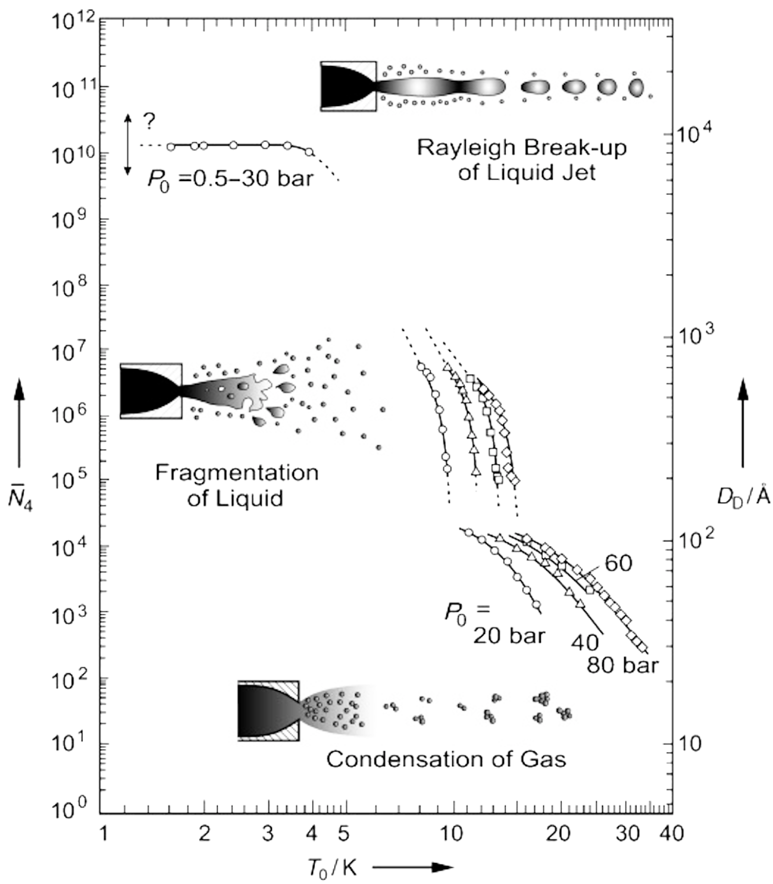

Figure 2.2: Number size (left y-axis) and droplet diameter (right y-axis) as a function of temperature and pressure for the different formation regimes: Rayleigh break-up of a liquid jet, fragmentation of the liquid and condensation of gas; figure adoped from [9]

The most common mode of droplet formation is the subcritical regime [9,10]. In this regime, the droplets grow by clustering [7,9], see "Gas" in fig 2.1 and lower section "Condensation of Gas" in fig 2.2. The droplets presented in chapter 7 are formed in this regime, with a nozzle temperature of 14 K and a backing pressure of 25 bar. Following the curves of Toennies et al. and Choi et al., these conditions lead to a droplet size of about $3 \cdot 10^3 - 10^4$ helium atoms and thus to a droplet diameter of approximately 5 – 10 nm [8, 9, 12].

2.1.2 Pickup process

To serve as a solvent matrix, the helium nanodroplets need to be doped with the desired species. The helium nanodroplet picks up the investigated molecules inside the pickup cell (see section 3.1.3). One advantage of helium nanodroplets is that they act as a "nanocryostat" for the dopant molecule through evaporative cooling of helium atoms or clusters [9]. Toennies et al. suggest a rule of thumb, according to which, 1600 helium atoms per 1 eV of energy (kinetic and internal) introduced by the dopant is evaporated [9]. However, neglecting the decreasing size the probability of picking up k molecules inside the helium droplet follows a poisson statistic [8]:

$$P_k(n) = \frac{(\alpha L)^k}{k!} e^{-\alpha L} \tag{2.1}$$

with: L the length of the pickup cell, $\alpha = \rho\sigma$, ρ the number density of the gas inside the pickup cell, and σ the helium droplet's cross section. The number density ρ is depending on the partial pressure of the dopant inside the pickup cell. Thus, by varying the pressure, one controls the average number of molecules that are picked up by the helium nanodroplet. An example of the pickup probability is shown in fig 2.3 for a mean droplet size of $4.1 \cdot 10^3$ atoms. The four different graphs show the probability to pick up k molecules depending on the partial pressure of the dopant species. With a low partial pressure, the probability to pick up one molecule peaks at $3 \cdot 10^{-5}$ mbar. When the partial pressure is increased, the probability of picking up just one molecules decreases, while the probability of picking up two or more molecules increases. As can be concluded from the curves in fig 2.3, at the peak probability of doping the droplets with one SF_6 molecule a significant number of droplets is also doped with a second molecule. In the measurements presented in chapter 7, the partial pressure has been chosen such that the probability of picking up one aniline molecule dominates as to avoid dimers for the measurements.

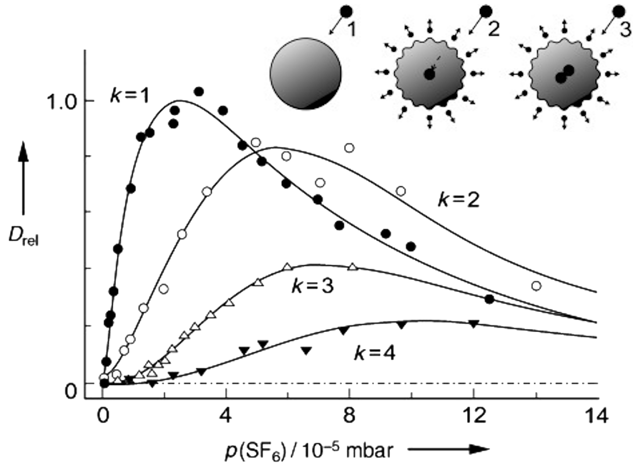

Figure 2.3: Depletion signal depending on the pressure of SF_6 in the pickup chamber for different absorption bands $(\mathrm{SF}_6)_k$, mean droplet size $4.1 \cdot 10^3$ helium atoms. The solid curves are fits to the data using eq 2.1. Inset above: Schematic of the successive pickup and evaporative cooling of molecules. Figure adopted from [9]

Once the droplet is doped, the molecule is likely found inside the droplet. However, some molecules and atoms do not reside inside the droplet after being picked up. Alkali and heavy alkaline earth metals are bound to the surface of the helium droplet [8,13]. Ancilotto et al. derived a formula to evaluate whether a cavity in the form of a bubble is formed inside the helium droplet or if the molecule or atom resides on the surface. The formula can naïvely be understood as the ratio of the energy cost to form a cavity of radius R, $\epsilon\rho R^3$, to the energy gain of the surface tension σR^2. Since R must nearly be r_{min}, the equilibrium separation [13]:

$$\lambda = \frac{\rho\epsilon r_{min}}{\sigma 2^{\frac{1}{6}}} \tag{2.2}$$

This time, with ρ being the number density of helium and σ the surface tension. The well depth is given as ϵ [13]. For λ>1.9, the molecule or atom is solvated into the droplet, which is the case for the majority of dopant species. For λ<1.9, the molecule or atom can be found on the surface of the droplet. Alkali atoms are known to reside on the surface [13]. They do not dissolve due to their weak interaction with the inert liquid [13]. However, Stark an Kresin have studied the solvation of alkali nanoclusters [14]. They evaluated the van der Waals attraction between alkali metals and helium, and the short-range repulsion and surface tension of a formed centre cavity [14]. They found the critical cluster size at which an alkali nanocluster is solvated in the droplet to increase with the atomic mass [14].

2.1.3 Applications of helium droplets

The use of helium nanodroplets for spectroscopy is discussed in several reviews, e.g. [7–9, 15, 16]. As mentioned before, the droplets act as a nanocryostat. Thus, few(er) quantum states are populated [7]. Therefore, the resolution in the spectrum improves and fewer quantum states need to be considered to interpret the spectrum [7]. Furthermore, the helium droplets also permit to study thermally unstable molecules as Choi and Miller have demonstrated in their infrared laser spectroscopy study of four tautomers of guanine. Since only low vapour pressures are required to dope the droplet, heating is not required, which is favourable for thermally unstable molecules [17].

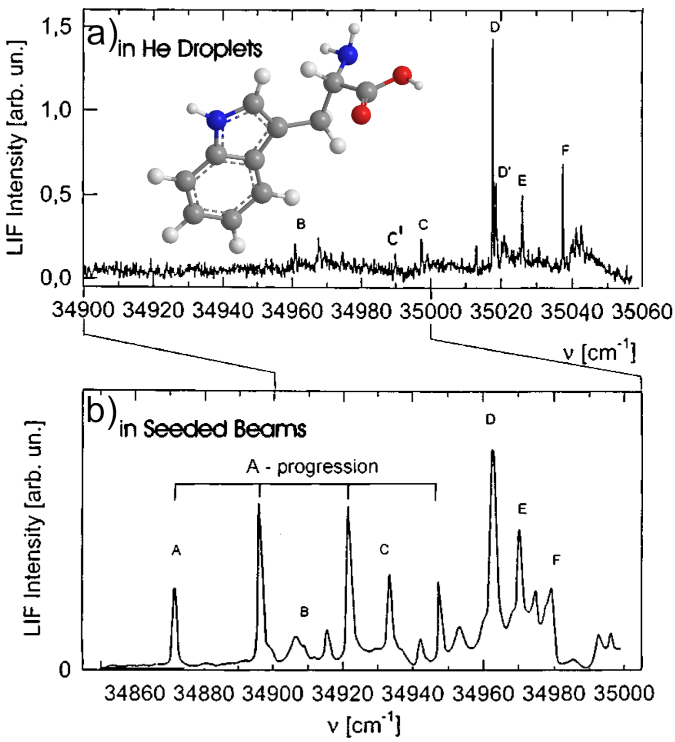

Figure 2.4: Comparison of LIF spectra of tryptophan, a) in helium nanodroplets ($8 \cdot 10^3$ atoms, E=30 μJ per pulse), b) in a seeded beam expansion. Excerpt from [18]. Inset: Tryptophan-molecule added for convenience

Lindinger et al. have reported sharpened spectra for tryptophan and tyrosine [18], which are shown in fig 2.4. On comparing the LIF spectrum obtained from molecules in a seeded beam (fig 2.4 b) with the spectrum obtained from molecules inside helium nanodroplets (fig 2.4 a), each peak is sharper. Especially feature D in b) is resolved as one peak, whereas it appears as two separately resolved peaks D and D' in a). They attributed this as an indication of two close lying isomers [18]. The spacing between D and D' is 1 cm^{-1} [18]. Furthermore, other peaks of the spectrum b) are not present in a). Lindinger et al. argue that these peaks in b) might be caused by hot bands. The spectrum is blue shifted by 55.0 cm^{-1}, which they attributed to the interaction between two electronic states, ^1L_a and ^1L_b.

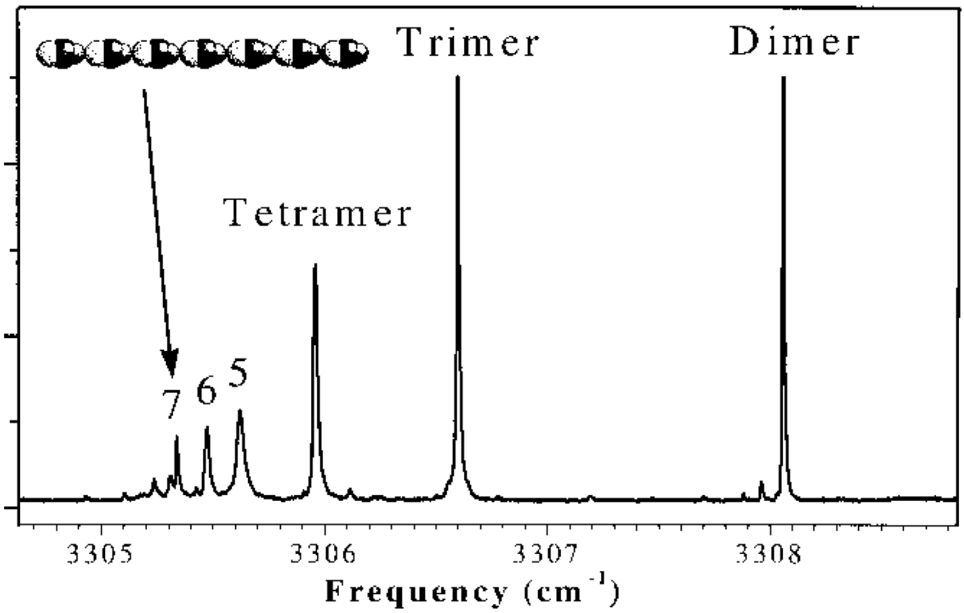

Figure 2.5: Spectrum of the free C-H stretch of the HCN polymers. The numbers 7-5 indicate the C-H stretch of the heptamer down to the pentamer. Inset: Linear heptamer chain of HCN. Figure adopted from [19]

In addition to the study of tautomers, the usage of helium nanodroplets opens another interesting study opportunity: conformers, which could not be observed at room temperature, can be studied in the nanocryostat. Nauta and Miller reported the formation of long chains of OCS molecules [19]. When a new molecule approaches the chain inside the droplet, they orient themselves in their respective fields, which leads to the formation of chains [19]. In a free gas expansion, the density is higher. In addition, the molecules have a higher internal energy enabling to overcome energy barriers presented by the potential energy surface in favour of the global minimum. Thus, an energetically more favourable isomer would be formed. They investigated the free C-H stretch of the OCS molecules embedded in helium droplets in a dc-electric field of 30 kV cm^{-1}. The field suppressed the P- and R-branches, see fig 2.5. With these spectra, they found that heptamers are indeed being formed inside helium nanodroplets [19].

Besides rovibrational-spectroscopy, helium droplets have also been used as a solvent matrix for electronic spectroscopy. The following paragraph follows the description found in review [15]. While the helium droplet remains rather indifferent to rovibrational excitation, the interaction between the droplet and its dopant, anisotropic in nature, changes exceedingly upon electronic excitation. As the electronic excitation can change the interaction strength and the anisotropy, it can even alter an attractive interaction to a repulsive one. A molecule residing inside the droplet before excitation might be ejected afterwards. In other cases, also seen for aniline embedded in helium nanodroplets [20], the changing interaction potential gives rise to phonon wings to the blue side of the spectrum. The zero phonon lines usually appear rather sharp and also slightly shifted to the red or the blue, usually less than $\pm$ 120 cm^{-1}[2]. For naphthalene a blue frequency shift of 15 cm^{-1} for the $S_1 \longleftarrow S_0$ transition was observed (32035 cm^{-1}), for aniline 116 $\pm$84 cm^{-1} [20].

Furthermore, the shape of the bubble surrounding the dopant molecule depends on the electronic structure of the molecule. The excited and the ground state can exhibit different nodal structures and thus the electron density is also altered. This changes the interaction with the surrounding helium atoms and they rearrange and give rise to a phonon wing in the spectrum. For some molecules, e.g. tetracene, some helium atoms might get attached to the molecule [15]. As they cannot fill all the potential minima at the same time, because the distance between helium atoms is about 1 Å larger than the distance between the benzene ring centres, different helium solvation shells can be observed as isomers [15]. Therefore, the zero phonon line splits [15].

2.1.4 Studies of helium droplets

Not only molecules or atoms solvated in helium droplets, also helium droplets themselves have been studied extensively, both experimentally [12, 21–24] and theoretically [25–27]. Harms et al. have conducted a scattering experiment with helium droplets and used krypton and argon as scattering agents to investigate the liquid-vapour interface of helium nanodroplets with 10^3–10^4 atoms [12]. A

[2] see tab I in ref [15]

large percentage of helium atoms in a droplet contribute to the surface. In a droplet with 5000 atoms, approximately half of them belong to the surface region [12]. They found the density of droplets in the region of about $6 \cdot 10^3$ atoms to be about 62–70% of the density of bulk helium[3], while for very small droplets, 703 atoms, it is only 40% and for large droplets $13 \cdot 10^3$ it is 85% [12]. The calculated density distributions of droplets of different sizes depending on the radius is shown in fig 2.6 a). Inside the droplet, the density is that of the bulk. When the radius approaches the finite radius, the density drops. As a comparison, the experiments showing the transmission of argon and krypton is given in fig 2.6 b). The transmission curve and the calculated density distribution agree well. The effective radius for a droplet with 10^4 atoms is marked as R_{eff}. Furthermore, they measured the surface thickness[4] to be 6.4 ± 1.3 Å.

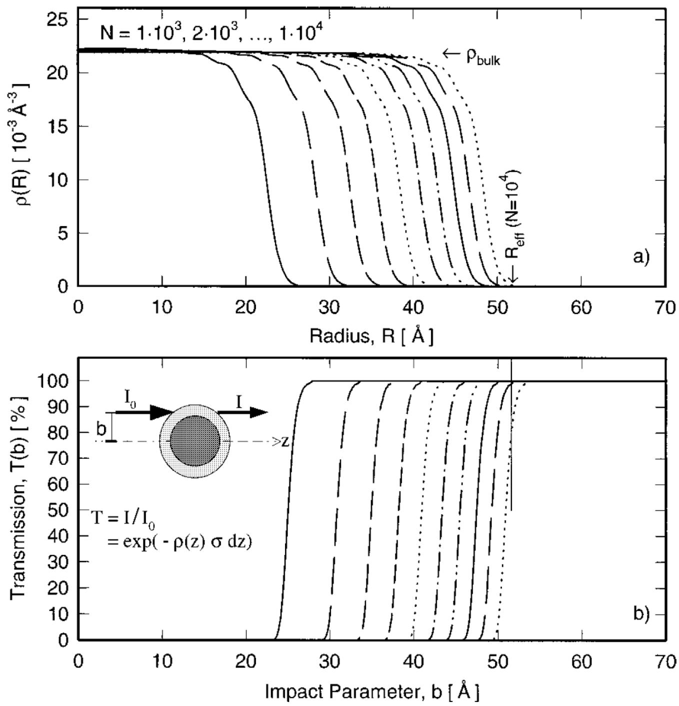

Figure 2.6: Comparison of the a) DFT calculated density distributions as a function of the droplet size with 10^3-steps, b) Transmission of the argon or krypton beam respectively. R_{eff} marks the effective radius of a droplet with 10^4 helium atoms marked with a line in b) and a caption in a). Figure adopted from [12]

[3] ρ_{bulk}=0.0218 Å^{-3} [12]
[4] 10-90% thickness; thickness in which the density rises from 10% to 90%

The superfluidity of bulk liquid helium was experimentally demonstrated by Kapitza in 1938 [28], while Grebenev et al. documented the superfluidity of helium nanodroplets in 1998 [21]. They investigated the IR absorption spectra of OCS in ^{4}He droplets, fig 2.7 A, and in ^{3}He droplets, fig 2.7 B. Both matrices are nearly identical in atomic features. ^{3}He droplets are colder (0.15 K) than ^{4}He droplets (0.37 K) and ^{3}He atoms are lighter than ^{4}He atoms. If the cause for free rotating molecules inside the droplets were the weak van der Waals interactions, the effect should be more pronounced in the case for ^{3}He droplets. However, this is not the situation. While in ^{4}He droplets the P- and R-branches of OCS are visible, the spectrum from OCS in ^{3}He droplets exhibits a broad peak, fig 2.7 A and B. While the bosonic ^{4}He is a superfluid at 0.37 K, the fermionic ^{3}He is still a normal fluid at 0.15 K. Thus, the remarkable effects of ^{4}He nanodroplets on the IR spectrum, fig 2.7 A, can be attributed to the droplet's superfluidity. As a further evidence, Grebenev et al. doped ^{3}He droplets with an increasing number of ^{4}He atoms, fig 2.7 C. The lines get clearly visible when the threshold of 60 ^{4}He atoms is reached. This is consistent with the OCS molecule being encapsulated by two shells of ^{4}He atoms [21].

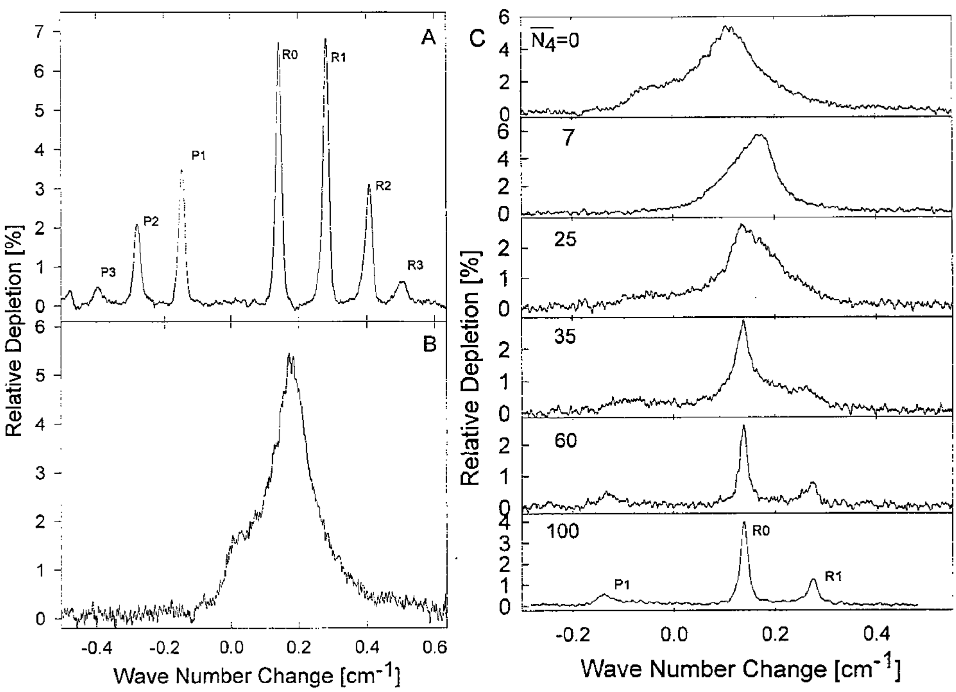

Figure 2.7: IR spectra of OCS molecules inside A –^{4}He droplets B –^{3}He C –IR Spectra of OCS in ^{3}He droplets with N_4 ^{4}He atoms added to the droplet. Excerpt from [21]

Since a helium droplet is finite in size, any liquid flow must involve rotational motion [23]. As a helium nanodroplet is also superfluid, this rotational motion reveals itself as quantized vortices [23]. While Bewley et al. first visualized the quantized vortices in bulk helium [29], Gomez et al. documented the quantized vortices also for helium nanodroplets using coherent X-ray diffraction [23]. The rings in fig 2.8 A and B are X-ray diffraction images of droplets doped with xenon. The shorter axis in the diffraction pattern correlates to the longer droplet axis [23]. Furthermore, fig 2.8 A and B also display Bragg spots (red circles). These Bragg spots are Xe structures with a period of 100 nm, which corresponds to the expected distances for quantized vortices [23].

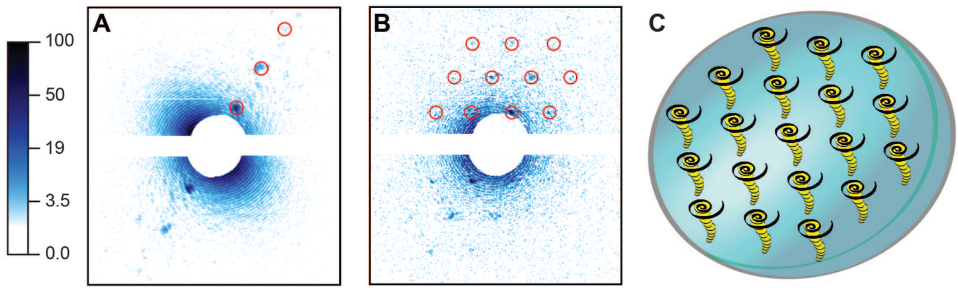

Figure 2.8: A,B: XRD images of droplets doped with xenon, the rings corresponding to the droplet shapes, Bragg spots enhanced with red circles. C Xenon atoms condensating along vortices. Figure adopted from [23]

2.2 Alignment

In this section, I want to give an introduction to laser-induced alignment. First, a qualitative theoretical description of laser-induced alignment for a linear molecule is given in sec 2.2.1. For laser-induced alignment, two main domains are distinguished, adiabatic and non-adiabatic alignment, which are discussed in the sections 2.2.2 and 2.2.5. An introduction to calculating an estimated degree of alignment can be found in section 2.2.3. The experiments have been conducted using a truncated alignment pulse, which is motivated in section 2.2.4.

In general, gas phase molecules are randomly oriented in space. However, a variety of intriguing processes and characteristics depend on the relative orientation between the molecules and other molecules or the molecules and the investigative method. For example, in collision studies from molecules with each other or with surfaces, their collision cross-sections depend on their orientation [30]. As another example, the reaction rate of the S_N2 reaction of a chlorine ion with methyliodide $Cl^- + CH_3I \longrightarrow CH_3Cl + I^-$ exhibits a maximum, when the chlorine ion approaches from the methyl group [31]. Another application for the alignment of molecules is to record MFPADs. In order to access the molecular frame in the laboratory frame, both need to coincide as much as possible. Therefore, it is desirable to "fix" and orientate the molecules in space for such experiments. Aligning molecules is a technique to achieve that.

The degree of alignment is qualified with two observables: The observable $\langle\cos^2\theta\rangle$ and its two-dimensional projection $\langle\cos^2\theta_{\mathrm{2D}}\rangle$. The angle θ refers to the angle between the major molecular axis and the polarization of the laser axis [31] and is one of the Euler angles connecting the molecular coordinate system with the laboratory coordinate system, see section 2.2.1. The angle θ_{2D} is its projection onto the two-dimensional detector. Consequently, randomly oriented molecules result in a degree of alignment $\langle\cos^2\theta\rangle$ of $1/3$ and $\langle\cos^2\theta_{\mathrm{2D}}\rangle$ of $1/2$. Perfectly aligned molecules correspond to a degree of alignment of 1.0. Note, that $\langle\cos^2\theta_{\mathrm{2D}}\rangle$ is usually higher than the three-dimensional $\langle\cos^2\theta\rangle$, since it is its two-dimensional projection. A special case of alignment, not part of this work, is orienting molecules. In addition to aligning the molecular axis, the molecule's head-to-tail order is also determined. The degree of orientation is measured as $\langle\cos\theta\rangle$.

Several methods are available for aligning molecules. If the molecule has a permanent dipole moment, a static electric field can be used to orient the molecules [31]. Since the molecules are required to interact much stronger with the field to overcome their rotational energy, the static electric field needs to be powerful [31]. Therefore, the technique is also called "brute force orientation" [31]. Instead of employing a permanent dipole moment, it is also possible to induce a dipole, which interacts with the electric field.

The degree of alignment improves if the initial rotational temperature of the molecules is lowered [32]. Embedding the molecule in a helium nanodroplets is one way of ensuring this. Another method, documented in our group [33], employed deflecting cold molecular beams with an electrostatic beam deflector. By this means low rotational states and thus rotationally cold molecules could be selected.

2.2.1 Theoretical description

The theoretical basis to describe laser-induced alignment was introduced by Friedrich and Herschbach in 1995 [34, 35]. Assuming the molecule bond-lengths are fixed and the molecule cannot vibrate (rigid-rotor approximation), and furthermore assuming that the nuclei and electrons can be evaluated independently (Born-Oppenheimer approximation), the field-free Hamiltonian is composed as follows:

$$\hat{H} = \hat{H}_{rot} + \hat{H}_{vib} + \hat{H}_{el} \tag{2.3}$$

Assuming the electric field of the laser only excites rotational states, the relevant part of the Hamiltonian is the rotational part[5]:

$$\hat{H}_{rot} = \frac{\hat{J_x}^2}{2I_{xx}} + \frac{\hat{J_y}^2}{2I_{yy}} + \frac{\hat{J_z}^2}{2I_{zz}} \tag{2.4}$$

with $\hat{J}_i$ the angular momentum operator and I_{ii} the moment of inertia of the i-axis of the molecule, in the molecular frame coordinate system xyz, with the unity vectors $\vec{x}_0$, $\vec{y}_0$ and $\vec{z}_0$. For asymmetric top molecules $I_{xx} < I_{yy} < I_{zz}$ and for linear molecules $I_{xx} = I_{yy} = I$, $I_{zz} = 0$. Although naphthalene and aniline are asymmetric top rotors, we here limit ourselves to linear molecules to investigate the general idea. The resulting energy of a rotational state using the rotational constant $B = \frac{\hbar^2}{2I}$ is:

$$E = BJ\,(J+1) \tag{2.5}$$

[5] Small letters will be used for the molecular frame, while capital letters refer to the laboratory frame coordinate system

We now introduce the electric field of a laser pulse with a frequency ω and an envelope amplitude $\epsilon_0(t)$:

$$\vec{\epsilon} = \epsilon_0(t)\cos\omega t \vec{Z}_0 \tag{2.6}$$

$\vec{Z}_0$ is a unity vector in the laboratory frame. The interaction potential between the molecule and the electric field can be described as follows:

$$\hat{V} = -\vec{\mu}\cdot\vec{\epsilon} - \frac{1}{2}\vec{\epsilon}^{\dagger}\underline{\underline{\alpha}}\vec{\epsilon} \tag{2.7}$$

with $\vec{\mu}$ the molecule's permanent dipole moment and $\underline{\underline{\alpha}}$ its polarizability tensor. Note, that $\hat{V} = \hat{V}(t)$, since the electric field is time-dependent. The hyperpolarizability terms and higher order terms have been neglected. The hyperpolarizability terms are relevant in e.g. orientation experiments, see supplementary material in ref [36] for a discussion. Since the electric field is oscillating, the torque introduced by the interaction between the electric field and the permanent dipole moment $\vec{\tau} = \vec{\mu}\times\vec{\epsilon}$ vanishes. In the case of a linear molecule, the polarizability tensor $\underline{\underline{\alpha}}$ is diagonal. Averaging over multiple cycles introduces a factor $\frac{1}{2}$ for the oscillating part of the field $\cos\omega t$. The interaction potential therefore simplifies to:

$$\hat{V} = -\frac{1}{4}\sum_i \alpha_{ii}\left|\epsilon_{0,i}\right|^2 \tag{2.8}$$

with $\epsilon_{0,i}$ being the amplitude of the field in the i-direction of the molecule. Now, the interaction potential is written in the molecular frame. It has thus connected the molecular frame with the laboratory frame, since the electric field has only been established in the latter. Mathematically, this can be described as a coordination transformation, employing two of the three Euler angles: θ and ϕ, where θ is the angle between $\vec{Z}_0$ and $\vec{z}_0$ and ϕ the angle between the projection of $\vec{Z}_0$ onto the xy-plane in the molecular frame and $\vec{x}_0$.

$$\hat{V} = -\frac{1}{4}\left|\epsilon_0\right|^2\left\{\alpha_{zz}\cos^2\theta + \sin^2\theta\left(\alpha_{xx}\cos^2\phi + \alpha_{yy}\sin^2\phi\right)\right\} \tag{2.9}$$

For a linear molecule $\alpha_{zz} = \alpha_{\|}$ and $\alpha_{xx} = \alpha_{yy} = \alpha_{\perp}$, thus:

$$\hat{V} = -\frac{1}{4}\left|\epsilon_0\right|^2\left\{\left(\alpha_{\|} - \alpha_{\perp}\right)\cos^2\theta + \alpha_{\perp}\right\} \tag{2.10}$$

If $\alpha_{\|} > \alpha_{\perp}$, the interaction potential exhibits minima for $\theta = 0, \pi$. Thus, molecules will align with their most polarizable axis parallel to the laser polarization axis. In other words, only θ of the three Euler angles $R = (\theta, \phi, \chi)$ is confined. This calculation only considered one-dimensional alignment of linear molecules. Nevertheless, for asymmetric top rotors, such as aniline and naphthalene, the most polarizable axis will be aligned parallel to the linearly polarized electric field of the laser pulse.

Furthermore, the experiments presented in the chapters 5, 6 and 7 also include three-dimensional alignment. A detailed theoretical analysis of three-dimensional alignment of asymmetric top rotors is beyond the scope of this work and the interested reader is referred to ref [37] for a discussion. In summary, the alignment laser pulse polarization in this case is not linear, but elliptic. This means the dependence on χ also needs to be considered in the interaction term describing the interaction between the molecule and the electric field of the laser pulse. The interaction describes how θ and χ are confined in space. If two of the three Euler angles, θ and χ are confined in space, the third Euler angle, ϕ, is consequently also fixed in space. Thus, the molecule is three-dimensionally aligned.

2.2.2 Adiabatic alignment

Within the adiabatic alignment regime the laser pulse is much longer than the rotational period of the molecule [31]. The laser pulse exhibits an electric field that slowly turns on, starting the interaction with the molecule, hitherto a free rotor, see fig 2.9 a). The formerly free rotor with its states $|JM\rangle$ is now a pendular eigenstate of the system, which can be expressed as $|J'M\rangle$. With the rotational quantum number J and M its projection on the laboratory frame in $\vec{Z}_0$-direction, $M \in [-J, -J+1, ..., J]$. After the peak of the pulse the polarizing field vanishes slowly and the molecule becomes a free rotor again.

For one-dimensional alignment, linearly polarized fields are employed. The molecule's most polarizable axis aligns in the direction of the laser pulse polarization. However, it can still rotate freely around this axis, fig 2.9 b). For three-dimensional alignment elliptically polarized laser pulses are utilized. The molecule's most polarizable axis aligns with the major axis of the ellipse, while the molecule's second most polarizable axis aligns with the minor axis of the ellipse. Therefore, also the third molecular axis is defined in space and the molecule is three-dimensionally aligned, fig 2.9 c).

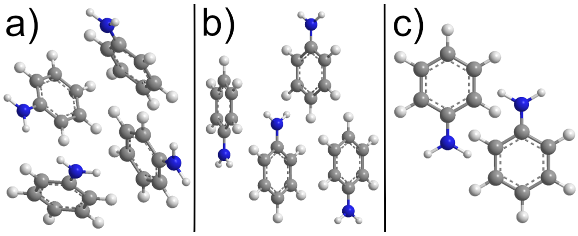

Figure 2.9: a) unaligned aniline molecules b) one-dimensionally aligned aniline molecules c) three-dimensionally aligned aniline molecules

2.2.3 Estimating the achievable alignment

In the course of a previous PhD project in our group an alignment calculator has been developed by Anders A. Søndergaard for calculating $\langle\cos^2\theta_{\text{2D}}\rangle$ and $\langle\cos^2\theta\rangle$ for 1D alignment and the interested reader is referred to references [38] and [39] for a detailed description. Here, a brief overview will be given.

A further addition to this programme[6] also includes custom pulses. The calculator is designed for symmetric top rotor molecules, but nevertheless can be used to estimate the maximum achievable alignment for an asymmetric top rotor. It numerically solves the Schrödinger equation projecting on one $|JKM\rangle$ state during the pulse [38]:

$$i\hbar\frac{\partial}{\partial t}C^J_{KM} = H^J_K C^J_{KM} + \sum_{J'} C^{J'}_{KM}\langle JKM|V(\theta,t)|J'KM\rangle \tag{2.11}$$

with:
K – the projection of J onto the $\vec{z}$-axis,
C^J_{KM} – expansion coefficients, resulting from 2.12
H^J_K – the energy eigenvalue of the $|JKM\rangle$ state, $H^J_K = BJ(J+1)+(A-B)K^2$
A, B – the rotational constants of the molecule
$\langle JKM|V(\theta,t)|J'KM\rangle$ – the matrix elements of the interaction potential

Thereafter, the propagation of the wave packet after the pulse and along with that also the revivals, see section 2.2.5, are calculated with the matrix elements of $\cos^2\theta$ [38]. Based on which, the matrix elements for $\cos^2\theta_{2D}$ are calculated as well [38].

[6] added by A. A. Søndergaard, A. S. Chatterley and A. V. Jørgensen

2.2.4 Alignment in helium nanodroplets using truncated pulses

In order to achieve well-resolved MFPADs, the molecules should be tightly aligned three-dimensionally. For this purpose, especially for asymmetric top rotors, adiabatic alignment is desirous. In previous experiments in our group the possibility to align molecules embedded in helium nanodroplets adiabatically [40] and near-adiabatically [41] has been demonstrated. The compromise on using adiabatic or near-adiabatic pulses is the presence of the field on the maximum degree of alignment.

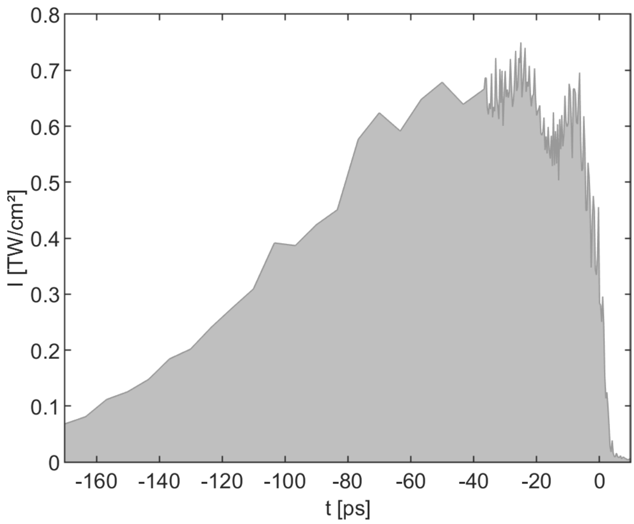

Figure 2.10: Truncated alignment pulse

In another experiment in our group, long-lasting field-free alignment has been achieved using truncated pulses [42] on molecules embedded in helium droplets [43]. A window for field-free experiments on aligned molecules of 10 ps and even longer, depending on the species, has been found [43].

The truncated pulse is a pulse that switches on slowly ($\approx$ 100 ps) and shuts down quickly (few ps), see fig 2.10. The untruncated pulse has a centre wavelength of 800 nm. A longpass filter is introduced to cut the pulse spectrally at 800 nm, reflecting any wavelength shorter than 800 nm. Since the pulse is also chirped, the pulse is also truncated in time. The laser intensity after the truncation edge is reduced by 2-3 orders of magnitude. Another means of truncating a pulse is using a switching pulse [44].

2.2.5 Non-adiabatic alignment

Though non-adiabatic alignment is not used in the experiments throughout this manuscript, it shall be discussed briefly for the sake of completeness. With non-adiabatic alignment, the laser pulse duration is much shorter than the inherent rotational period of the molecules [32]. The interaction between the molecules and the kick pulse introduces a rotational wave packet [32], which can be expanded onto an angular momentum basis:

$$|\Psi_{KM}\rangle = \sum_J C^J_{KM}|JKM\rangle \tag{2.12}$$

Shortly after the pulse, the alignment curve exhibits a maximum, i.e. the rotational wave packet components interfere constructively. As the components dephase, the degree of alignment drops almost to the value seen with unaligned molecules, see dashed line in fig 2.11. After a specific time, which depends on the rotational constant B of the molecules, the components are in phase again – leading to a $1/4$, $1/2$, $3/4$ and full revival, see fig 2.11. These revivals do not necessarily exhibit a $\langle\cos^2\theta\rangle$ with only a maximum and can be accompanied by a minimum, less than $\langle\cos^2\theta\rangle = 0.33$, see e.g. the 1/4 revival in fig 2.11. In field-free experiments, the maxima are often referred to as alignment and the minima as anti-alignment, since the most polarizable axis of the molecule is oriented perpendicular to the direction of the laser polarization.

Revivals are known for symmetric top molecules in the 1D alignment case as J-type revivals. A J-type revival is the results of a symmetric top rotation. In contrast to symmetric top molecules, asymmetric top molecules do not exhibit the same periodically reconstruction of the alignment [45]. The dynamics of nonadiabatically aligned asymmetric top molecules is subject to the fluence of the laser pulse [46]. For asymmetric top molecules, J-type revivals and C-type revivals have been documented [32]. Thus, asymmetric top molecules can exhibit a a quasi-symmetric-top-like rotational behaviour as well. A C-type revival results from the molecule's rotation about the axis perpendicular to the molecular plane [32].

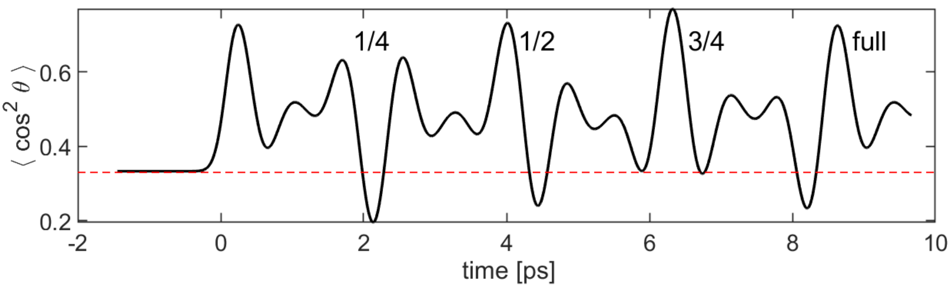

Figure 2.11: Alignment trace for N_2 molecules calculated using the alignment calculator described in section 2.2.3; Gaussian alignment pulse, intensity 16 TW cm^{-2}. Dashed red line: $\langle \cos^2\theta \rangle$ of unaligned molecules (0.33), $1/4$, $1/2$, $3/4$ and full revivals are marked accordingly.

Guérin et al. suggested combining an adiabiatic pulse with a kick pulse, resulting in a pulse that ramps up adiabatically and ends with a kick pulse [47]. For aligning a CO_2 molecule, they predicted a maximum degree of alignment of $\langle \cos^2\theta \rangle \approx 0.915$ [47][7]. Furthermore, they found indications for a perfect rephasing of the wave packet components [47]. This would be equal to finding the aforementioned maximum alignment under field-free conditions.

[7]including the ionization probability, T=30 K, I_{ramp}=10 TW cm^{-2}, I_{kick}=50 TW cm^{-2} [47]

2.3 MFPADs

In this chapter, I am giving an overview of previous research on photoelectron angular distributions (PADs) in general and molecular frame photoelectron angular distributions (MFPADs) in particular. One way to access the molecular frame is to measure fragments of the investigated species and photoelectrons in coincidence. The section 2.3.2 focuses on that topic. Another technique to address the molecular frame is aligning the molecules prior to ionization, which was briefly discussed in section 2.2. Reid found that in order to access the molecular frame in the laboratory frame, the three-dimensional degree of alignment needs to be 0.9 or better [48]. As MFPADs are also depending on the kinetic energy of the photoelectrons and thus the energy of the ionizing photon, other energy ranges than those that are used in this experiment are considered in the sections 2.3.3 and 2.3.4. Previous experiments in Femtolab involved strong-field ionization and are presented in section 2.3.5. MFPADs can also exhibit a time-dependent nature, which is addressed in section 2.3.6.

The first apparatus recording PADs was introduced by Lawrence and Chaffee in 1930 [49]. Polarized UV light was generated with a monochromator, restricting the wavelength to 240 nm, and quartz plates to ensure the light was polarized linearly. With a slit and a Faraday cage the photoelectrons emitted from a potassium jet were recorded with respect to the light polarization's angle, confirming Sommerfeld's $\cos^2\theta$-law[8]. Compared with today's VMI images this would correspond to a radial integrated, angular resolved measurement.

In 1968, Hall and Siegel showed that photoelectrons from $O^-(^3P)$ and $C^-(^4S)$ exhibit a maximum perpendicular to the laser polarization direction. This differs from $H^-(^1S)$, which shows a maximum parallel to the laser polarization direction [6]. Cooper and Zare predicted this behaviour in the same issue [5] and the theoretical and experimental findings were in good agreement. In the case of $H^-(^1S)$ only a p-wave channel resulting in a distribution proportional to $\cos^2\theta$, where θ is the angle between the emission direction and the laser polarization axis. On the other hand for $O^-(^3P)$ and $C^-(^4S)$, s-wave and d-wave channels are available, which interfere destructively, resulting in a distribution proportional to $\sin^2\theta$ [6].

Today, PADs provide a means to study photoionization dynamics, structures and distributions of isolated molecules and intramolecular dynamical processes [1, 2]. The photoelectrons are sensitive to the molecular structure, since they encounter the atoms as scattering centres [3]. This phenomenon is widely referred to as shape resonance [4]. Furthermore, their angular distribution de-

[8] Sommerfeld's $\cos^2\theta$-law predicts an angular dependence for emitted photoelectrons from hydrogen atoms: $I \propto \cos^2\theta$ [50]

pends on the (molecular) orbital from which they were ejected [3, 5, 6]. Despite the fascinating possibilities MFPADs open to investigate molecules and the vast interest in the field, understanding them is still challenging [2, 51].

2.3.1 Theoretical motivation

An approach from theory deriving expressions to characterize the PAD of a fixed diatomic molecule was made in 1976 by Dill [52]. The method was expanded to polyatomic molecules in 1987 by Chandra, also exploiting molecular symmetry to facilitate the expressions [53]. The photoelectron wave function are expanded in terms of spherical harmonics adapted to the symmetry [54]. The angle between the direction of the electric field vector and the molecular axis is given as a set of Euler angles $(\theta_M, \phi_M, \chi_M)$. The MFPAD can be expressed through spherical harmonics $Y\left(\theta_M, \phi_M\right)$ and weighting factors B_{LM}. Close to the notation by ref [54], this expression reads as follows:

$$I\left(\theta_M, \phi_M\right) = \sum_{LM} B_{LM} Y_{LM}\left(\theta_M, \phi_M\right) \tag{2.13}$$

In eq 2.13 L can take values from 0 to $2\ell_{max}$, ℓ_{max} corresponding to the highest partial wave contributing to the MFPAD. The MFPAD can lose its up-down symmetry, if even and odd partial waves interfere, and lead to nonzero coefficients B_{LM} for odd L.

However, these are considerations for fixed molecules, i.e. PADs in the molecular frame. In the laboratory frame the molecules are not fixed perfectly in space. Their molecular axes are distributed. Underwood and Reid introduced a formalism to compare between the laboratory frame PAD (LFPAD) and the molecular frame PAD (MFPAD). They approach the LFPAD as a convolution of the MF-PAD with the distribution of the molecular axes, $F\left(\theta, \phi\right) = \sum_{KQ} A_{KQ} Y_{KQ}$ [54], where θ_L, ϕ_L are part of the Euler angles connecting the LF and the MF. The indices K and Q specify the rank and component [54], with $K = 0, 1, 2, \ldots$ and $-K \leq Q \leq K$ [48]. In a cylindrical symmetric distribution, only terms with with $Q = 0$ contribute to the distribution [48, 54]. In the special case of an isotropic distribution $K = 0$ as well as $Q = 0$ [48]. Underwood and Reid found the following expression for the LFPAD $I\left(\theta_L, \phi_L\right)$:

$$I\left(\theta_L, \phi_L\right) = \sum_{LQ} \beta_{LQ} Y_{LQ}\left(\theta_L, \phi_L\right) \tag{2.14}$$

In contrast to eq 2.13, L can only take values up to $K_{max} + 2$, with K_{max} the rank of the highest nonzero moment in $F\left(\theta, \phi\right)$. The electric field vector is symmetric. Thus, even and odd ℓ partial waves cannot interfere and L can only be even. The parameters β_{LQ} are called anisotropy parameters [1] or asymmetry parameter [5, 52]. They depend on the symmetry as well as on the distribution of the molecular axes. If the LFPAD is cylindrical symmetric, $\beta_{LQ} \neq 0$ only for $Q = 0$. If the geometry of the experiment is cylindrically symmetric, anisotropy parameters can be extracted for a fit to Legendre polynomials through Abel inversion, see section 4.2.

2.3.2 MFPADs measured from electrons and ions in coincidence

One coincidence technique is cold target recoil ion momentum spectroscopy (COLTRIMS). It provides a means for a kinematically complete scattering experiment [55]. In a COLTRIMS the molecule species of interest is effused via a supersonic gas expansion [55] into a well-defined reaction zone. The probing projectile can be an ion, electron or photon [55]. The targeted species fragments and electromagnetic fields guide these fragments towards time- and position-sensitive detectors [55]. However, this powerful technique requires that the investigated species fragments and does so in the axial recoil limit [55].

Williams et al. have demonstrated three-dimensional MFPADs from methane using the COLTRIMS technique. They probed methane with 295 eV photons, which were linearly polarized [56]. They observed two decay channels: an Auger decay (H^+,H^+,CH_2) and simultaneous double Auger decay (H^+,H^+,$CH_2{}^+$) [56]. They recorded the corresponding photoelectrons in coincidence with the fragments [56]. Figure 2.12 shows 3D MFPADs from a low electron energy channel, 4.35 eV. The polarization has been varied: parallel to the C_2 axis (fig 2.12 left column), linearly polarized perpendicular to the C_2 axis (fig 2.12 middle column), and perpendicular to a C_3 axis along one bond and in plane with another bond (fig 2.12 right column). It is striking in fig 2.12 that the electrons are preferably ejected along the directions of the bonds, scattering from the potential of the parent molecule. Furthermore, a preference of an ejection along the polarization direction is evident. It is caused by an initial $1\,\mathrm{s} \longrightarrow \epsilon\,\mathrm{p}$ transition, where ϵ represents the polarization of the incoming light.

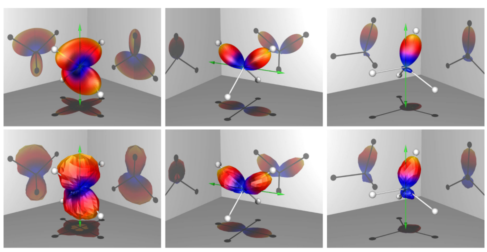

Figure 2.12: MFPADs from methane with respect to the orientation of the polarization axis (green arrow). Top: calculated, bottom: experimental. Figure adopted from [56]

2.3.3 Midrange photon energies (XUV)

Experiments in the extreme ultraviolet range (XUV) have been performed, e.g. by Rouzée and coworkers, see refs [3, 57, 58]. They generated the XUV light through high harmonic generation (HHG) by focussing an IR beam into a 3 mm long gas cell containing 25 mbar of Argon [57]. They achieved photon energies in the regime 17-45 eV. As the ionization potentials (IP) of the investigated species, CO_2 (IP=13.8 eV [3]), O_2 (IP=12.3 eV [57]), N_2 (IP=15.6 eV [57]) and CO (IP=14 eV [57]), are (significantly) lower than that, the observed photoelectrons were emitted via the absorption of a single photon and have a high kinetic energy. It also addresses more than one molecular orbital. For the CO_2-molecule, the HOMO down to the HOMO-3 contributed the MFPADs and were observed as different channels [3]. Kelkensberg et al. documented changes in the angular distributions on aligning or antialigning the molecules depending on the origin orbital prior to Coulomb exploding [3]. For the HOMO and HOMO-1, they found the electron signal to be suppressed when the molecules were aligned (most polarizable axis parallel to the probe pulse). When the molecules were antialigned (most polarizable axis perpendicular to the probe pulse), the signal was enhanced. Whereas the signal gets enhanced for the HOMO-2 and HOMO-3 channel when the molecules are aligned, and suppressed when they are antialigned, fig 2.13 b). This is related to the nature of the transition. If it is a parallel transition, the signal gets enhanced upon alignment. If the transition is perpendicular, the signal is enhanced upon antialignment. The anisotropy parameter β_2 for the HOMO orbital is only marginally influenced by the alignment, while the HOMO-1 to HOMO-3 channel exhibit a pronounced change, fig 2.13 c). The HOMO-1 and HOMO-2 exhibit a peak in β_2, when the molecules are antialigned. While the β_2-distribution for the HOMO-3 channel has its maximum, when the molecules are aligned. A differential PAD is shown in fig 2.13 d). It shows the difference between the aligned photoelectron angular distribution and the unaligned one and compares the theoretical calculations with the experimental results. When the signal is enhanced while the molecules are antialigned, the value gets negative, which indicates a perpendicular transition. They furthermore investigated the differential PADs in dependence to the incident photon energy. For the HOMO-2 they documented a striking change in the differential PAD. While the resulting values were positive below 15 eV, above 15 eV negative values appeared. This indicates the final state shifts from Σ_U to Π_U.

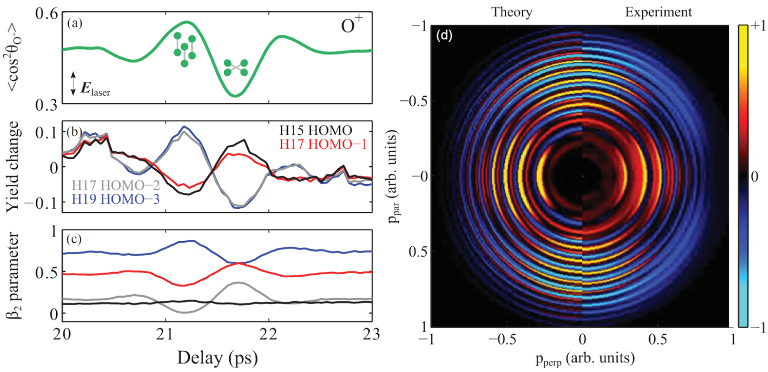

Figure 2.13: As a function of delay time between the alignment and the ionizing XUV pulse: a) degree of alignment b) electron yield c) β_2-parameter. d) differential PAD left: theoretical calculations, right: experimental results. Excerpt from [3]

2.3.4 High photon energies (XFEL)

X-ray free-electron lasers provide a source of photons with energies above 100 eV. Figure 2.14 shows how the MFPAD of C 1s of CO are evolving with the photon energy. The molecular frame is accessed by aligning or orienting the molecules and interpreting the x-ray diffraction pattern [59]. As the photon energy rises, more partial waves must be taken into account. For the photon energies 120 and 150 eV, 11 partial-waves contribute to the MFPAD [51]. As Hall and Siegel, and Cooper and Zare stated, the angular distribution is depending on the interference of the partial-waves [5, 6].

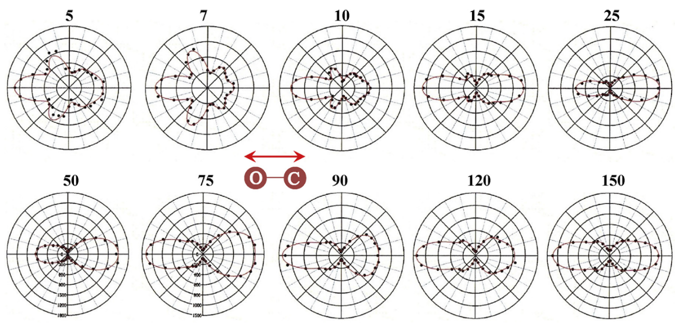

Figure 2.14: MFPADs from CO, emerging from the 1s orbital of carbon. The photo-electron kinetic energy [eV] is stated above each figure. Inset: Polarization axis and molecule orientation. Figure adopted from [51]

For 7-15 eV, Yagishita found $\ell 2$ and $\ell 3$ partial-waves add dominantly to shape of the MFPAD because of the σ* shape resonance in the C 1s ionization continuum [51]. The shape of the MFPADs elude from an f-partial-wave. The interference between the $\ell 2$ and $\ell 3$ partial-waves gives rise to a left-right asymmetry. This left-right asymmetry was first demonstrated by Heiser et al. in 1997 [60].

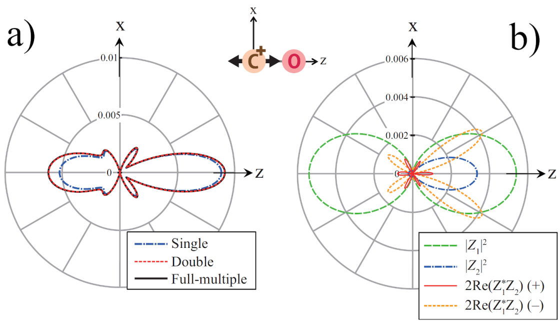

Figure 2.15: Calculated MFPAD for C 1s of CO, photon energy 150 eV, a) MFPADs with single (blue), double (red) and full-multiple scattering. b) Individual single scattering components. Excerpt from [59]

In a theoretical experiment, Kazama et al. calculated the MFPAD for C 1s of a CO molecule for a photon energy of 150 eV [59]. They calculated the transition amplitude $\langle\psi_p^-|\Delta|\phi_c\rangle$, with $|\psi_p^-\rangle$ the photoelectron wave function, and $|\phi_c\rangle$ the core wave function using a t-matrix expansion. The interested reader is referred to ref. [59] for the detailed calculation. The expansion reads as follows: $\langle\psi_p^-|\Delta|\phi_c\rangle = Z_1 + Z_2 + Z_3 + \ldots$. Z_1 represents the direct photoemission amplitude without scattering, Z_2 the single scattering amplitude and Z_3 the double scattering amplitude [59]. The calculated MFPAD for single ($|Z_1 + Z_2|^2$), double ($|Z_1 + Z_2 + Z_3|^2$) and full-multiple scattering is shown in fig 2.15 a). It is interesting to note that the MFPAD calculated with double and full-multiple scattering appear almost indistinguishable. The individual terms of the single scattering calculation are shown in fig 2.15 b). $|Z_1|^2$ follows a $\cos^2\theta$ distribution as it describes only the dipole transition s $\longrightarrow$ p [59]. As such, it also independent from the molecular structure since it does not contain any scattering components. The term $|Z_2|^2$ exhibits a striking left-right anisotropy leaning towards the oxygen atom. The interference part, divided in positive and negative contribution, reveals several lobes.

2.3.5 Strong field regime

Instead of absorbing a single high energetic photon to yield photoelectrons, it is also applicable to absorb multiple low energetic photons. In this case, much higher laser intensities are necessary. Such experiments have previously been conducted in our group [61–64]. Figure 2.16 shows the MFPADs obtained from benzonitrile. The molecules have been oriented with a static field of 467 $\mathrm{V\,m^{-1}}$ and aligned with approx. $7 \cdot 10^{11}$ $\mathrm{W\,cm^{-2}}$, centre wavelength 1064 nm. They were probed with an 800 nm pulse with an intensity of $1.2 \cdot 10^{14}$ $\mathrm{W\,cm^{-2}}$. Figures 2.16 a, c, e were probed with a left circularly polarized pulse (LCP), while figs b, d and f were probed with a right circularly polarized pulse (RCP). The unaligned MFPADs in figs a and b exhibit a minor up-down asymmetry since the static field is nevertheless present to cause a preferred orientation of the molecules. One-dimensionally orienting the molecules, figs 2.16 c and d, results in an up/total ratio of 55 % (44 %) for LCP (RCP) [61]. The asymmetry is more pronounced than in the unaligned case. Upon three-dimensional orientation a suppression appears, figs 2.16 e, f. The centre axis of the suppression coincides with the nodal plane of the HOMO and the HOMO-1. The opening angle $\Omega_{\mathrm{exp}} = 18° \pm 1°$ matches the theoretical prediction $\Omega_{\mathrm{theo}} \cong 18.8°$ [61].

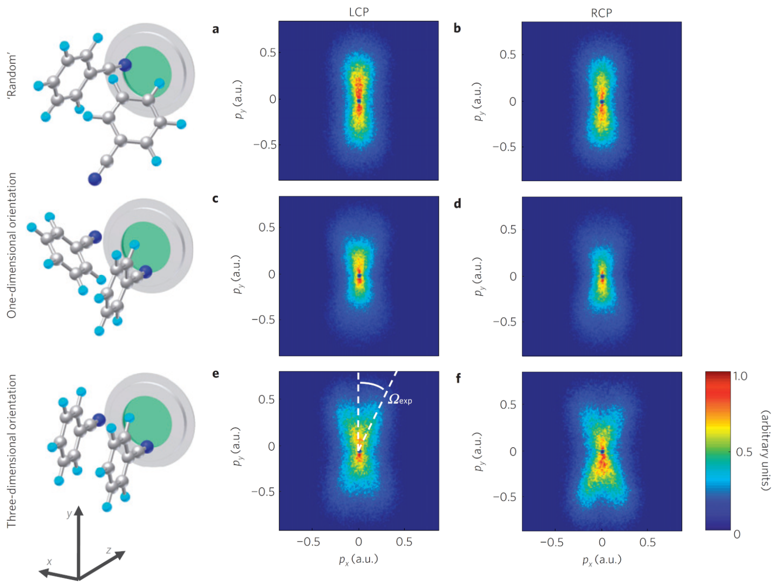

Figure 2.16: MFPADs from unaligned (a,b), one-dimensionally oriented (c,d) and three-dimensionally oriented (e,f) benzonitrile; probe pulse left-circularly polarized (a,c,e) and right-circularly polarized (b,d,f). Figure adopted from [61]

In another experiment, the three-dimensional photoelectron momentum distribution (PMD) of naphthalene has been reconstructed tomographically. The naphthalene molecules have been aligned three dimensionally with an elliptically polarized pulse, I=8$\cdot$ 10^{11}W cm^{-2}, centre wavelength 1064 nm and probed with a circularly polarized pulse, I=9$\cdot$ 10^{13}W cm^{-2}, centre wavelength 800 nm [63]. The geometry is shown in fig 2.17 a) for the elliptically polarized pulse with its major axis parallel to the plane of the detector. The two-dimensional MFPAD corresponding to this geometry is displayed in fig 2.17 c). If the molecules are three-dimensionally aligned perpendicular to the plane of the detector, the structure in the MFPAD is quenched, fig 2.17 b). Both cases exhibit a suppression at $p_{x,y}$=0. It is most pronounced at p_x=0 three-dimensionally aligned parallel to the plane of the detector. This suppression corresponds to the nodal planes of the HOMO [62]. Note, the laboratory frame coordinates in fig 2.17 are written as x,y,z and the molecular frame coordinates are primed, x', y', z'.

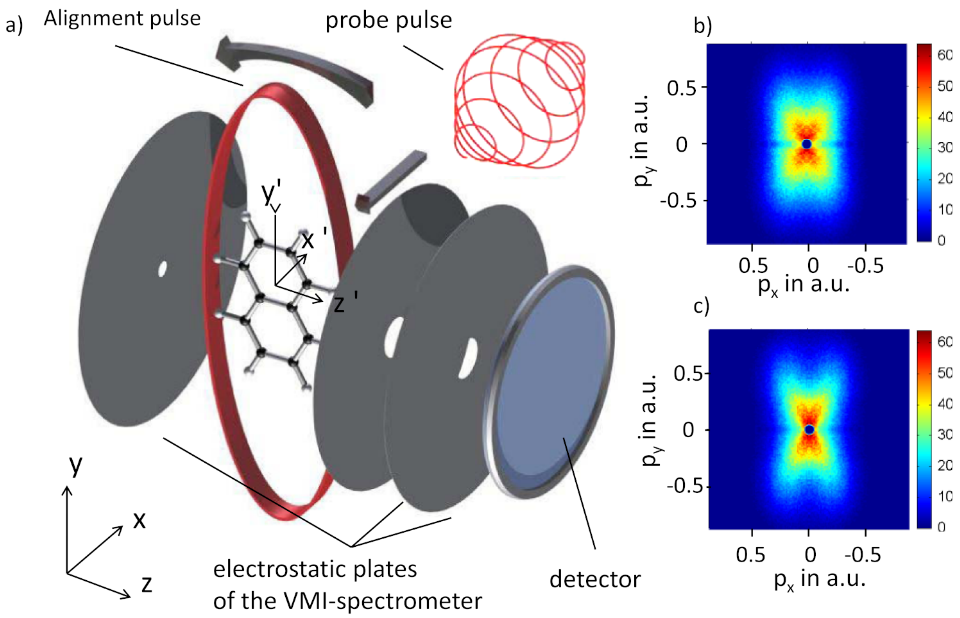

Figure 2.17: a) Geometry of the experimental setup: The naphthalene molecules are aligned with an elliptically polarized pulse (red elliptic ribbon), probed with a circularly polarized pulse (red spiral) and the VMI plates focus the photoelectrons onto the detector. b) MFPAD from naphthalene three-dimensionally aligned perpendicular to the plane of the detector. c) MFPAD from naphthalene three-dimensionally aligned perpendicular to the plane of the detector. Figure adopted from [63]

The data set for the three-dimensional tomographic reconstruction was obtained by turning the elliptic alignment pulse in 2° steps over 180°. An isosurface of the reconstructed three-dimensional MFPMD is presented in fig 2.18. It roughly resembles a torus with an indentation in the $p_{y'}p_{z'}$-plane and a hollow in x'-direction at $(p_{y'} = 0, p_{z'} = 0)$. The indentation arises from the aforementioned nodal planes. Another interesting feature of the three-dimensional MFPMD is the maximum of the photoelectron emission does not occur in the $p_{y'}$- or $p_{z'}$-direction, as fig 2.17 would suggest. The stretch of fig 2.17 c) compared to 2.17 b) is caused by the ionization yield.

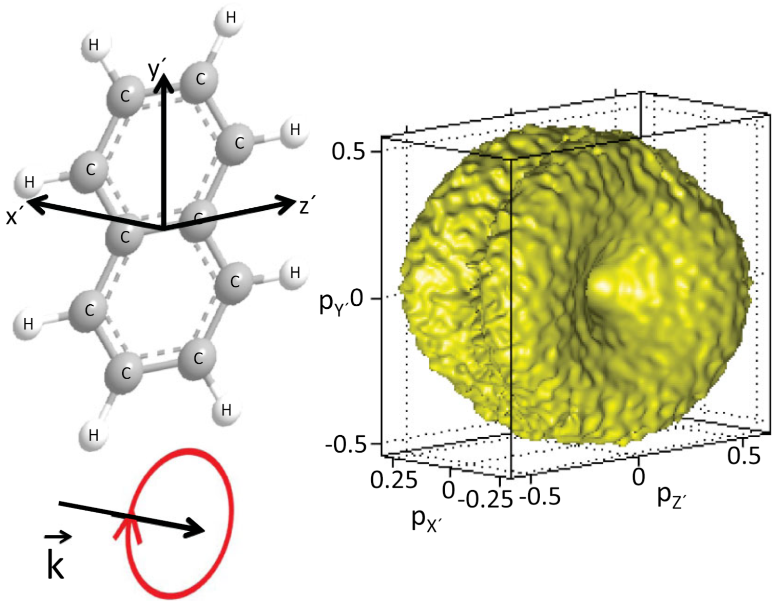

Figure 2.18: Tomographic reconstruction of the three-dimensional MFPMD. Left: Naphthalene molecule with right-circularly polarized probe pulse. Right: Isosurface plot of the reconstructed 3D MFPMD. Figure adopted from [63]

2.3.6 Time-resolved MFPADs

The first time-resolved PAD was reported in 1978 [65, 66]. Strand et al. excited atomic sodium to superposition of hyperfine states with a dye laser tuned to 588.99 nm. This excited state was probed with pulse from a N_2-laser, 337.1 nm. While the angle between both linearly polarized beams was fixed for one measurement, the polarization direction was tuned in 18°-steps [65, 67]. The photoelectrons emitted perpendicularly to the propagation axis of the laser beams were collected with a channeltron photomultiplier. They found the PAD a subject to change with the time delay between the two pulses and ascribed it to the changing interference among hyperfine levels.

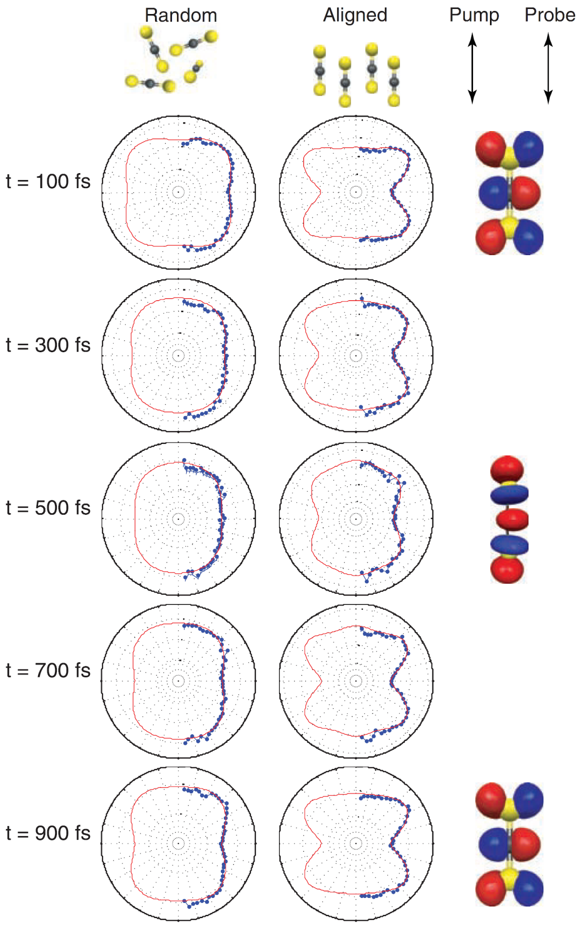

Figure 2.19: Unaligned PADs (left) and MFPADs (right) from CS_2 evolving with time, to the right: π*- (100 and 900 fs) and σ*-state (500 fs). Figure adopted from [68]

In 1999, Reid et al. documented time-resolved PADs with picosecond resolution for para-difluorobenzene [69]. More recently (2009 and 2011), time-resolved MFPADs with a time resolution in the fs-regime have been achieved in experiments with CS_2-molecules, see refs [68, 70]. The CS_2-molecules have been introduced to the laser interaction region in a jet-cooled molecular beam with helium as a carrier gas [68]. The rotational temperature was about 2 K [68]. They aligned the molecules non-adiabatically with a laser pulse with a centre wavelength of 805 nm and an intensity of $4{\cdot}10^{12}\,\mathrm{W\,cm^{-2}}$ [68]. During a revival, the molecules have been excited with a centre wavelength of 201.2 nm, 1 nJ/pulse and probed with 268.3 nm, 500 nJ/pulse to investigate the photodissociation reaction $CS_2 + h\nu \longrightarrow CS_2^* \longrightarrow CS(X) + S(^1D)/S(^3P)$ [68]. Three types of dynamics contribute to the photodissociation of CS_2: vibrational mode coupling, internal conversion and intersystem crossing [68]. When a nonbonding S atom is excited to a π^* orbital, the C-S bonds stretches and the equilibrium geometry is bent. At this bent geometry, neighbouring excited states can interact, which results in a mixing of electronic character. An optically dark state, i.e. a state that does not absorb a photon, the $^1\Pi_g$-state lies above the initial state $^1\Sigma_u^+$ [68]. These states cannot interact in the linear geometry. However, they do in the bent geometry. In this geometry the $^1\Pi_g$-state degenerates into two components of A_2 and B_2, see supplementary material of [68]. The component with B_2 exhibits a strong interaction with the $^1\Sigma_u^+$-state [68]. The MFPADs at t=100 fs and t=900 fs show the average of the electronic characters, while the MFPAD at t=500 fs exhibits the difference between them. Furthermore, fig 2.19 demonstrates the form of the MFPAD is oscillating between the sum and the difference signal, which is caused by the quantum beat phenomenon [68].

CHAPTER 3

Experimental setup

In this chapter I will describe the details of the experimental setup. The sections 3.1.2 – 3.1.6 are dedicated to the detailed description of the chambers, while the chapter 3.1.1 elucidates the differences between the old setup and the new setup. Section 3.1.7 provides an insight into the pumping capacities.

Parts of this chapter are reproduced and/or modified from my progress report. The sections 3.1.1 and 3.1.7 are reproduced from my progress report with slight adjustments. Figures 3.2 and 3.4 are modified versions of figures in my progress report. The optical setup is described in section 3.2.

3.1 Vacuum setup

The whole vacuum setup is shown in fig 3.1. The helium nanodroplet beam is formed by expanding helium gas through the nozzle attached to the cryostat (A) into the source chamber (B), see also section 2.1. As the beam crosses through the pickup chamber (C), the droplets pass a pickup cell, where they can be doped with the species of interest. The doped droplet beam, along with some effusive gas, i.e. unsolvated molecules, travels through the cold trap chamber (D), where the amount of effusive contaminating the target chamber (E) is reduced. The overall distance between the helium droplet nozzle and the centre of the velocity map imaging spectrometer (VMI), see section 3.1.5, is 123 cm. Alternatively, experiments can be performed by using a free gas jet, supplied by supersonic expansion in an Even-Lavie valve inside the supersonic

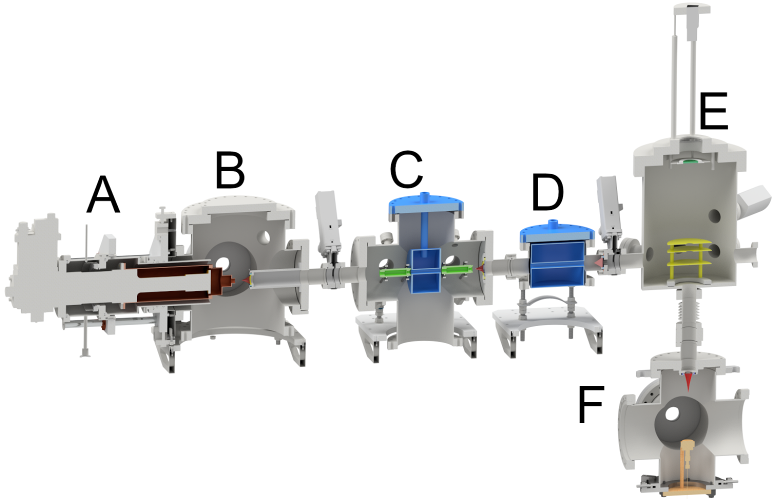

Figure 3.1: Vacuum setup: A - cryostat, B - source chamber, C - pickup chamber, D - cold trap chamber, E - target chamber, F - supersonic source chamber

source chamber (F), which is the modified source chamber of the old setup (B in fig 3.2).

The source chamber and the pickup chamber were initially designed by Benjamin Shepperson and are in use in a third experimental setup. I modified these designs to render them compatible to the parts of the old setup we would like to reuse. The cold trap chamber and the modifications to the old source chamber (B in fig 3.2) to turn it into the supersonic chamber of the new setup were entirely designed by me. The target chamber was reused as it was.

3.1.1 Difference between the new and the old experimental setup

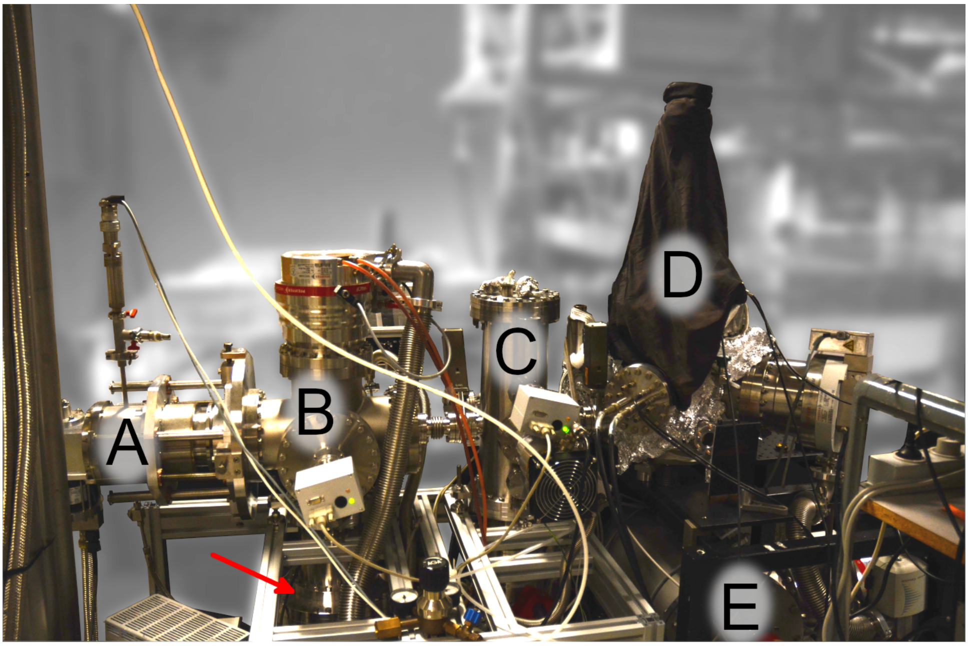

Figure 3.2: Photograph of the old experimental setup, taken 9th March 2017; The parts are: A — cryostat, B — source chamber, C — pickup chamber, D — target chamber, E — supersonic source chamber; The red arrow points to the reducing flange in between the source chamber and the Pfeiffer HiPace 2300 turbomolecular pump

In the old experimental setup, one pump, a Pfeiffer HiPace 2300, was connected via a CF160-flange, though it is designed to fit a CF250-flange (red arrow in fig 3.2). This reduced the effective pumping speed by 60%. With the new experimental setup, shown as an Autodesk Inventor drawing in fig 3.1, it is connected without reduction, see also fig 3.3.

As mentioned before, the new experimental setup has an additional chamber, hosting a cold trap (section 3.1.4). Also, the cold trap designs are different. In the old experimental setup, the cold traps were made of a reservoir of liquid nitrogen that was welded to the edge of a copper plate through which the droplet beam passes. In the new experimental setup, with the cryogenic traps of the pickup chamber and the cold trap chamber the trapping surface is a cylinder inserted in the liquid nitrogen reservoir, see sections 3.1.3 and 3.1.4. The cold traps are filled with liquid nitrogen, which has a temperature of 77.36 K [71].

As this is below the freezing point of water (273 K) or CO_2 (sublimation point 194.536 K [72]), these parts of any residual air can be trapped there effectively. Residual gases arise from two main sources: desorption from the chamber walls and impurities deliberately introduced into vacuum chambers. Though we evacuate the supply line that connects the leak valve and the reservoir of the species through a backing pump line, we entirely get rid of any air travelling along with the species at the very first opening of the valve. The pickup chamber (C in fig 3.1), cold trap chamber (D) and target chamber (E) are baked to obtain an ultrahigh vacuum (10^{-9} to 10^{-10} mbar), whenever considered necessary. One gas that is likely to be encountered inside them despite the baking is hydrogen [73]. However, the main purpose of the cold traps is to capture effusive dopant molecules. Since their boiling point is usually above that of nitrogen, they are likely to be trapped. For example, the boiling point of aniline is 267.11 K [74] and the sublimation point of naphthalene is 353.5 K [75].

The supersonic source chamber of the old experimental setup had an unnecessary large volume (fig 3.2 E). As the source chamber from the old experimental setup has a smaller volume and would not be used as such any longer, it was considered a suitable replacement. The Even-Lavie valve (section 3.1.6) is mounted on a flange connecting and sealing with a Viton O-ring. This kind of sealing allows the plate on which the valve is mounted to be moved and thus adjust and optimize the molecular jet with the skimmer's orifice. The source chamber from the old experimental setup is a six-way-cross, with DN160CF-flanges only. Thus the chamber had to be modified to host the desired connection type.

The cryostat in the photograph (fig 3.2 A) is a model RDK-408 D2 cryostat by Sumitomo Heavy Industries. In the new setup, the cryostat is a model RDK-415D cryostat. The cryostat units were swapped for maintenance reasons. Furthermore, the Even-Lavie valve in the old experimental setup was a model EL-7-2004-HT-LRR, while the new setup features a EL-7-4-2015-HRR,HT. This exchange was made because the high repetition rate valve (HRR) was spare at the time of the assembly.

3.1.2 Source chamber

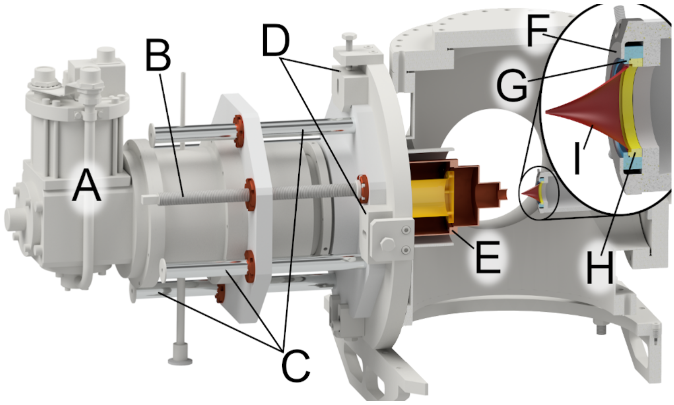

Figure 3.3: Source chamber, A –cryostat, B –manipulation bars (in beam direction), C –supporting bars, D –manipulation set (plane perpendicular to the beam), E –copper shields, F –clamp, G –top cover, H –bottom cover for the skimmer, I –skimmer (Beam Dynamics, Model 2, 1 mm orifice)

The main feature of the source chamber (fig 3.3) is the cryostat (Sumitomo Heavy Industries model RDK-415D), A in figs 3.3, 3.1 and also shown in fig 3.4, which is used as the helium nanodroplet source and is described in detail later. Additionally, the chamber also has skimmer (Beam Dynamics, Model 2, fig 3.3 I) with a 1 mm orifice in an initial distance of 16.5 mm to skim down to the coldest parts of the helium droplet beam. The skimmer is held by a top and bottom cover (fig 3.3, G and H) and this assembly can be moved by $\pm$ 2.50 mm inside the clamp (fig 3.3 F). The distance between the nozzle and the skimmer can be adjusted using two threaded manipulation bars (fig 3.3 B). Since the cryostat has a weight of 18.5 kg, blank bars were added to support it and ease the manipulation (fig 3.3 C). The cryostat position can also be adjusted perpendicular to the beam using four manipulation screws (fig 3.3, D). In case of a pump malfunction and thus a closed valve, the chamber could be pressurised by the constant flow of helium. To prevent any damage to the chamber or a safety hazard for people, an ASME[1] certified burst disk has been installed.

When (re-)installing the pickup cells, a HeNe laser beam is employed to model the helium droplet beam and align the cells. For ensuring the laser beam is aligned well through the skimmers and the pickup cells, the chamber also has a fused silica window.

[1] American Society of Mechanical Engineers

The cryostat

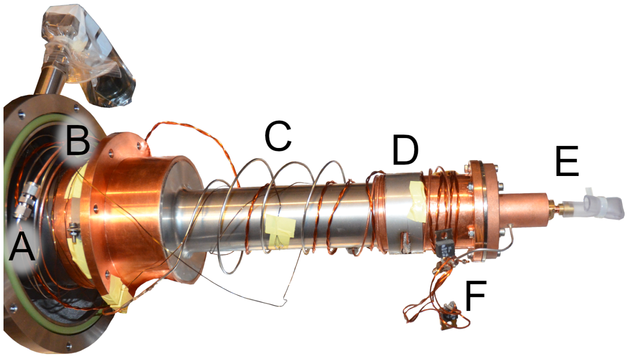

Figure 3.4: The cryostat: A – helium gas inlet, B – first cooling stage, C – thermally isolating stainless steel tubing, D – second cooling stage, E – nozzle assembly, F – heating resistors

Helium is circulating in a closed cycle inside the cryostat and this provides the necessary cooling for the helium that is used to generate the droplet beam. The compressor cycling the helium is a F-50Hw from Sumitomo Heavy Industries. The helium gas (AirLiquide Alphagaz, purity 99.9999%) used in the supersonic expansion is induced through 1/16″ of stainless steel tubing (A). It is followed by a coil of copper tubing (also 1/16″), that is clamped down to the first cooling stage (B). Here, it is cooled down to about 40 K [76]. Afterwards a piece of stainless steel tubing (C) leads it to the second cooling stage, where again, a copper tubing coil is clamped to the cryostat (D). The second cooling stage cools the helium down to approx. 4 K [76]. Since stainless steel has a smaller thermal conductivity than copper (16 $\mathrm{W\,mK^{-1}}$ to 413 $\mathrm{W\,mK^{-1}}$ [77]), it serves as thermal insulation. The nozzle assembly is also isolated with a stainless steel plate from the second cooling stage to maintain a stable temperature. Here, the helium gas is expanded through the nozzle (Plano GmbH, model A0200P) with an orifice of 5 µm at a backing pressure of 25 bar. Since the nozzle temperature influences the droplet size (subcritical and supercritical regime, section 2.1), heating resistors (F, Farnell MHP35 470F 47 Ω 1% 35 W) and a diode (silicon, DT-670B-CU by Lakeshore) are attached to the nozzle assembly and control the temperature in a feedback loop. The whole assembly is thermally and mechanically protected with a copper shield attached to the first cooling stage (B), which is not mounted in the provided image such that the tubing and wire are visible. It is pictured in fig 3.3 E. Furthermore, the heating resistors and the diode were not mounted and the nozzle is protected from clogging with a teflon hose sleeve, fig 3.4 E.

3.1.3 Pickup chamber

This chamber, fig 3.5, receives its name from the two subsequent pickup units (A), in which the helium droplets can be doped with the desired species. A pickup cell is a stainless steel cylinder with an inner diameter of 14 mm. It has two caps, one with an inlet orifice of 8 mm and an outlet with an opening of 3 mm. These diameters are a compromise between allowing the helium droplet beam to pass through the cell while keeping the dopant from evaporating into the chamber. The species is introduced to the cell via a Kurt Lesker leak valve, type VZLVM267. This valve connects to two DN40CF flanges, one facing the reservoir with the species, one connecting to the vacuum. The reservoir is usually a swagelok 1/4″ cap, filled with the desired compound. For this way of evaporating the sample into the cell, it needs to have a sufficiently high vapour pressure. For species with a low vapour pressure, it was planned to install an oven. However, due to manufacturing errors, the support rings are off-centred. The pickup cells are small enough to install them nonetheless, while the oven has a larger diameter and does not fit without disturbing the helium droplet beam. Two of the DN16CF-ports (D) were reserved for a thermocouple to connect to the oven.

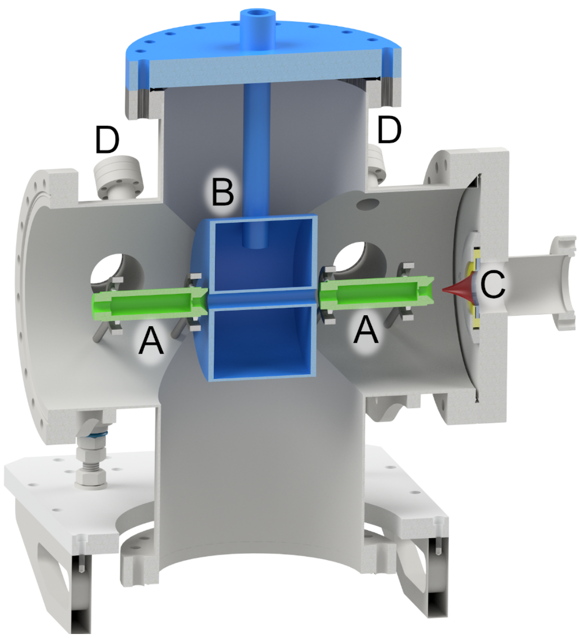

Figure 3.5: Pickup chamber: A - pickup cells, B - cold trap, C - skimmer, D - view ports/thermocouple feed throughs

In order to reduce the amount of effusive gas, the chamber also has a cold trap (B) and a skimmer (C, Beam Dynamics, model 2, orifice 2 mm). The skimmer can be moved $\pm$ 1 mm perpendicular to the helium droplet beam propagation direction. The cold trap has a volume of 0.8 l and a length of 80 mm in beam direction. The inner diameter of the cold trap was chosen to be 13 mm in order to account for any inaccuracies in the manufacturing process. The droplet beam passes through a cylindrical aluminium insert with a hole of ca. 2 mm.

3.1.4 Cold trap chamber

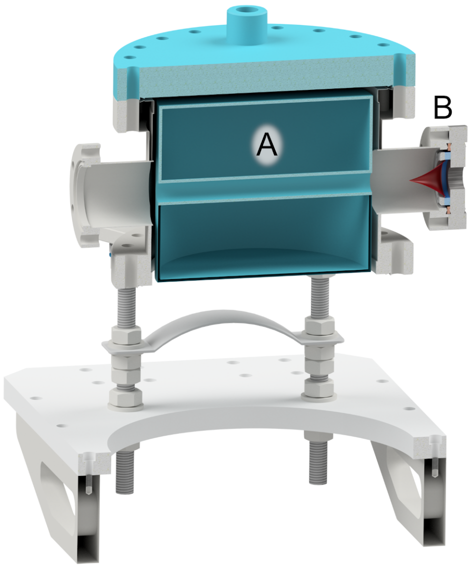

Figure 3.6: Cold trap chamber: A – cold trap (1.6 l), B – skimmer assembly

The cold trap chamber (fig 3.6) serves as a stage of differential pumping and also trapping effusive molecules. The cold trap (fig 3.6 A) here has a larger volume, 1.6 l, than the cold trap inside the pickup chamber and the helium droplet beam also crosses this cold trap at a length of 145 mm. As mentioned previously for the pickup chamber's cold trap, the inner diameter of the cold trap tube was chosen to be larger than the helium droplet beam, to account for any inaccuracies in the manufacturing process. The aluminium cylinder in this cold trap consists of two parts, press fit together, since a drill sufficiently long enough was not available. Additionally, this also ensures a straight hole.

A longer cylinder and a longer drill would increase the risk of the drill diverging from the intended direction.

Besides the cold trap, the chamber also hosts another skimmer, (fig 3.6 B, Beam Dynamics, model 2, orifice 2 mm). Due to the very confined spacing, this skimmer can only be moved by approx. 0.2 mm. With the two skimmers, the openings to the adjacent chambers are negligible compared to the DN160CF connection towards the pump. While the pickup chamber has two sources of incoming gas, the evaporating species and helium from the helium droplet beam, this chamber just has the helium droplet beam as a source of incoming gas and thus only traps or evacuates molecules. The chamber also has an additional volume of approx. 4.7 l towards the pump because the pump Leybold Turbovac 361 connects with an ISO160K flange, while the chamber has a DN160CF-connection. Therefore, an adapter has been inserted. With the small opening of 3.5 mm between the cold trap and the chamber walls the conduction is expected to be low, so one might expect a decrease in the pumping efficiency and thus a rise in the pressure. When the cold trap is filled, the measured pressure inside the chamber is in the 10^{-10}mbar region. It is to be emphasized that this pressure is measured outside the cold trap. The partial pressure inside the cold trap, especially close to the beam, is unknown. The effectiveness of the differential pumping could be confirmed in an experiment with acetylene. This species has a high vapour pressure, 48662.7 mbar [78]. The experiment has also been conducted on the aforementioned third setup. The contrast between effusive and signal yield were high in both cases: 18.45% in the third setup, 17.41 % in the presented setup. With the third setup, the pressure in the target chamber increased over time, which was detrimental to the achieved contrast. This was not observed with the presented vacuum setup. Since the third setup also has two cold traps between the helium droplet source and the target chamber, the difference is attributed to the differential pumping.

3.1.5 Target chamber

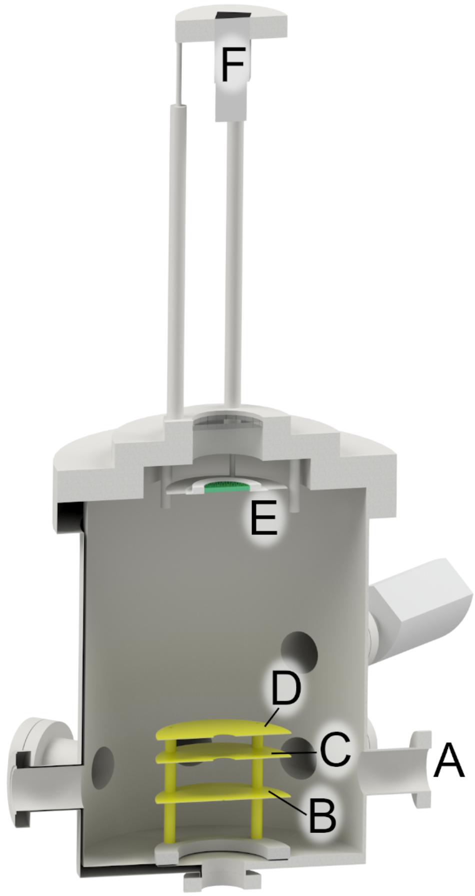

Figure 3.7: Target chamber: A – window for chamber alignment, B – repeller electrode, C – extractor electrode, D – electrode at ground potential, E – MCP and phosphor screen, F – camera

This chamber 3.7 contains the laser interaction region, the spectrometer and the detection unit. The laser beams cross the doped helium droplet beam and the free gas jet perpendicularly. The entrance window is a 5 mm thick 1″ UV enhanced fused silica window with an AR[2] coating for 250 – 400 nm and the exit window is a 4 mm thick 1.5″ UV enhanced fused silica window (both not visible in the figure). The first window needs to be small and thick, since the

[2]anti-reflective

	Electron Imaging	Ion Imaging
MCP front	0 V (ground)	-600 V
MCP back	1900 V	1200 V
Phosphor screen	4200 V	3800 V

Table 3.1: Operating voltages of the detector unit

larger windows are experiencing a larger torque bending them. A bent window introduces a birefringence, which is detrimental for the polarization. A third window is installed in the direction of the helium droplet beam fig 3.7 A. It is used to line up the chambers with the output of a HeNe laser and also for (re-) installing the pickup cells.

The species of interest interacts with the laser pulse(s) in the middle of two circular electrodes (diameter 110 mm), called the extractor (fig 3.7 C) and repeller (fig 3.7 B). For the images shown in chapters 5 and 6, the applied voltages were between -970 and -1015 V for the extractor and -1500 V for the repeller. Since the laser and the droplet beam or free gas jet do not interact always at the exact same spot between the two electrodes, the extractor voltage is adjusted to regain sharp velocity focussing. Together with a third electrode at ground potential (fig 3.7 D), these two electrodes form the velocity map imaging (VMI, see chapter 4) spectrometer, which focuses the electrons (or ions) onto the detector unit. This unit consists of a microchannel plate (abbr. MCP, fig 3.7 E, model Double MCP 50 by El-Mul Technologies Ltd) with an active diameter of 41.5 mm [79], followed by a phosphor screen (ScintiMaxP47, El-Mul Technologies Ltd) and a camera Allied Vision, model Prosilica GE 680 (fig 3.7 E). In electron imaging mode, the front of the MCP is grounded, while its back is set to a voltage of 1900 V, and 4200 V are applied to the phosphor screen. The voltages for ion imaging mode are given in comparison in tab 3.1. In ion imaging mode the front of the MCP is gated according to the flight time of the observed species. To increase the flight time and thus enhance the discrimination between the ions, a flight tube with a length of 294 mm is also available. In the time of flight mode all ions created by the interaction with the probe pulse are recorded with their travelling time, which depends on the mass to charge ratio.

3.1.6 Supersonic source chamber

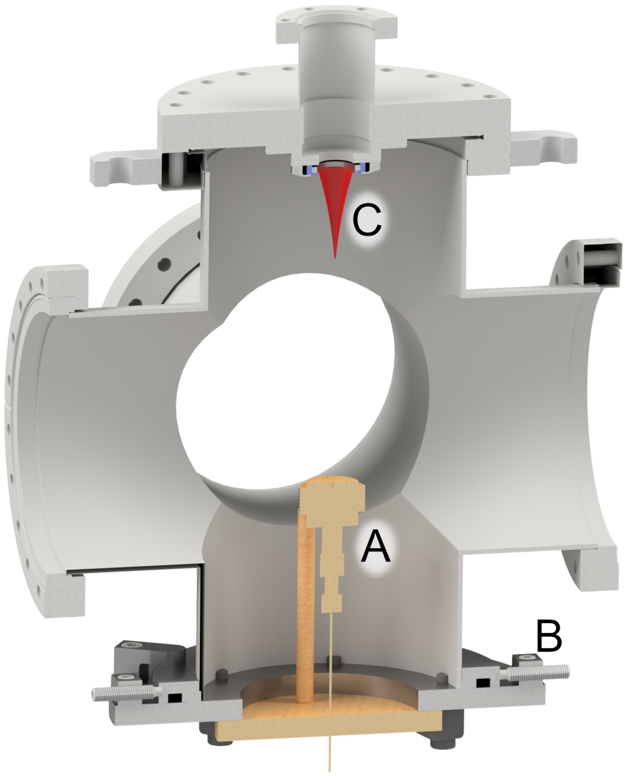

Figure 3.8: Supersonic source chamber: A – Even-Lavie valve, B – manipulating flange, C – skimmer assembly

Figure 3.8 shows the supersonic source chamber. It hosts an Even-Lavie valve, model EL-7-4-2015-HRR,HT[3] (fig 3.8 A) with a repetition rate of 1 kHz. It is mounted with an ISO100K to a manipulating flange (fig 3.8 B). The flange can be moved in the plane perpendicular to the free gas jet. It is only adjusted once with the assembly of the system to ensure the free gas jet hits the centre of the VMI stack. The valve can therefore be removed or reinstalled without the necessity to adjust its position. A skimmer (fig 3.8 C, Beam Dynamics, model 50.8) is installed in a distance of 130 mm to the valve.

[3]max pressure 100 bar, max temperature 250 °C

3.1.7 Pumping

Each chamber is pumped individually with a turbomolecular pump. These pumps are used to achieve an ultrahigh vacuum (10^{-8} mbar and lower). However, they are not suitable to work with atmospheric pressure at their exhaust and need a pre-vacuum (< 2 mbar), provided by foreline pumps. The above-mentioned pump supply lines connect the foreline pumps to the turbomolecular pumps. The source chamber has an individual backing line. The source chamber's turbomolecular pump is connected to a mechanical booster pump, mounted on a rotary vane pump. Formerly, this chamber was also connected to one rotary vane pump. The supersonic source chamber also has an individual pump supply line. The rotary vane pump, formerly installed to the source chamber, was installed to this line as it became spare. These two chambers have a high throughput of gas, that is otherwise not desired to influence the pumping of the other chambers. In contrast to this, the pickup chamber, the cold trap chamber and the target chamber share a backing line to a rotary vane pump. An overview of the pumps used and their pumping speed is given in tab 3.2.

Foreline Pumps		
Chamber(s)	Pump	Pumping speed [$\mathrm{m^3\,h^{-1}}$]
Source, supersonic source	Pfeiffer DUO 65	70 [80]
Source	Edwards Booster EH500 Hyd	400 [81]
Pickup, cold trap and target	Leybold Trivac D16B	16 [80]
Supersonic	Edwards 28	27.5 [82]
Turbomolecular Pumps		
Chamber	Pump	Pumping speed [$\mathrm{l\,s^{-1}}$]
Source	Pfeiffer HiPace 2300	1900 [80]
Pickup	Pfeiffer TMU 521	520 [80]
Cold trap	Leybold Turbovac 361	400 [83]
Target	Pfeiffer HiPace 700	685 [80]
Supersonic	Pfeiffer HiPace 700	685 [80]

Table 3.2: Overview of foreline and turbomolecular pumps for the various vacuum chambers

The pump speeds of the foreline pumps are limited by the conductance of the tubes connecting them to the turbomolecular pumps. The conductance can be estimated by the following formulae, giving the result in l/s [73]:

$$C = 180\frac{D^4}{L}P_{av} \tag{3.1}$$

$$C = 12\frac{D^3}{L} \tag{3.2}$$

with:
D – tube diameter [cm]
L – tube length [cm]
P_{av} - average pressure in the tube [torr]

While eq 3.1 can be used in the viscous flow region, eq 3.2 is used in the molecular flow region, in which the mean free path far exceeds the tube diameter [73]. As can be seen easily, the conductance highly depends on the tube diameter. The chosen tube diameters are 5 cm for the supersonic source chamber's backing line and the pickup, cold trap, and target chamber's backing line. With the source chamber, we expect a high throughput of helium gas, so a larger tube with a diameter of 10 cm was chosen, resulting in a 16 times larger conductance as if a tube of 5 cm had been chosen instead.

The net pump speed S can be calculated from the initial pump speed S_p and the conductance C [73]:

$$\frac{1}{S} = \frac{1}{S_p} + \frac{1}{C} \tag{3.3}$$

As the pressure influences the conductance in the viscous flow region, two calculations were performed: One with the total pressures according to the individual manual and another one with the pressures measured in the backing lines. The results can be found in the tabs 3.3 and 3.4. The mean free path expected for the given pressures is roughly below 5 cm [73], except for the measured pressure in the supersonic's backing line (5.0 10^{-4} mbar), here it can be estimated as between 5 and 50 cm. This presents a case in between the viscous and molecular flow region. For this region a more detailed analysis would be necessary. Thus, both values are given in tab 3.4, with the value calculated in the viscous flow region giving a conservative value, likely to underestimate the net pump speed. The backing lines have the following lengths (connecting to the chamber): 1461 cm (source chamber), 1550 cm (pickup, cold trap and target chamber), and 1531 cm (supersonic source chamber).

pump	pump speed [$\mathrm{l\,s^{-1}}$]	p_{manual} [mbar]	net S [$\mathrm{l\,s^{-1}}$]
Pfeiffer Duo 65	19.44	0.002 [84]	1.69
Edwards Booster EH500	111.11	0.02 [85]	15.85
Leybold Trivac D16B	4.44	0.002 [86]	0.11
Edwards 28	7.68	0.001 [82]	0.05

Table 3.3: net speed of the pumps, using the total pressures according to the manuals

pump	pump speed [$\mathrm{l\,s^{-1}}$]	p_{measured} [mbar]	net S [$\mathrm{l\,s^{-1}}$]
Pfeiffer Duo 65	19.44	0.0255	10.65
Edwards Booster EH500	111.11	0.0195	15.51
Leybold Trivac D16B	4.44	0.00257	0.14
Edwards 28	7.68	0.0005	0.03 (0.86)

Table 3.4: net speed of the pumps, using the measured pressures in the backing line, the value in brackets is calculated with the conductance in the molecular flow region

The pressures were measured close to the setup. Closer to the foreline pump they are likely to be lower [73], which also indicates that the calculated net pump speed is probably underestimating the real value.

3.2 Optical setup

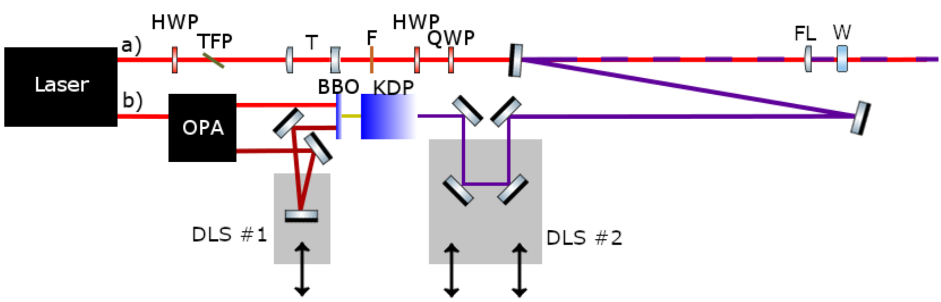

Figure 3.9: Schematic laser setup: a) Alignment arm: power control (half-wave plate (HWP) and thin film polarizer (TFP)), spot size control (T, telescope – planoconvex and planoconcave lens), truncation (longpass filter), polarization control (half-wave plate (HWP) and quarter-wave plate (QWP); b) Probe arm: OPA output 800 nm and e.g. 2117 nm, collinearly overlapped into the BBO, frequency-doubled with the KDP. Both beams are overlapped collinearly and focused with a 30 cm lens (FL) through a window (W) into the chamber. DLS - delay stage. All non-labelled items are dichroic mirrors. Parts of the figure have been composed using the component library of [87].

The laser system (customized Solstice ACE, model 80L-35F-1K-HP-T Spectra-Physics, 1 kHz, 6 W, 40 fs) has two outputs: A compressed (FWHM ~45 fs, fig 3.9 b)) and an uncompressed one (FWHM ~300 ps, fig 3.9 a)), both with a centre wavelength of 800 nm. The uncompressed arm the uncompressed arm is used to align molecules via laser-induced alignment (section 2.2), while the compressed is introduced into an optical parametric amplifier (abbr. OPA, model TOPAS prime, TP8U1, by Light Conversion). The TOPAS provides three different beams: the signal, the idler and a residual 800 nm beam. The signal and the idler overlap in space and time, but vary in polarization (idler parallel to the plane of incidence, signal perpendicular to the plane of incidence).

Figure 3.9 shows a scheme of the laser setup used in the experiments described in the chapters 5, 6 and 7. The probe pulse is in the UV regime, generated by sum frequency generation (SFG). First, pulses of 800 nm and e.g. 2117 nm centre wavelength (idler) are collinearly overlapped in a 0.5 mm thin BBO crystal cut to an angle of 22.4°.

The polarization of the 800 nm pulse is also parallel to the plane of incidence, so it matches the idler's polarization. The signal pulse is still present, however since its polarization is perpendicular to the plane of incidence, it does not interfere with the SFG. The beam, resulting from the mixing in the BBO crystal, is frequency doubled in a 40 mm long KDP crystal, in this example giving a centre wavelength of 293.85 nm. The long crystal ensures a narrow bandwidth (0.06 nm, FWHM, fig 3.10 a-c), with the compromise of expanding the pulse duration to an overall length of 6 ps (fig 3.10 d) inlet). The spectrometer's resolution is limited to 0.06 nm. Thus the actual spectral bandwidth might even be narrower than this. However, the experimentally determined temporal FWHM is still in the femtosecond-regime, 585 fs (fig 3.10 d) inlet). The cause for the asymmetric temporal pulse shape is also found in the length of the crystal. When the fundamental pulse enters the crystal, the conversion is at a maximum, giving rise to the peak, seen in fig 3.10 d) inlet. While the phase velocities match, the group velocities of the two wavelengths mismatch. The fundamental propagates with a group velocity higher than the group velocity of the second harmonic. During its propagation less and less of the second harmonic is generated as the intensity of the fundamental is decreasing since it is converted. However, the peak of the second harmonic pulse needs to propagate through the crystal after the generation. Thus the part of the second harmonic that was created last, leaves the crystal first.

For each conversion along the propagation of the fundamental pulse, one can assume the temporal walk-off as the limiting factor. The group velocity mismatch of 281 $\mathrm{fs\,mm^{-1}}$ [88] suggests that the second harmonic and fundamental (estimated pulse duration ~120 fs) walk-off within 0.4 mm. The phase-matching follows a sinc-function, which reaches a minimum at Π. The minimum marks the minimum of the achievable spectral bandwidth:

$$\operatorname{sinc}\left(\frac{\Delta k L}{2}\right) \stackrel{!}{=} \pi \underset{\Delta k = \frac{\Delta\lambda 2 \cdot \pi n}{\lambda^2}}{\Longrightarrow} \Delta\lambda = \frac{1}{L}\frac{\lambda^2}{n} \tag{3.4}$$

This leads to a Δλ of 0.53 nm, which is an order of magnitude higher than the measured spectral bandwidth. Thus, a temporal walk-off is not the limiting factor.

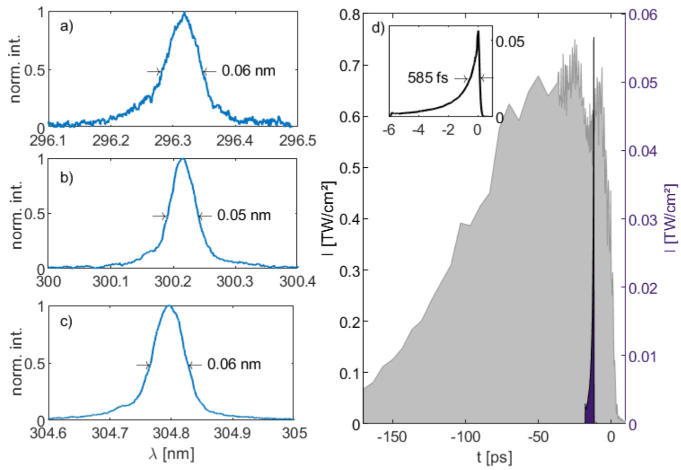

Figure 3.10: a,b,c) spectral shape of the probe pulse, data: courtesy of A.S. Chatterley, centre wavelength a) 296.3 nm, b) 300.2, c) 304.8 nm; d) temporal shape of the pulses, grey: alignment pulse, purple: probe pulse, inlet: probe pulse

The intensity of the alignment pulse, i.e. the uncompressed output of the laser (fig 3.9 a), is controlled by varying its polarization with a half wave plate (HWP) followed by a thin film polarizer (TFP), fig 3.9. With a telescope in the alignment arm it is ensured that the spot size of the alignment pulse is bigger than the spot size of the probe, so preferably only aligned molecules are probed. The alignment beam is truncated with a longpass filter, as described in ref [42] (FWHM after truncation: 110 ps, fig 3.10 d). The following HWP and quarter-wave plate (QWP) were varied to obtain the desired polarization. The alignment and the probe beam are overlapped collinearly. Both beams are focused into the target chamber with a custom made planoconcave achromatic doublet lens with a focal length of 300 mm. It is AR coated for 266, 305, 800 and 1064 nm.

CHAPTER 4

Velocity map imaging

Chandler and Housten first documented an imaging technique capable of recording the spatial distribution of photofragments [89]. They imaged the CH_3^+ fragment of the photodissociation of CH_3I using a quadrupled Nd:YAG laser beam (266 nm) to photodissociate the molecules and a dye laser (ca. 330 nm) to ionize the CH_3 fragment [89]. It is interesting to note that they also reconstructed the three-dimensional distribution exploiting the cylindrical symmetry [89].

This imaging technique was further improved by Eppink and Parker as they introduced velocity map imaging [90]. With this method, the velocity rather than the spatial distribution is imaged. They employed two photons of 225 nm to excite the O_2 molecules to a Rydberg state [90]. The absorption of a third photon excites the molecule to a super-excited state 16.53 eV above ground level, from where the molecules photodissociate [90]. The O^+ ions and electrons with energies ranging from 0-4 eV resulting from the photodissociation were imaged.

Since then, velocity map imaging has been used in a variety of applications, see ref [91] for a review. It has been used for, e.g. the study of inelastic collisions, neutral-neutral reactions, photo-initiated and electron-initiated processes [91].

In the following section, I am going to briefly recapitulate the operating mode of the VMI spectrometer. In the chapters 5, 6 and 7, I am using Abel inversion, which is explained in section 4.2. Furthermore, the VMI spectrometer has been calibrated using iodobenzene, which is elucidated in section 4.3. Additionally, the electron velocity map images presented in the chapters 5 and 6 are shown on a radial scale. The difference to normal imaging is also shown in section 4.3.

4.1 Operating mode

The principle units of a VMI spectrometer are shown in fig 4.1, together with the Even-Lavie valve. A molecular beam is produced with the Even-Lavie valve (ELV in fig 4.1) and passes through a skimmer. In the laser interaction region, it is crossed at a 90° angle with the laser pulse(s) (red arrow in fig 4.1) and is ionized. The laser interaction region is found in the centre of two circular electrodes, the extractor (Ex in fig 4.1) an repeller (R in fig 4.1). A third electrode at ground potential ensures a field-free region between the third electrode and the two-dimensional imaging detector (2DID in fig 4.1). These three electrodes form an electrostatic lens, which project the electrons onto the two-dimensional imaging detector. This detector consists of an MCP, a phosphor screen and a camera, see section 3.1.5. The electrodes with the detector unit form the VMI spectrometer similar to the VMI spectrometer described by Eppink and Parker.

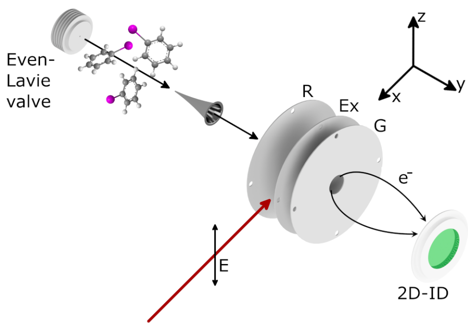

Figure 4.1: VMI spectrometer with molecular beam and laser beam (electric field E). With: Even-Lavie valve, 2DID - two-dimensional imaging detector, R - Repeller, Ex - Extractor, G - electrode at ground potential

4.2 Abel inversion

Using a two-dimensional imaging detector comes with one disadvantage: Only the velocities in the plane of the detector (xz-plane, fig 4.1) are resolved. This is illustrated in fig 4.2. Molecules are ionized with a laser with its polarization parallel to the z-axis. The VMI electrodes (ion optics in fig 4.2) project the electrodes onto the detector. In the field-free space the three-dimensional electron velocity distribution is displayed. It is a Newton sphere, cylindrically symmetric around the z-axis. Once the Newton sphere is projected onto the detector, the resulting distribution F is depending on (x, z). The information about the velocity distribution in y-direction is lost. It can be retrieved through Abel inversion.

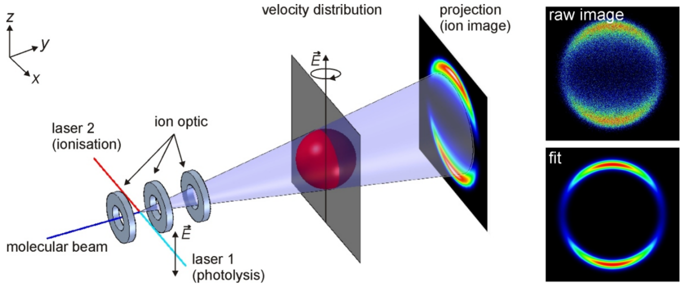

Figure 4.2: Velocity map imaging and Abel inversion. Figure adopted from [92]

First, the Abel transform projecting $f\,(r,z)$ onto $F\,(x,z)$ shall be considered. After the ionization, the three-dimensional cylindrical symmetric distribution, $f\,(r,z)$, with $r^2 = x^2 + y^2$ is projected onto a two-dimensional surface in the following manner, using an Abel transformation:

$$F\,(x,z) = \int_{-\infty}^{\infty} f\,(r,z)dy = 2\int_{0}^{\infty} f\,(r,z)dy \tag{4.1}$$

The variable r depends on y as $r^2 = x^2 + y^2$. Thus, the infinitesimal element dy can be replaced with the following substitution:

$$dy = \frac{r}{\sqrt{r^2 - x^2}}dr \tag{4.2}$$

$$F\,(x,z) = 2\int_{|x|}^{\infty} \frac{f\,(r,z)\,r}{\sqrt{r^2 - x^2}}dr \tag{4.3}$$

The distribution $F\,(x,z)$ is the two-dimensional image observed on the detector. To calculate the initial three-dimensional distribution, the transformation needs to be reversed:

$$f\,(r,z) = -\frac{1}{\pi}\int_{|r|}^{inf} \frac{F\,(x,z)}{dx}\frac{1}{x^2 - r^2}dx \tag{4.4}$$

The requirement to use Abel inversion is cylindrical symmetry. Thus, only electron velocity map images that match two experimental geometries can be Abel inverted. The cylindrical symmetry is fulfilled if only the probe pulse is present or if the polarization of the alignment pulse is also parallel to the z-axis as the probe pulse. The presented analysis is using cartesian coordinates.

In practice, the images have been Abel inverted using the polar onion peeling (POP) algorithm introduced by Roberts et al. [93]. The algorithm was implemented in Matlab as found in resource [94]. As the name implies, this method uses polar coordinates and "peels" the image like an onion. The "peeling" means that the algorithm subtracts the contributions of outer shells from the inner part of the image [93]. Each shell is fit using Legendre polynomials of the order n [93]. The image $I(\theta)$ is thus reconstructed using an intensity factor $N(r)$ and the anisotropy parameters β_n:

$$I(\theta) = N(r) \sum_n \beta_n P_n(\cos\theta) \tag{4.5}$$

4.3 VMI calibration

The VMI spectrometer has been calibrated using iodobenzene as a reference system. Iodobenzene has been fragmented using 304.59 nm with an intensity of approx. 0.8 TW cm^{-2} and the iodine atom has been used to calibrate the system with a resonant [2+1]-photoionization. The iodine atom has an ionization potential of 10.45 eV [95] and the addressed state is the iodine state 5 p^4(^{3}P$_2$)6 p with J=7/2 at 65670 cm^{-1} (8.14 eV) [96]. Thus, two photons of 304.59 nm (4.07 eV) need to be absorbed to excite this state and a third photon ionizes the atom. The resulting photoelectron has a photoelectron kinetic energy of 1.76 eV.

The raw electron velocity map image of this photoionization can be seen in fig 4.3 a) on a radial scale, i.e. the electron signal has been multiplied with the radius. The photoelectrons with a kinetic energy of 1.76 eV can clearly be seen as a ring with an excess of signal parallel to the z-axis. Furthermore, there are two dark spots visible. The centre of the image is dark due to the scaling and close to it is another dark spot, off-centred. This is a burn in the detector. As a comparison the same image is presented on a normal scale next to it, fig 4.3 b). The photoelectrons with zero kinetic energy are the most dominant in this image and the ring of photoelectrons with a kinetic energy of 1.76 eV can hardly be seen. Figure 4.3 c) shows a centre cut employed on electron velocity map image as fig 4.3 b). The most dominant peak in the centre is cut out and the ring becomes visible again. With radial scaling such a centre cut is not necessary, while the features with less signal than the centre peak of electrons with zero kinetic energy are clearly visible. The images in the chapters 5 and 6 are presented with a radial scaling, while the images in chapter 7 are shown on a normal scale.

Figure 4.3 d) shows the Abel inverted image. The ring at 1.76 eV can clearly be seen. Additionally the signal of the projected Newton sphere, see fig 4.2 is gone. The image presents a slice of the three-dimensional electron velocity distribution.

The radial distribution of the Abel inverted image has been extracted and calibrated to a photoelectron kinetic energy distribution. The result is shown in fig 4.3 e). The peak at 1.76 eV has a FWHM of 0.155 eV, which leads to a resolution of 9%.

Electron velocity map images have been recorded for different repeller voltages and a calibration function has been determined. The resulting calibration for the photoelectron kinetic energy as a function of the repeller voltage and the Abel inverted radius is:

$$E\,(eV) = r^2 * U_{rep} * 8.9366 \cdot 10^{-8} * \frac{\mathrm{eV}}{\mathrm{px}^2 V} \tag{4.6}$$

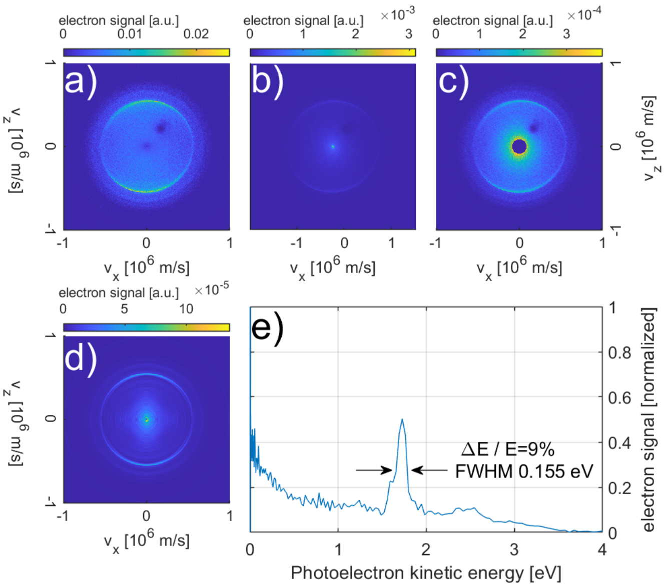

Figure 4.3: VMI calibration with an electron velocity map image of electrons obtained from iodobenzene, probe wavelength 304.59 nm. a) Electron velocity map image on radial scale b) Electron velocity map image on normal scale c) Electron velocity map image on normal scale with centre cut d) Abel inverted electron velocity map image e) Photoelectron kinetic energy spectrum obtained via Abel inversion

It is dutifully noted that an Abel inversion of a radial scale image would distort the Abel inverted image and hence the photoelectron kinetic energy distribution. Thus Abel inversion is only performed on normal scale images. Furthermore, the data for the angular distributions are also extracted from the normal scale data sets.

CHAPTER 5

Aniline

Aromatic amino acids, e.g. phenylalanine, tryptophan and tyrosin take part in the biosynthesis of proteins. Aniline is an aromatic amine consisting just of a phenyl ring and an amino group (fig 5.1) and as such, it has experienced great popularity as a simple model system for aromatic amino acids. It has been investigated using IR spectroscopy [97], zero kinetic energy photoelectron spectroscopy [98], mass analyzed threshold ionization [99], electronic spectroscopy [100], photoabsorption spectroscopy [101] and also resonant enhanced two-photon ionization [102], to name but a few. Furthermore, it has been investigated in time-resolved (ultrafast) experiments [103–105] and theoretical experiments [106].

Its symmetry can be approximated as C_{2V}, although the amino group is not exactly in plane with the phenyl ring. Thus, the correct symmetry is C_S. However, in its first cation state, D_0, the geometry changes to be planar [102]. Interestingly, the transition dipole moment for the $S_1 \leftarrow S_0$ transition is perpendicular to the most polarizable axis (MPA, C-N axis), fig 5.1 [100]. On the other hand, the polarizability anisotropy of aniline is fairly small, tab 5.1. As the achievable alignment increases with the polarizability anisotropy (eq 2.10), aniline does not align well compared to molecules with a larger polarizability anisotropy, such as naphthalene.

Table 5.1: Polarizability and rotational constants of aniline, most polarizable axis (MPA) and second most polarizable axis highlighted, B3LYP/aug-cc-pVDZ [107, 108]

Polarizability [Å^3]			
	x	y	z
x	7.601	-0.007	0.000
y	-0.007	**15.907**	0.000
z	0.000	0.000	**13.195**
Rotational constants [GHz]			
	1.768	5.593	2.579

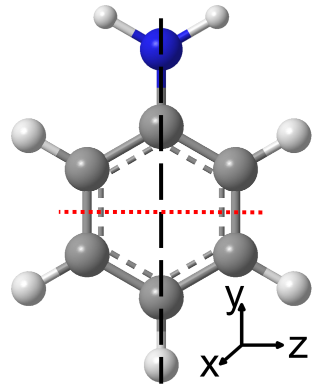

Figure 5.1: Structure of aniline: most polarizable axis (MPA): C-N axis (dashed black line), $S_1 \leftarrow S_0$ transition dipole moment (dotted red line)

5.1 Laser-induced alignment of aniline molecules

In this section I make numerical estimates for the degree of alignment for one-dimensionally aligned aniline molecules. As mentioned previously, a high degree of alignment is important to achieve MFPADs [48] and thus the degree of alignment is relevant for the PADs reported in the sections 5.3.2, 5.3.4 and 5.3.5. One-dimensional alignment is induced by a linearly polarized laser pulse and confines the most polarizable axis to the polarization axis of the laser pulse, see also section 2.2. The degree of alignment has been estimated using the alignment calculator briefly explained in section 2.2.3. For this calculation, the actual pulse shape of the truncated alignment pulse is used, see grey area fig 5.2 b). This pulse adiabatically turns on in about 150 ps, has a FWHM of 110 ps and rapidly turns off in ca. 10 ps.

To use the alignment calculator, aniline, an asymmetric top rotor, is approximated as a symmetric top rotor. As a conservative estimate, the highlighted polarizabilities in tab 5.1 have been used to calculate the polarizability anisotropy and with it the degree of alignment (see sec 2.2) in the following manner:

$$\Delta\alpha = \alpha_{yy} - \alpha_{zz} = 2.712\,\text{Å}^3 \tag{5.1}$$

It is likely to underestimate the true degree of alignment, since the most polarizable axis and the least polarizable axis exhibit a significant difference in polarizability (x- and y-direction, see tab 5.1). Thus, the least polarizable axis is likely to be confined perpendicular to the polarization direction, which is not considered with this approximation. Instead it focusses on the most and secondmost polarizable axis competing with one another, still favouring the most polarizable axis over the second most polarizable axis. The strongest degree of alignment occuring at the peak of the pulse for this case is given in fig 5.2 a) in blue.

Another approach, also considering the least polarizable axis, is to calculate $\langle\cos^2\theta\rangle$ with an averaged polarizability anisotropy, according to eq 5.2. The resulting strongest degree of alignment occuring at the peak of the pulse is given in fig 5.2 a) in red.

$$\Delta\alpha = \alpha_{yy} - \frac{\alpha_{xx} + \alpha_{zz}}{2} = 5.509\,\text{Å}^3 \tag{5.2}$$

An example for a calculated alignment trace is shown in fig 5.2 b). The chosen intensity, 0.81 $\mathrm{TW\,cm^{-2}}$, was used in the experiments, if not stated otherwise. It represents the compromise between maximizing the degree of alignment and minimizing other effects of the alignment pulse on the molecule besides aligning. In the beginning of the pulse, t=-200 ps, the molecules are randomly oriented, which results in a degree of alignment of $\langle\cos^2\theta\rangle = 0.33$. As the pulse adiabatically turns on, the degree of alignment also rises. The strongest alignment occurs at the peak of the pulse and is marked in both subfigures as A. With the truncation of the pulse, the molecules do not experience the torque of the aligning electric field any more and start to rotate freely again. The decrease in the degree of alignment appears retarded to the decrease in the alignment pulse. Previous research suggests a small window of about 2 ps for field-free alignment in this case [42]. However, as long probe (6 ps) pulses are used in the presented experiments, this window is insufficient to carry out the experiment under field-free conditions. Furthermore, as the calculation assumes a symmetric top rotor, the calculated window is likely to be larger than the experimental one. After the truncation of the pulse, the rotational wave-package re-phases. At t=46.4 ps a quarter- revival occurs with a degree of alignment of $\langle\cos^2\theta\rangle = 0.42$, leaving the molecules anti-aligned. It is followed by half-revival at t=91.0 ps with a degree of alignment of $\langle\cos^2\theta\rangle = 0.58$. As the calculator assumes a symmetric top rotor, only J-type revivals are considered. Furthermore, their respective timing and the resulting degree of alignment can also not be expected to represent the experimental value. Additionally, asymmetric top rotors can also exhibit C-type revivals (see sec 2.2.5), which are not represented in this calculation.

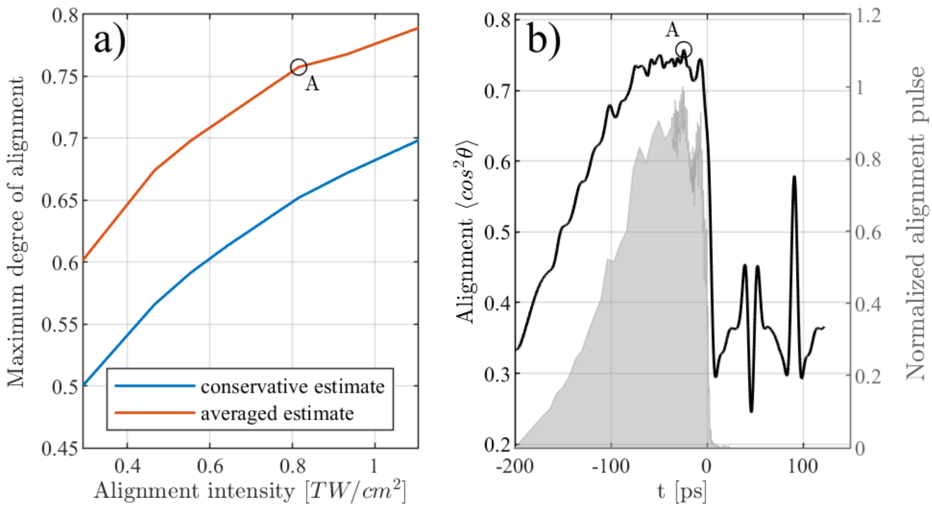

Figure 5.2: a) Maximum degree of alignment, conservative and averaged estimate b) Calculated alignment trace ($a_{\|}$=15.907 Å^3 $a_{\perp}$=10.398 Å^3) with alignment pulse shape; A: strongest degree of alignment occuring at the peak of the pulse

5.2 Ionization pathways

An advantage of aniline as the investigated species is its relatively isolated vibrational bands, accessible with the laser bandwidth of 0.06 nm. Furthermore, its S_1-state (34031 $\pm$ 3 cm^{-1} [102]) and D_0-level (62271 $\pm$ 6 cm^{-1} [102]) are favourable for a [1+1]-photoionization with our UV light source. The ionization scheme is presented in fig 5.3 a). One UV photon with [34031+798] cm^{-1} excites the molecule to the vibrational mode 1^1 of its first electronically excited state, the S_1-state. With the absorption of a second UV photon the molecule is ionized to the D_0-state. Figure 5.3 b) provides a zoom on the absorption of the second UV photon. The cation is left in its ground state or e.g. the $8a^1$ state.

However, with the alignment pulse present, other ionization channels including the electronically excited states S_2 and S_3 (3s Rydberg state, “new S_2”, in the notation of Ebata et al. [97]), are available as well. After absorbing one UV photon, the molecule in the first excited state (S_1) can absorb an IR photon 12500 cm^{-1}. This leads to a decay into the S_2 or S_3 state. The absorption of another UV photon ionizes the molecule. The suggested photoionization process is therefore a [1+1'+1]-photoionization, the primed number referring to an IR photon.

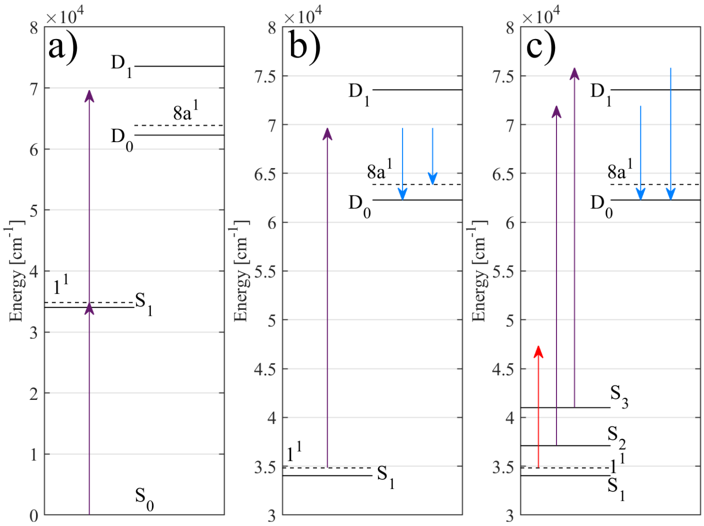

Figure 5.3: a) [1+1]-Photoionization targeting the 1^1-vibrational mode of the S_1-state b) Zoom on the absorption of the second photon, leaving the cation in the ground state and its $8a^1$-vibrational mode c) Rivalling photoionization channel through the absorption of a photon of the alignment pulse, including the electronically excited states S_2 and S_3 states. Purple arrows: UV photons, red arrow: IR photon, blue arrows: photoelectron kinetic energy

5.3 Gas phase experiments

5.3.1 R2PI

Figures 5.4 and 5.5 show resonant two-photon ionization spectra (R2PI) of gas phase aniline. The electron yield was recorded as a function of the rotational stage position of the KDP crystal (see sec 3.2) and a calibration matching this stage position with the obtained wavelength was established. The spectrometer used for this calibration has a spectral resolution of approx. 1.2 nm in the used range [109]. The laser bandwidth is approx. 6 cm^{-1}. In addition, the calibration of the spectra has been finely adjusted with a scaling factor to match the $6a^1$ ($6a^2$) transition in fig 5.4 (fig 5.5).

The x-axis in the spectrum in fig 5.4 is given as the photon energy relative to the origin as stated by previous experiments (34031 cm^{-1} [102]). The spectrum reveals three peaks. The first peak is the origin 0^0. Its centre mismatches the value measured by Qu et al. by 6 cm^{-1}. The second peak is the 15^1-transition, found at 374 cm^{-1} (Qu et al.: 386 cm^{-1} [102]). The third peak in the spectrum is ascribed to the $6a^1$-transition, found at 528 cm^{-1} (Qu et al.:

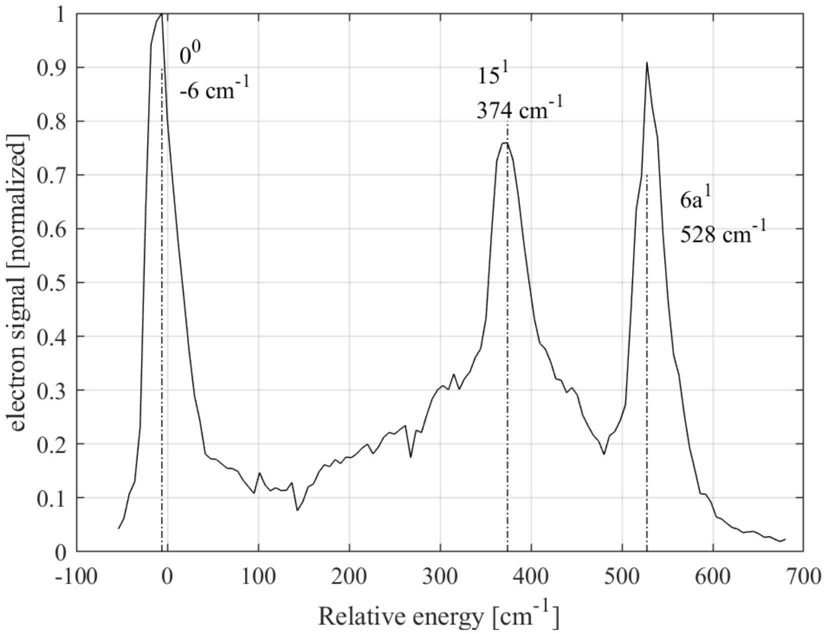

Figure 5.4: R2PI spectrum of gas phase aniline relative to the S_1-state (34031 cm^{-1}), dashed vertical lines give the centre of vibronic transitions. Transition locations according to [102]: 15^1 386 cm^{-1} $6a^1$ 527 cm^{-1}

527 cm^{-1}). This is a remarkable good agreement and exceeds the expectation given the spectrometer resolution.

Another R2PI-spectrum with a broader wavelength range is shown in fig 5.5. The photon energy is again given relative to the origin. The spectrum reveals nine peaks, seven of which could be assigned (see tab 5.2). The calibration matching the rotational stage position of the KDP crystal with the resulting wavelength was defective for the spectrum in fig 5.5. Therefore, the mismatch of the observed relative energies is bigger than in fig 5.4.

The ion R2PI spectrum presented by Qu et al. is shown in fig 5.6. They also used [1+1]-photoionization for their R2PI spectrum. However, the employed laser systems differ. Qu et al. used an Nd:YAG pumped dye laser with a bandwidth of 0.1 cm^{-1} and a pulse duration of 6-8 ns, while our laser setup results, as mentioned earlier, in a laser bandwidth of approx. 6 cm^{-1} and a pulse duration of 6 ps. The R2PI spectrum in fig 5.4 agrees well with the measurements of Qu et al., while the R2PI spectrum in fig 5.5 shows only a fair agreement.

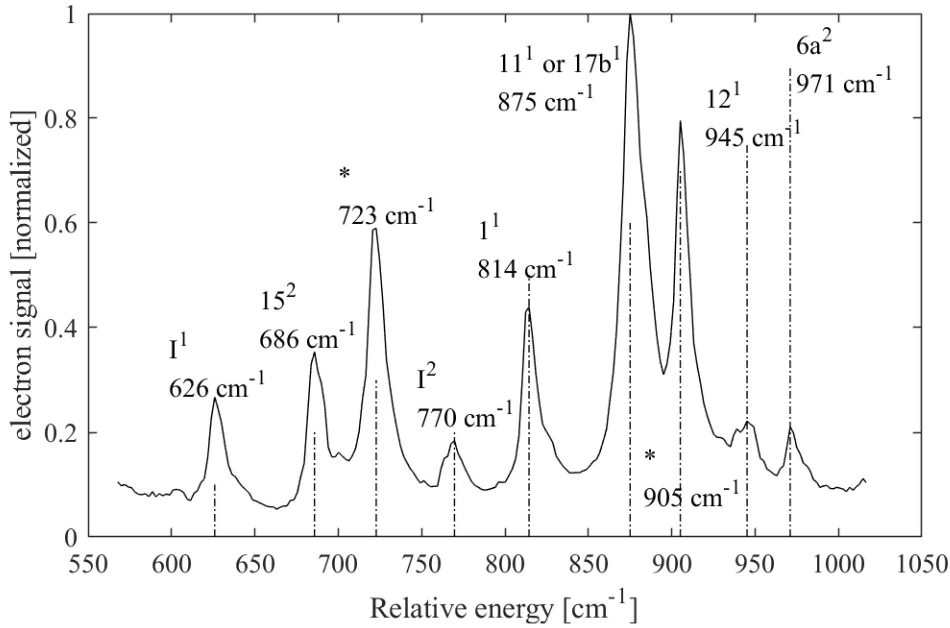

Figure 5.5: R2PI spectrum of gas phase aniline relative to the S_1-state (34031 cm^{-1}), with defective calibration. * marks transition locations that could not be assigned. Peak assignment see tab 5.2

Peak location [cm^{-1}]	Peak location [cm^{-1}], ref [102]	Assignment
626	595*	I^1
686	703	15^2
723		
770	760	I^2
814	798	1^1
875	799*	11^1 or 17b^1
905		
945	953	12^1
971	986**	6a^2

Table 5.2: Peak locations observed in fig 5.5 with the peak locations found by Qu et al. and their assignment. Values denoted with a * indicate values ref [102] only lists with calculated values. Values without a * are experimentally observed values. The value for the 6a^2 transition, marked **, is calculated from the frequency Qu et al. observed experimentally for the 6a^1.

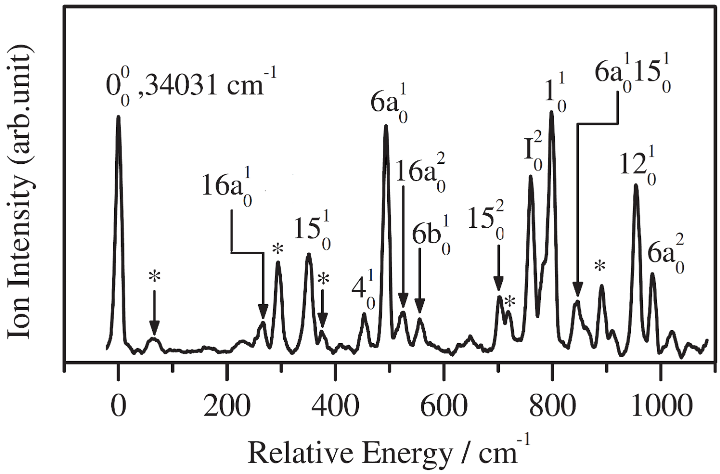

Figure 5.6: [1+1] R2PI, (*) indicate signal from contaminations. Figure adopted from [102]

5.3.2 0^0 vibrational mode

The two-dimensional velocity map images of electrons obtained via [1+1]-photoionization of aniline with the probe wavelength tuned to the origin transition, 293.85 nm (34031 cm^{-1}) are shown in fig 5.7. The different subfigures correspond to different alignment geometries, illustrated to the left of each electron velocity map image. The probe pulse intensity was close to the threshold of the power meter's sensitivity and was measured to be 0.06 $TW\,cm^{-2}$. However, it is very likely smaller than that. The probe pulse polarization is kept in plane with the detector, parallel to the z-axis, for all PADs, whereas the polarization state of the alignment pulse is varied. The images are normalized and displayed on the same scale, albeit the signal of the unaligned image has been doubled to enhance its visibility.

The electron velocity map image of randomly oriented aniline molecules, fig 5.7 a), exhibits three channels, labelled 1-3, each with an (almost) isotropic distribution. The channel with the lowest kinetic energy (1) is found at 0.40 eV, the second (2) at 0.55 eV and the last channel (3) at 0.75 eV. The second channel is ascribed to a combination of the $9a^1$- and the $8a^1$-transition. The third channel represents the origin 0^0. The first channel could not be assigned.

Upon aligning the molecules one-dimensionally with their MPA parallel to the z-axis, the photoelectron angular distribution becomes anisotropic, fig 5.7 b). The electrons are favourably ejected along the z-axis. Additionally to this angular confinement, new channels appear upon alignment. Besides aligning the molecule, alignment pulse photons also get absorbed, causing these new ionization channels, see also chapter 5.2. In fig 5.7 c), an elliptically (3:1) polarized pulse with its major axis parallel to z-axis was employed to align the molecules three-dimensionally. With this alignment geometry, the MPA is fixed parallel to z-axis, while the second most polarizable axis is fixed perpendicularly to it, parallel to the y-axis. This also leaves the third and least polarizable axis confined in space parallel to the x-axis. The PAD in this case does not reveal any striking difference to the PAD of the one-dimensionally aligned molecules. Figure 5.7 d) shows a special case of one-dimensional alignment. The circularly polarized alignment pulse fixes the benzene ring of aniline in space, thus confining the least polarizable axis parallel to the x-axis. Compared to fig 5.7 b) and c) the angular distribution is less confined. At a first glance, the confinement seems even more diminished in fig 5.7 e). This PAD is obtained from aniline molecules with their MPA fixed along the y-axis and their second most polarizable axis fixed in space parallel to the z-axis. Thus, the transition dipole moment of the S_1 state is parallel to the probe pulse polarization. The highest signal levels were obtained in this configuration. Accordingly, this electron velocity map image is the brightest. The angular confinement is de facto comparable to the one-dimensionally aligned case in fig 5.7 b). Since the transition dipole moment is oriented perpendicular to the probe pulse polarization with the molecules aligned one-dimensionally parallel to the z-axis, one would expect the signal to decrease compared to the randomly oriented aniline molecules. However, this is not the case due to the IR photons also being absorbed.

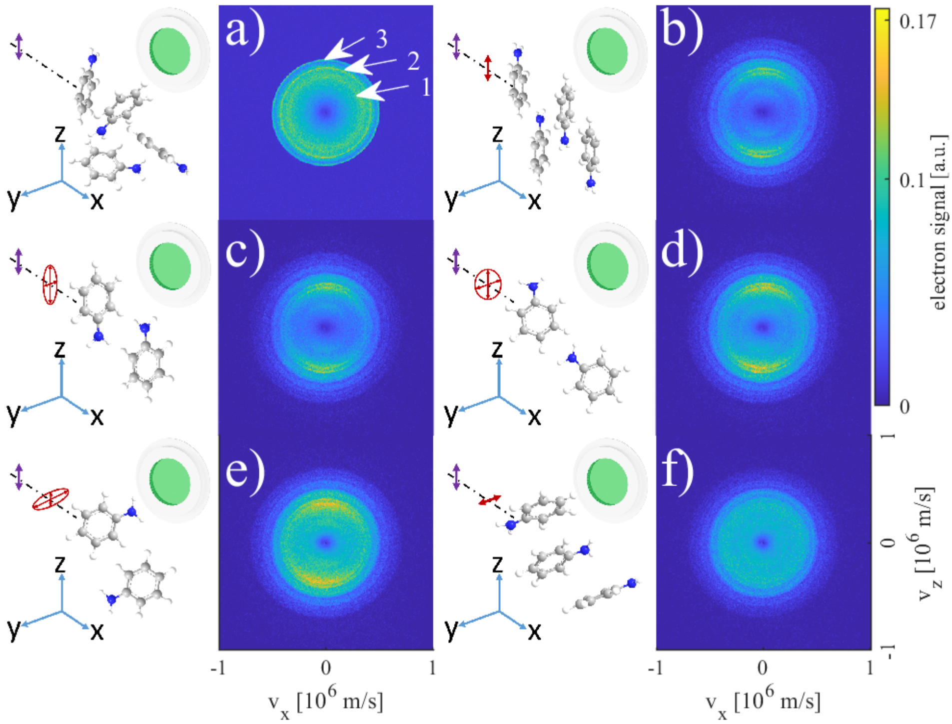

Figure 5.7: PADs from aniline molecules in gas phase 0^0 transition, probe wavelength 293.85 nm, I=0.06 TW cm^{-2}. a) unaligned, b) 1D aligned MPA $\parallel$ z-axis, c) 3D aligned MPA $\parallel$ z-axis, d) 1D aligned least polarizable axis $\parallel$ x-axis, e) 3D aligned MPA $\parallel$ y-axis, f) 1D aligned MPA $\parallel$ y-axis; 1-3 different channels

Each of the three channels marked in fig 5.7 a) has been analysed separately and their angular distributions have been determined. For a radial range, given by the extent of the channel, the signal of the image has been radially integrated. The figs 5.8-5.10 show the result of this integration. The lettering a)-f) follows the same scheme as in fig 5.7, while the centre image illustrates the radial range used for integration.

Figure 5.8 shows the angular distributions for the first channel, labelled 1 in fig 5.7. The angular distribution of unaligned molecules, fig 5.8 a) is isotropic. Aligning the molecules one-dimensionally with their MPA parallel to the z-axis, fig 5.8 b), reveals a two-fold structure with maxima at 0° and 180° in the angular distribution. When the molecule is three-dimensionally aligned with the MPA parallel to the z-axis, fig 5.8 c), the height of these maxima is increased. The two maxima are only insignificantly smaller for three-dimensionally aligned molecules with their MPA parallel to the y-axis, fig 5.8 e). Confining the least polarizable axis parallel to the x-axis, 5.8 d), also leads to a two-fold structure with maxima at 0° and 180°. However, they are smaller than in the case of one-dimensional alignment with the MPA parallel to the z-axis. With one-dimensional alignment confining the MPA parallel to the y-axis the distribution is almost isotropic with an insignificant amount of more electron signal at 90° and 270°.

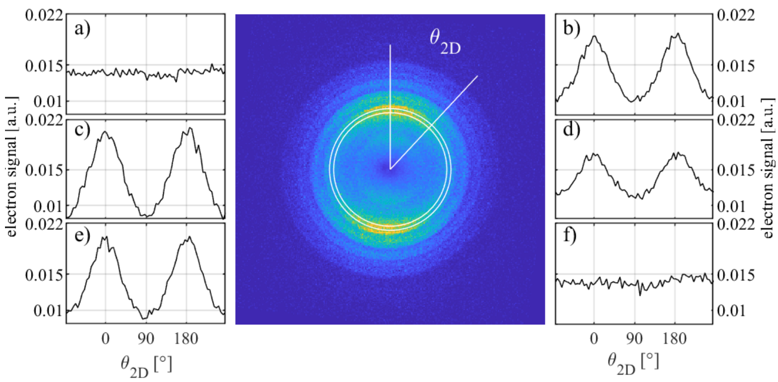

Figure 5.8: Angular distribution of the first channel (labelled 1 in fig 5.7), centre image: 1D ∥ aligned with radial range. The alignment geometries used in the different subfigures are the same as in fig 5.7, i.e. a) unaligned, b) 1D aligned MPA ∥ z-axis, c) 3D aligned MPA ∥ z-axis, d) 1D aligned least polarizable axis ∥ x-axis, e) 3D aligned MPA ∥ y-axis, f) 1D aligned MPA ∥ y-axis.

The second channel, fig 5.9, exhibits similar angular distributions as observed in the first channel fig 5.8. The angular distributions of the unaligned molecules fig 5.9 a) show an isotropic distribution. For the other alignment cases, b)-e), a preference for an ejection along the z-axis in the VMI image peaking at 0° and 180° can be observed. The most confined angular distribution is obtained, when the aniline molecules are aligned three-dimensionally with their MPA parallel to the z-axis fig 5.9 c). Upon aligning the molecules one-dimensionally with their MPA parallel to the y-axis, the angular distribution becomes isotropic again.

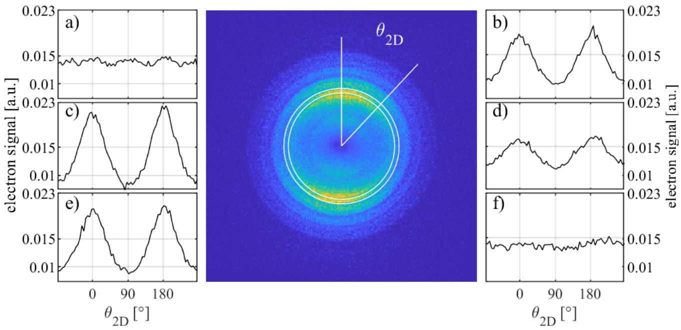

Figure 5.9: Angular distribution of the second channel (labelled 2 in fig 5.7) centre image: 1D ∥ aligned with radial range. The alignment geometries used in the different subfigures are the same as in fig 5.7, i.e. a) unaligned, b) 1D aligned MPA ∥ z-axis, c) 3D aligned MPA ∥ z-axis, d) 1D aligned least polarizable axis ∥ x-axis, e) 3D aligned MPA ∥ y-axis, f) 1D aligned MPA ∥ y-axis.

The angular distribution for the third channel, fig 5.10 differs from the previous angular distributions in the case of randomly oriented aniline molecules a) and the case of one-dimensionally along the y-axis aligned molecules f). When the molecules are unaligned a slight enhancement in 90° and 270° is observed. This is unexpected, because these ejection angles are perpendicular to the probe pulse polarization axis. In the case of molecules one-dimensionally along the y-axis aligned, fig 5.10 f), the angular distribution is not isotropic and exhibits a small enhancement at 0° and 180°.

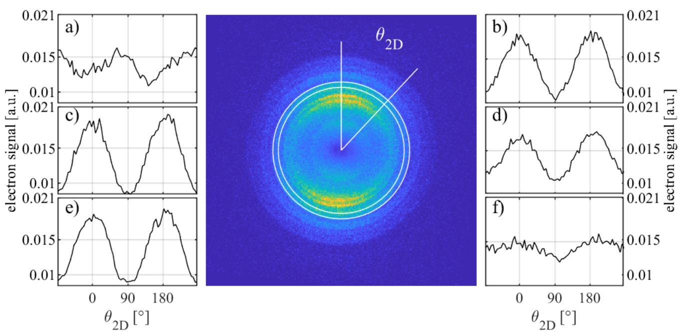

Figure 5.10: Angular distribution of the third channel (labelled 3 in fig 5.7) centre image: 1D ∥ aligned with radial range. The alignment geometries used in the different subfigures are the same as in fig 5.7, i.e. a) unaligned, b) 1D aligned MPA ∥ z-axis, c) 3D aligned MPA ∥ z-axis, d) 1D aligned least polarizable axis ∥ x-axis, e) 3D aligned MPA ∥ y-axis, f) 1D aligned MPA ∥ y-axis.

The PADs obtained from unaligned and the one-dimensionally along the z-axis aligned aniline molecules have been Abel inverted and the kinetic energy distribution has been extracted. For an easier comparison to the literature, the photoelectron kinetic energy spectrum of the unaligned PAD was converted to ion internal energy, fig 5.11. The spectrum reveals three peaks. The first peak is readily assigned to the origin, the 0^0-transition. The second peak is a convolution of two peaks. Through fitting, their respective position was determined to be found at 1134 cm^{-1} and 1688 cm^{-1}. They can be assigned to the $9a^1$- and $8a^1$-transition, which is in good agreement with the measurements of Qu et al. (1188 cm^{-1} and 1592 cm^{-1} [102]). The VMI resolution was measured to be at 9% (155 meV) for photoelectron kinetic energies about 2 eV. The discrepancy in this case, 94 cm^{-1}, corresponding to 12 meV is therefore below the VMI resolution.

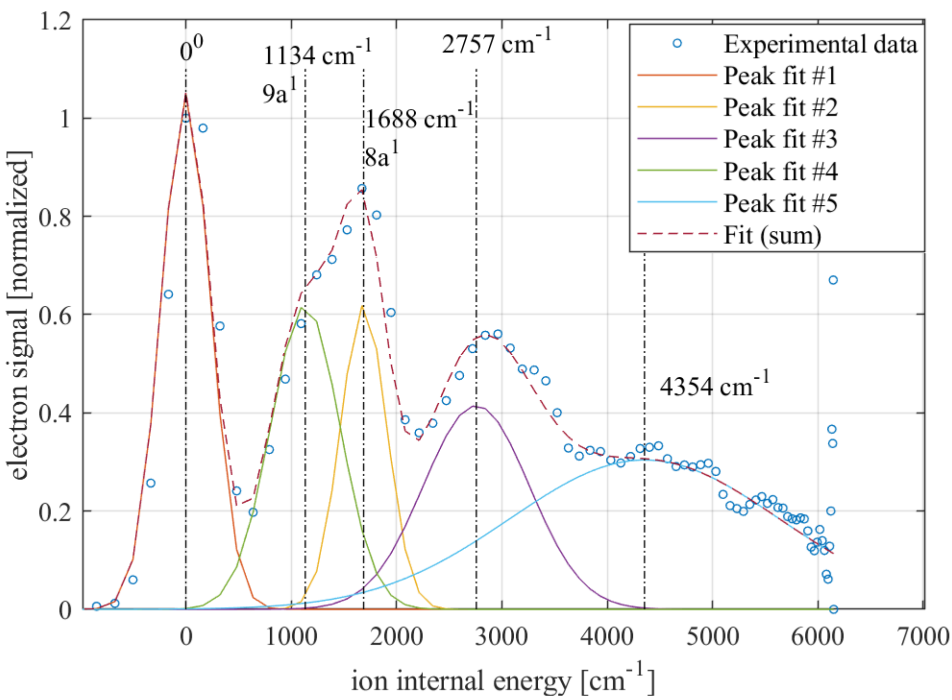

Figure 5.11: [1+1]-photoionization photoelectron spectrum in ion internal energy of unaligned aniline molecules, 0^0 transition, obtained through Abel inversion. Probe wavelength 293.85 nm. Assigned peak locations according to [102]: $8a^1$ 1594 cm^{-1}, $9a^1$ 1188 cm^{-1}

Figure 5.12 shows the energy distribution obtained through Abel inversion from the PAD of one-dimensionally aligned molecules with their most polarizable axis parallel to the plane of the detector. Due to the absorption of parts of the alignment pulse, this photoelectron spectrum exhibits more channels. The various peak locations are indicated as dashdotted lines in fig 5.12. They are summarized and assigned in tab 5.3. Comparing the ionization channels in fig 5.11 and the ionization channels in fig 5.12, the difference in the total number of peaks is evident (see also fig 5.13). Besides the new ionization channels due to a populated S_2 and S_3, there are also other vibrational modes enhanced or missing. The $9a^1$ vibration is supposedly missing in fig 5.12, while the 1^1 or I^1 vibration channel appears.

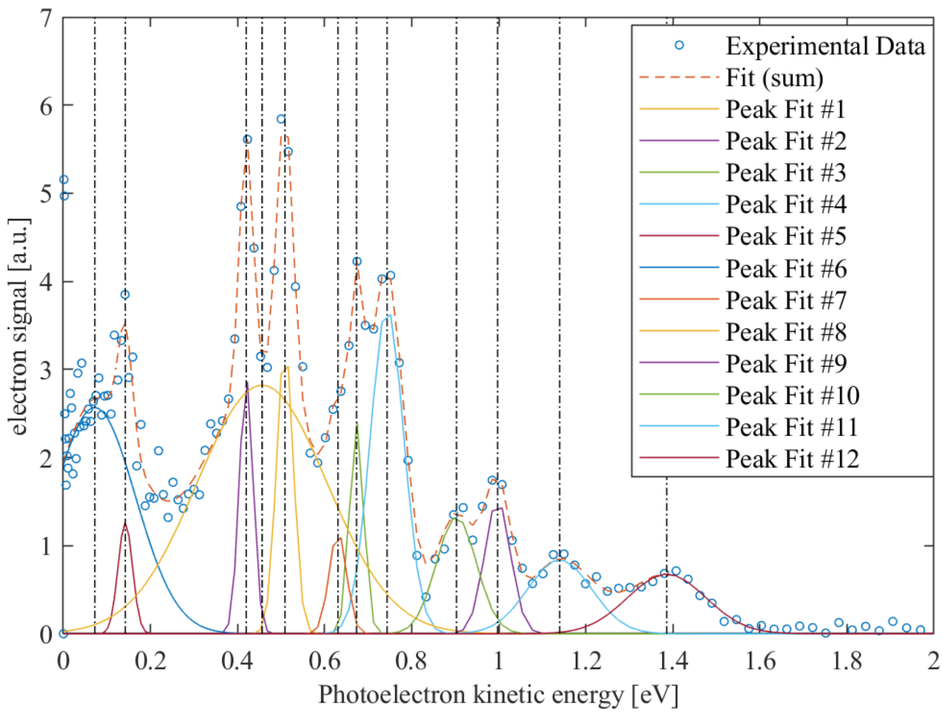

Figure 5.12: [1+1]-photoionization photoelectron spectrum of aligned aniline molecules, 0^0 transition, probe wavelength 293.85 nm, 0.06 TW cm^{-2}. The peaks are assigned in tab 5.3.

kE [eV]	Assignment
0.07	
0.14	
0.42	
0.46	
0.51	$8a^1$ and 9a (?)
0.63	I or 1 (?)
0.67	16a (?)
0.74	0^0
0.90	via S_2, $8a^1$
1.00	via S_2, I or 1 (?)
1.14	via S_2, 0^0
1.39	via S_3, 0^0 (?)

Table 5.3: Peak location in photoelectron kinetic energy and assignment

Figure 5.13 shows the photoelectron kinetic energy distributions of aligned (red) and unaligned (blue). Both distributions have been normalized to their respective maximum. With the unaligned distirbution the maximum intensity is located in the origin channel, while the maximum intensity in the one-dimensionally aligned distribution is found in the $8a^1$ channel. Furthermore the channels are slightly red and blue shifted in the aligned distribution. The $8a^1$ channel is found at at 0.55 (0.51) eV in the unaligned (aligned) photoelectron kinetic energy distribution and the origin at 0.76 (0.74) eV. For these three channels, the anisotropy parameters have been extracted as a weighted average (hatched areas fig 5.13). The areas have been chosen such that they overlap as much as possible for the aligned and unaligned distribution, albeit the shift. For the origin channel only the outer edge of the peak has been evaluated, c2 in fig 5.13, to minimize the influence of the 1^1 channel. As the $8a^1$ and $9a^1$ channel overlap significantly in the unaligned distribution, the whole area was chosen, b1) in fig 5.13, although the influence of the $9a^1$ is potentially missing in the aligned distribution.

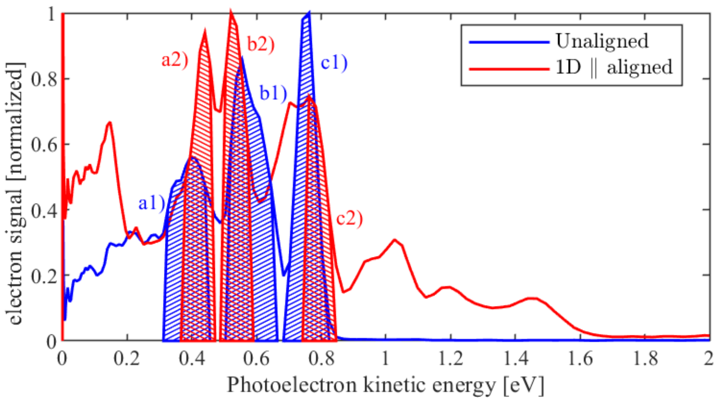

Figure 5.13: [1+1]-photoionization photoelectron spectrum of aligned and unaligned aniline molecules, 0^0 transition; hatched areas used for β-calculation

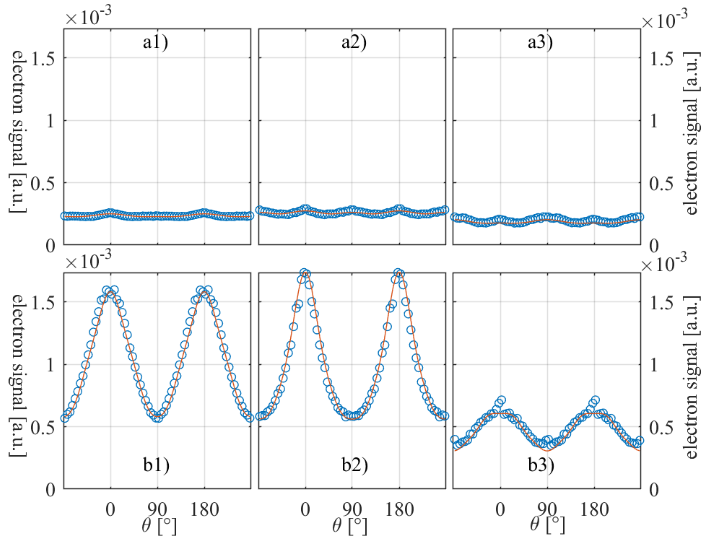

Figure 5.14: Angular distributions from the 0^0 transition of aniline, raw Abel inverted data (circles) and fit (solid line); for the three channels: first channel 1), second channel 2), and third channel 3). The upper row a) shows the distribution from unaligned molecules, the lower row b) the distribution from one-dimensionally aligned molecules (MPA ∥ z-axis)

Qu et al. observed for the 0^0-transition using [1+1]-photoionization (293.85 nm) a β_2 of -0.1305 and β_4 -0.1938 [102]. They did not align the molecules. While our measurement for the unaligned molecules agrees well for the β_2, -0.1158, β_4, 0.0517 differs significantly. The angular anisotropy with pronounced features at 0° and 180° upon alignment is clearly visible, fig 5.14 b1)-b3). The less energetic channels of the unaligned molecules, fig 5.14 a1) and a2), show an isotropic distribution. The anisotropy is most pronounced in the second channel of the aligned aniline molecules, fig 5.14 b2).

5.3.3 Alignment intensity study

This chapter is based on the publication in preparation, see [110]. GAMESS and ePolyScat calculations were performed by Paul Hockett, who also wrote the post process programme to interpret them. James Thompsen performed the calculations to generate the voxel matrices and their projection and extracted the beta values there-from. I wrote the code to turn, weight and average the voxel matrices and extracted the experimental anisotropy parameters. Dhirendra Singh and I conducted the experiment together.

When the intensity of the alignment pulse is varied, the achieved degree of alignment varies accordingly, see fig 5.2. Thus, the molecular frame coordinate system and the laboratory frame coordinate system coincide to a different degree. The less confined the alignment, the more averaging effects blur the MFPAD, see also ref [48].

An alignment intensity study for the 0^0-transition for the special case of one-dimensional alignment has been performed with supporting theoretical calculations using ePolyScat, see refs [111, 112] for details, and ref [113] for the calculation results. The ePolyScat calculation results have been post-processed with ePSproc, see ref [114].

With ePolyScat the radial dipole matrix elements have been calculated starting from the S_1-state and using the cation state as the final state. In comparison with the experiment, this corresponds to neglecting the absorption process of the first UV photon and other ionization channels, especially due to absorbing an IR photon. In a next step, ePSproc was used to calculate the MFPAD also considering the probe pulse polarization. Further calculations take the non-perfect alignment into account and simulate possible electron velocity map images. The following section is dedicated to the results of these calculations and provides a comparison to the experimental results.

Figure 5.15 shows isosurfaces of MFPADs calculated with ePSproc for chosen photoelectron kinetic energies, a) 0.1 b) 1.1 c) 2.1, ... f) 5.1 eV. The attributed energies are estimated to be accurate within 1 eV. It is dutifully noted that the calculated MFPADs are not on the same scale to enhance their visibility. The MFPADs are calculated for perfectly oriented molecules, see fig 5.16 a1) for a geometry reference. The lobes in each subfigure are showing directions of preferred of emission, while the nodes are areas of suppressed emission. The MFPADs also feature shape resonances, i.e. the photoelectron scattering on the molecule's potential. All six MFPADs exhibit twelve lobes. However, their distribution and respective sizes vary. The MFPAD with a photoelectron kinetic energy of 0.1 eV, figure 5.15 a), exhibits four lobes that are almost in the xy-plane, each lobe containing an angle of 45° with the x- or the y-axis. Eight further lobes are also following the 45°-distribution with the x- or the y-axis, but are stretching in the positive or negative direction of the the z-axis. The lobes in the positive z-direction, i.e. the direction of the amino group (see also fig 5.16 a1) are slightly larger than the other eight lobes. Figure 5.15 b) shows the MFPAD of photoelectrons with a kinetic energy of 1.1 eV. The four lobes that are almost in the xy-plane are most pronounced. With a photoelectron kinetic energy of 2.1 eV, fig 5.15 c), the four lobes in the positive z-direction are as pronounced as the four lobes that are found almost in the xy-plane. The least emission is found in the four lobes in the negative z-direction. With increasing energy, 3.1 eV, fig 5.15 d), the four lobes in the positive z-direction are more pronounced than the ones almost in the xy-plane. Figure 5.15 e) shows the MFPAD calculated for a photoelectron kinetic energy of 4.1 eV. The four lobes pointing in the positive z-direction are most pronounced, while the four lobes almost in the xy-plane decrease compared to fig 5.15 d). The MFPAD in fig 5.15 f), 5.1 eV varies only slightly from the MFPAD in fig 5.15 e). The lobes almost in the xy-plane decrease further, while the lobes in the positive z-direction are most pronounced.

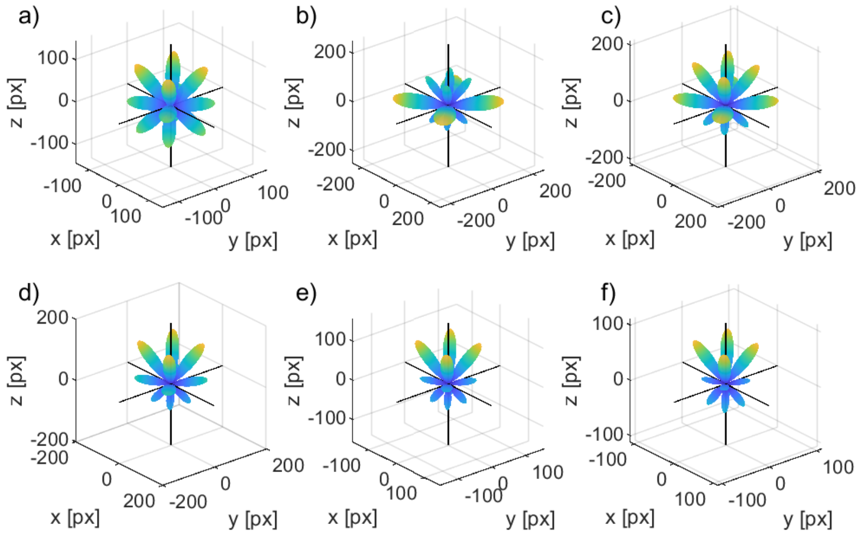

Figure 5.15: Calculated three-dimensional MFPADs with increasing photoelectron kinetic energy $[0.1, 1.1, \ldots, 5.1]$ eV. Figure also used in [110]

The MFPADs in fig 5.15 are considering a probe pulse parallel to the z-axis. However, the aniline molecules in the experiment are not perfectly aligned. Thus, the MPA can include an angle with the polarization direction of the probe pulse. Figure 5.16 a1) shows the geometry with the laser polarization parallel to the MPA. In fig 5.16 b1) the polarization direction of the probe pulse is at an angle to the MPA. Both figures are drawn in a molecular frame coordinate system. Thus, the MPA is fixed in space to the z-axis, while the polarization vector of the probe pulse varies with respect to it. Figure 5.16a2) shows the MFPAD resulting from a parallel orientation with an electron kinetic energy 5.1 eV, reproducing the MFPAD from fig 5.15 f). When the probe pulse polarization does not coincide with the MPA, the lobes differ, see fig 5.16 b2). Two of the four lobes in the positive z-direction increase, while the other two decrease in size. Furthermore, two of the lobes in the negative z-direction get enhanced while the other two decrease. This leads to different electron velocity map images, fig 5.16 a3) and b3). The projection accessible in the experiment is the one in the xz-plane. In fig 5.16 a3) the four most pronounced lobes of fig 5.16 a2) give the most signal, visible as two yellow spots (marked with a white arrow). As two lobes in the positive z-direction in fig 5.16 b2) are more pronounced than the other two, the resulting electron velocity map image, fig 5.16 b3) also shows one brighter and one darker spot (marked with a white arrow) compared to fig 5.16 a3).

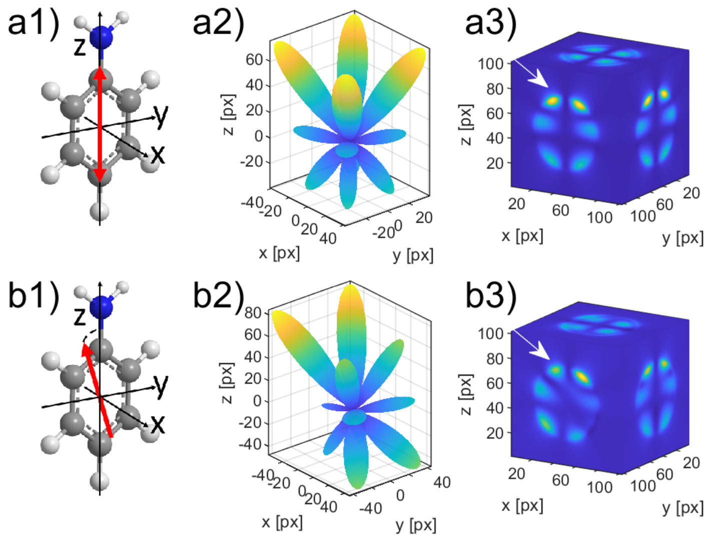

Figure 5.16: a1), b1) Geometry between the MPA (z-axis) and the probe pulse polarization (red arrow) for ϑ=0° and ϑ=22.5°, a2), b2) resulting MFPADs, a3), b3) projections of the respective three-dimensional velocity distributions

Figures 5.16 a3) and b3) show the electron velocity map images for only two distinctive angles. In practice, MPFPADs for a series of orientations of the MPA respective to the polarization of the probe laser have been calculated. The angle between the MPA and polarization axis is given as a subset of Euler angles, $(\vartheta_{\hat{n}}, \varphi_{\hat{n}})$. The angles have been varied in 5° increments in an interval of [0° 90°]. This represents 1/8th of a sphere.

It shall be highlighted, that the electron velocity map images in 5.16 a3) and b3) are given in the molecular frame coordinate system, i.e. the polarization of the probe pulse is varied with respect to the MPA of the molecules. The MPA of the molecule is parallel to the z-axis. In the laboratory frame, the polarization of the probe pulse is constant, while the MPA of the molecule is angled with respect to it. In order to convert the resulting electron velocity map image to the laboratory frame, the three-dimensional electron velocity distribution (a voxel matrix) used to generate the projections [e.g. fig 5.16 a3) and b3)] have been turned, such that the probe pulse polarization matches for each.

In order to obtain the other 7/8th of a sphere, the three-dimensional electron velocity distributions have been symmetrized. Each entry in the three-dimensional velocity distribution q_{ijk} has been summed with its seven mirror entries in the other seven quadrants:

$$\begin{aligned} q_{i,j,k} = q_{i,j,k} + q_{e-i,j,k} + q_{i,e-j,k} + q_{i,j,e-k} \\ +q_{e-i,e-j,k} + q_{e-i,j,e-k} + q_{i,e-j,e-k} + q_{e-i,e-j,e-k} \end{aligned} \tag{5.3}$$

With e being the size of the odd-sized matrix plus one. This step accounts for the molecules being oriented with the amino group in the positive as well as in the negative z-direction, as well as being turned by 180°.

In a next step, each three-dimensional velocity matrix has been averaged around the laboratory frame z-axis, since the molecules can be oriented in either direction around the z-axis. Within these two steps, the rotation of the molecule around itself is neglected to some extend. While the chosen angles $(\vartheta_{\hat{n}}, \varphi_{\hat{n}})$ all provide that the molecules include a different angle with the laboratory frame z-axis, they are nevertheless specific. However, the considered time frame is only the absorption of the second UV photon. The rotation of the molecule in the time between the absorption of the first and the second photon can therefore be neglected. Furthermore, if the three-dimensional velocity matrix was averaged before it was rotated, so that the polarization vector matches the laboratory frame z-axis, the polarization vector would be averaged as well and the matrix could therefore not be rotated reliably into the laboratory frame.

For different degrees of alignment $\langle \cos^2 \theta \rangle$, the different three-dimensional electron velocity distributions have been projected onto the xz-plane. Each of the two-dimensional electron velocity distributions has a different probability of contributing to the final summed two-dimensional electron velocity distribution. Thus, each of the resulting distributions have been weighted according to the formula introduced by Reid in [48], see eq 5.4 and summed accordingly.

$$P(\theta) = n_\sigma e^{\left(\frac{-\sin^2 \theta}{2\sigma^2}\right)} \tag{5.4}$$

with:

$$n_\sigma = \frac{1}{\int_0^\Pi e^{\left(\frac{-\sin^2 \theta}{2\sigma^2}\right)} \sin \theta d\theta} \tag{5.5}$$

and as a rule of thumb:

$$\lim_{\sigma^2 \to 0} \sigma^2 = 1 - \langle \cos^2 \theta \rangle \tag{5.6}$$

For each of the six photoelectron kinetic energies, six different degrees of alignment [0.5, 0.6 ... 1.0] have been simulated. As the calculation is computatively demanding, the randomly oriented distribution $\langle \cos^2 \theta \rangle$ =0.33 has been neglected. The anisotropy parameters $b_L{}^{LF}$ have been extracted from each. The index L describes the angular momenta. LF indicates that they are extracted from the laboratory frame distribution, i.e. the simulated electron velocity map image. The resulting distribution is shown in fig 5.17. Focussing on the $b_2{}^{LF}$-value (blue), different tendencies can be seen. For a photoelectron kinetic energy of 0.1 eV, fig 5.17 a), the value hardly varies from zero, even for high degrees of alignment. In fig 5.17 b), photoelectron kinetic energy 1.1 eV, the $b_2{}^{LF}$ -value decreases with increasing degree of alignment. This is also the case, though milder, for a photoelectron kinetic energy of 2.1 eV, fig 5.17 c). For a photoelectron kinetic energy of 3.1 eV, fig 5.17 d), the trend inverts. With increasing degree of alignment, the $b_2{}^{LF}$ -value also increases. The slope increases for 4.1 eV and 5.1 eV fig 5.17 e) and f).

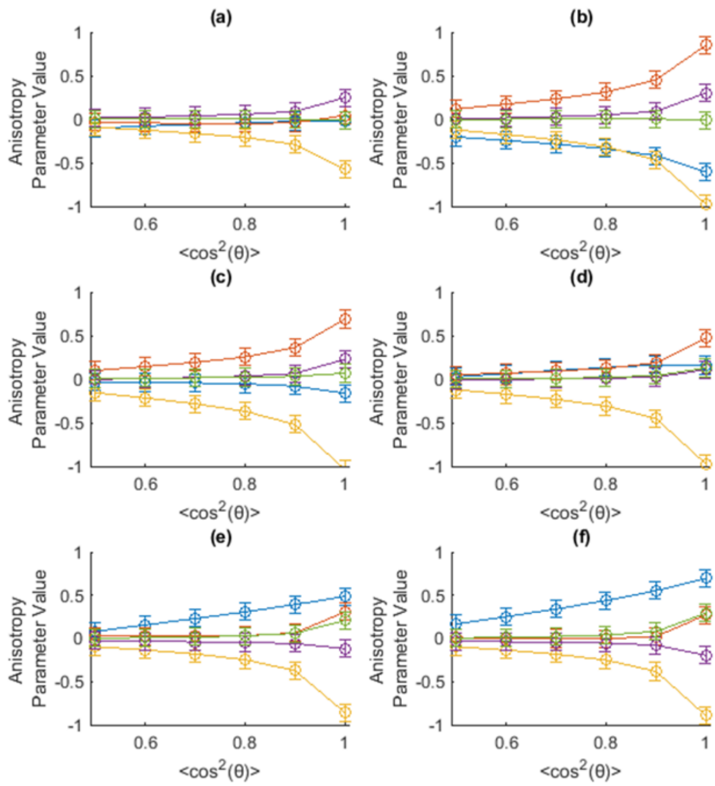

Figure 5.17: Simulation of the anisotropy parameters, $b_L{}^{LF}$, for the projected simulated LFPADs for a range of photoelectron kinetic energies, Ekin. a) 0.1 eV b) 1.1 eV c) 2.1 eV d) 3.1 eV e) 4.1 eV f) 5.1 eV. The different colours indicate the angular momenta L = 2 (blue), 4 (orange) , 6 (yellow), 8 (purple) and 10 (green). Figure also used in [110]

The experimental distribution of anisotropy parameters in dependence to the degree of alignment is shown in fig 5.18. The respective degree of alignment has been estimated using the conservative estimate, eq 5.1. The distribution also shows an increasing β_2-value with an increasing degree of alignment. Thus, it is likely, that the original MFPAD leading to the data presented for the origin channel in 5.3.2 looked like the MFPAD calculated with a photoelectron kinetic energy of 4.1 eV or 5.1 eV, albeit the measured photoelectron kinetic energy was 0.72 eV.

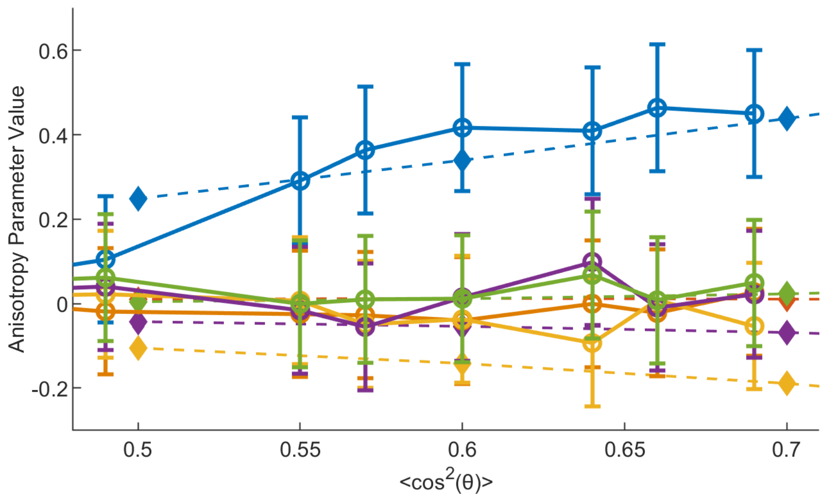

Figure 5.18: Anisotropy parameters, Dashed lines and diamonds: values from the fits to experimental data as a function of the degree of alignment; Solid lines and the circles: values from the projected calculated LFPADs at 4.1 eV as a function of $\langle\cos^2\theta\rangle$. The different colours indicate the angular momenta L = 2 (blue), 4 (orange) , 6 (yellow), 8 (purple) and 10 (green). Figure also used in [110]

5.3.4 1^1 vibrational mode

The 1 vibrational motion of aniline is an in-plane motion in the form of a ring breathing of the benzene ring. Figure 5.19 shows the PADs obtained from a [1+1]-photoionization via the 1^1 vibrational mode of the first electronically excited state, S_1, 287.1 nm (34831 cm^{-1}, 4.32 eV, see also fig 5.5) with an intensity of 0.08 TW cm^{-2}. The molecules have been aligned with an intensity of 0.9 TW cm^{-2}. The labels a)-f) follow the same scheme to label the geometries as fig 5.7. Furthermore the signal in fig 5.19 is also doubled to enhance its visibility. The PADs look rather similar to the PADs in fig 5.7. The unaligned distribution exhibits three channels, fig 5.19 a). As for the 0^0-vibrational mode, additional channels appear upon alignment, b)-f). Subfigures a) and f) seem isotropic, while fig 5.19 b)-e) exhibit an angular confinement.

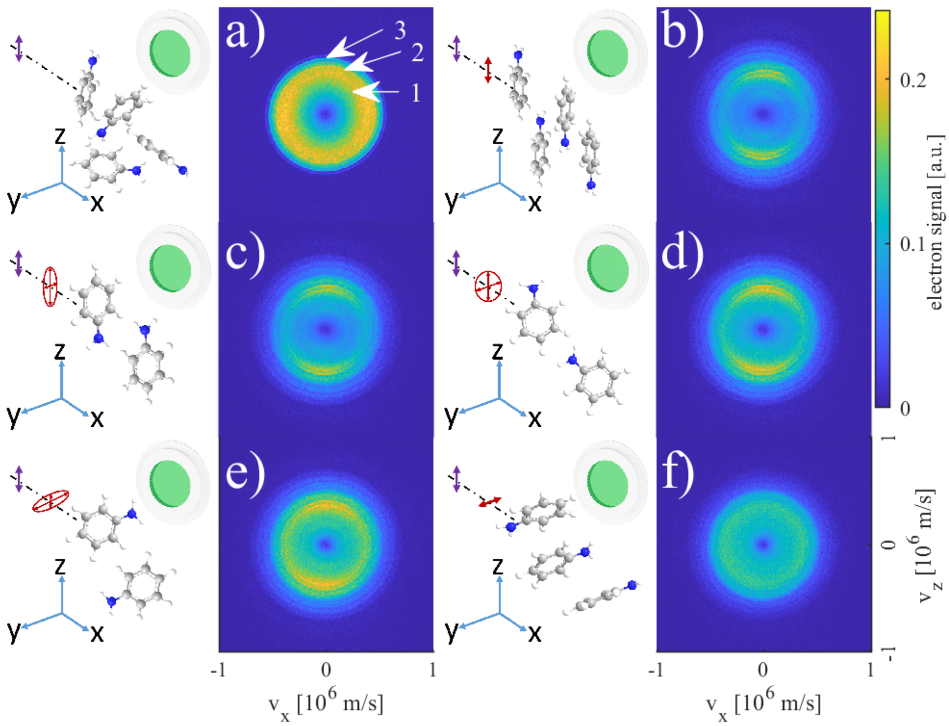

Figure 5.19: PADs from aniline molecules in gas phase 1^1 transition, probe wavelength 287.1 nm I=0.08 TW cm^{-2}. a) unaligned, b) 1D aligned MPA ∥ z-axis, c) 3D aligned MPA ∥ z-axis, d) 1D aligned least polarizable axis ∥ x-axis, e) 3D aligned MPA ∥ y-axis, f) 1D aligned MPA ∥ y-axis; 1-3 different channels

Figure 5.20 shows the angular distributions for the first channel, labelled 1 in fig 5.19. The angular distribution of unaligned molecules, fig 5.20 a) has slight maxima at 90° and 270°, perpendicular to the probe polarization. Upon aligning the molecules one-dimensionally with their MPA parallel to the z-axis, fig 5.20 b) the angular distribution shows a two-fold structure with maxima at 0° and 180°. These maxima increase, when the molecule is three-dimensonally aligned with the MPA parallel to the z-axis, fig 5.20 c). They are only marginally smaller for three-dimensionally aligned molecules with their MPA parallel to the y-axis, fig 5.20 e). Confining the least polarizable axis parallel to the x-axis, 5.20 d), also leads to a two-fold structure with maxima at 0° and 180°. However, they are smaller than in the case of one-dimensional alignment with the MPA parallel to the z-axis. With one-dimensional alignment confining the MPA parallel to the y-axis the distribution is almost isotropic with an insignificant amount of more electron signal at 90° and 270°.

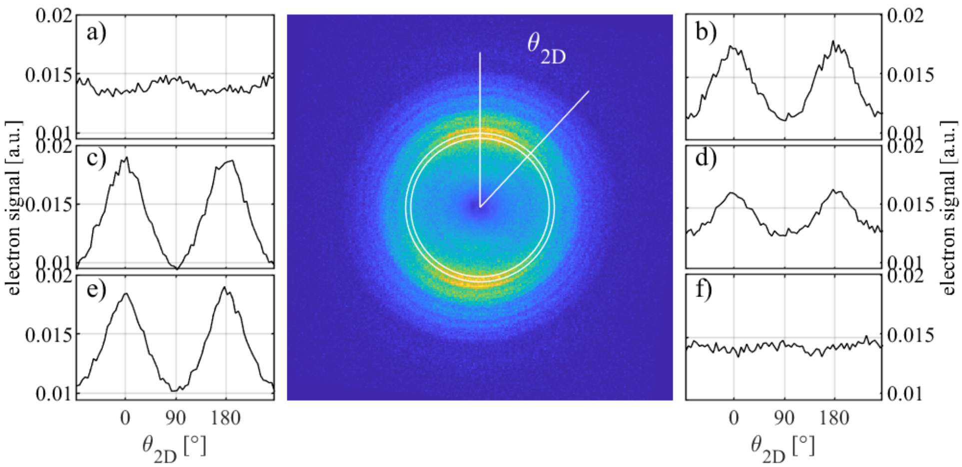

Figure 5.20: Angular distributions of the first channel (labelled 1 in fig 5.19) centre image: 1D ∥ aligned with radial range. The alignment geometries used in the different subfigures are the same as in fig 5.19, i.e. a) unaligned, b) 1D aligned MPA ∥ z-axis, c) 3D aligned MPA ∥ z-axis, d) 1D aligned least polarizable axis ∥ x-axis, e) 3D aligned MPA ∥ y-axis, f) 1D aligned MPA ∥ y-axis.

The angular distribution of the second channel, labelled 2 in fig 5.19, is shown in fig 5.21. As in fig 5.20 a), the angular distribution of unaligned molecules, fig 5.21 a), exhibits faint maxima at 90° and 270°. However, they are more pronounced as in fig 5.20 a). Aligning the molecules one-dimensionally with their MPA parallel to the z-axis, fig 5.21 b), reveals a two-fold structure with peaks at 0° and 180°. These maxima increase upon three-dimensional alignment with the MPA parallel to the z-axis, fig 5.21 c). They are slightly diminished when the molecules are aligned three-dimensionally with their MPA parallel to the y-axis, fig 5.21 e). When the least polarizable axis is confined parallel to the x-axis, fig 5.20 d), the angular distribution also shows a two-fold structure with maxima at 0° and 180°. However, they are also smaller than in the case of one-dimensional alignment with the MPA parallel to the z-axis, as it was the case for the first channel. A difference to the first channel can be observed in fig 5.21 f). The angular distribution is isotropic.

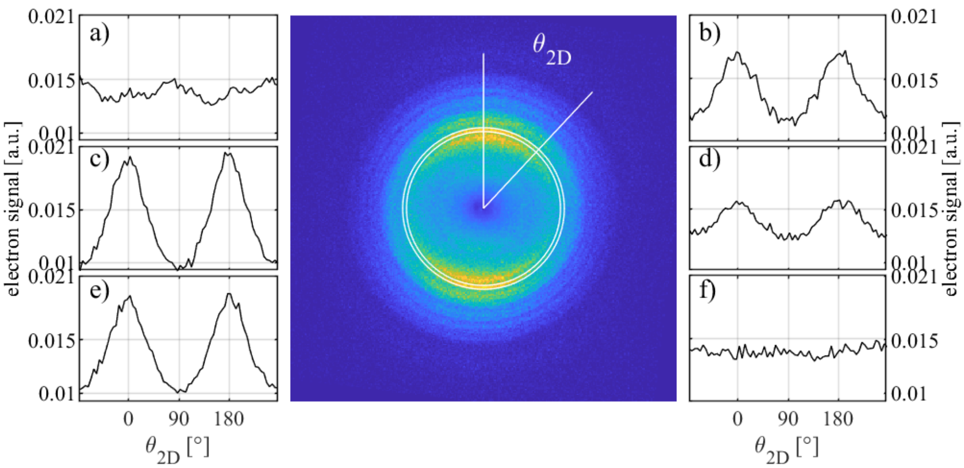

Figure 5.21: Angular distributions of the second channel (labelled 2 in fig 5.19) centre image: 1D ∥ aligned with radial range. The alignment geometries used in the different subfigures are the same as in fig 5.19, i.e. a) unaligned, b) 1D aligned MPA ∥ z-axis, c) 3D aligned MPA ∥ z-axis, d) 1D aligned least polarizable axis ∥ x-axis, e) 3D aligned MPA ∥ y-axis, f) 1D aligned MPA ∥ y-axis.

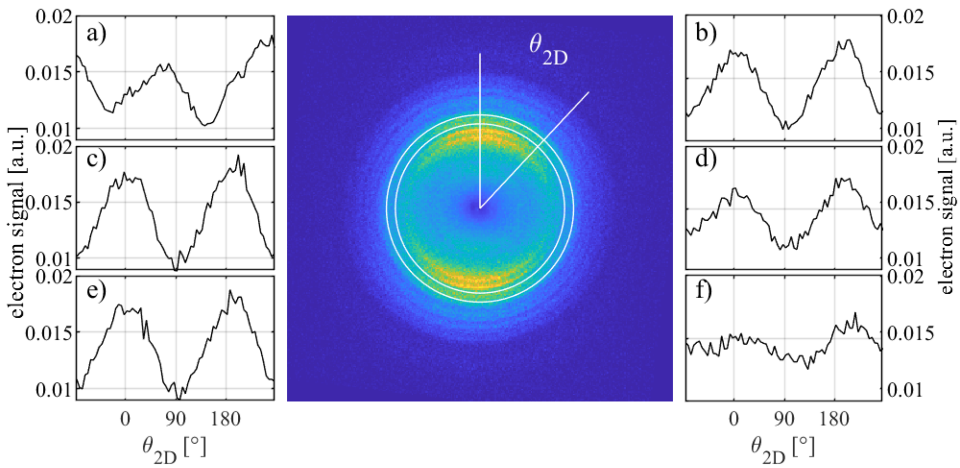

Figure 5.22: Angular distributions of the third channel (labelled 3 in fig 5.19) centre image: 1D ∥ aligned with radial range. The alignment geometries used in the different subfigures are the same as in fig 5.19, i.e. a) unaligned, b) 1D aligned MPA ∥ z-axis, c) 3D aligned MPA ∥ z-axis, d) 1D aligned least polarizable axis ∥ x-axis, e) 3D aligned MPA ∥ y-axis, f) 1D aligned MPA ∥ y-axis.

Figure 5.22 shows the angular distribution of the third channel, labelled 3 in fig 5.19. The angular distribution of the unaligned molecules, fig 5.22 a), shows a remarkable two-fold structure perpendicular to the probe pulse polarization. The maxima can be found at 90° and 270°. Aligning the molecules one-dimensionally with their MPA parallel to the z-axis, fig 5.22 b), reverses the effect. The maxima are now found at 0° and 180°. These maxima get slightly enhanced upon aligning the molecules three-dimensionally with their MPA parallel to the z-axis, fig 5.22 c). Confining the least polarizable axis to the x-axis, fig 5.22 d), leaves the maxima decreased compared to fig 5.22 a). When the molecules are aligned three-dimensionally with their MPA parallel to the y-axis, fig 5.22 e), the maxima increase again and the height of the peaks is the same as for three-dimensional alignment with the MPA parallel to the z-axis. Aligning the molecules one-dimensionally with their MPA parallel to the y-axis gives only slight maxima at 0° and 180°.

The electron velocity map image of the unaligned aniline molecules, fig 5.19 a), has been Abel inverted and the photoelectron kinetic energy distribution has been extracted. In order to facilitate the comparison to the literature, the spectrum has been converted to ion internal energy, see fig 5.23. The three channels visible in fig 5.19 a) can readily be seen as three dominant peaks. The first peak is assigned to the origin, i.e. the cation is left in the vibrational ground state after ionization. The second peak, centred at 821 cm^{-1}, can be assigned to the 1^1 vibrational mode of the cation (location according to Qu et al. 814 cm^{-1} [102]). The third peak is ascribed to the 1^2 vibrational mode and is centred at 1650 cm^{-1} (Qu et al. 1621 cm^{-1} [102]). The measurement is therefore in good agreement with the literature.

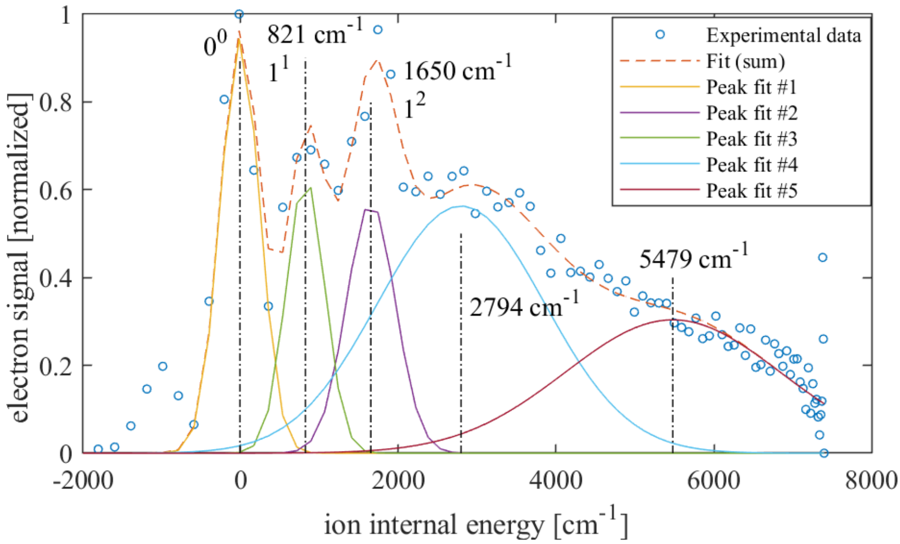

Figure 5.23: [1+1]-Photoionization photoelectron spectrum of unaligned aniline molecules 1^1 transition, probe wavelength 287.1 nm, I=0.08 TW cm^{-2}. Assigned peak locations according to [102]: 1^1 814 cm^{-1}, 1^2 1621 cm^{-1}

The photoelectron kinetic energy distribution obtained via Abel inversion of the one-dimensionally aligned molecules with their MPA parallel to the z-axis, is shown in fig 5.24. As seen for 0^0-transition, see section 5.3.2, new peaks appear upon aligning the molecules. Furthermore, the peak locations shift. A tentative assignment can be found in tab 5.4.

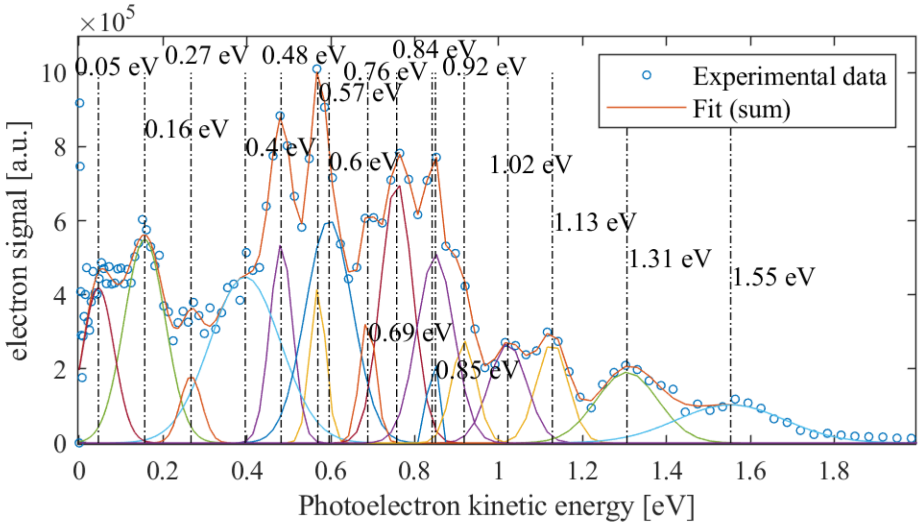

Figure 5.24: [1+1]-photoelectron kinetic energy distribution from 1D aligned aniline molecules (MPA ∥ z-axis) in gas phase 1^1 transition. Probe wavelength 287.1 nm, I=0.08 TW cm^{-2}. The peaks are assigned in tab 5.4.

eKE [eV]	Assignment
0.05	
0.16	
0.27	
0.40	
0.48	1^2 (?)
0.57	1^1 (?)
0.60	
0.69	$8a^1$ (?)
0.76	$9a^1$ (?)
0.84	I or 6a
0.92	0^0
1.02	via S2 10b or 16 a (?)
1.13	S_2 0^0
1.31	
1.55	S_3 0^0 (?)

Table 5.4: Peak location in photoelectron kinetic energy and assignment

The angular distributions of the Abel inverted images for the three most prominent channels in fig 5.19 a) have been extracted, see fig 5.25. The upper row a), shows the angular distributions of the unaligned molecules, the lower row b), shows the angular distributions of the one-dimensionally aligned molecules with the MPA parallel to the z-axis. For the unaligned distribution, all three channels, fig 5.25 a1)-a3), show an isotropic distribution. The third channel exhibits an insignificant amount of excess signal at 90° and 270°. Upon aligning the molecules one-dimensionally with their MPA parallel to the z-axis, fig 5.25 b1)-b3), the angular distributions exhibit a two-fold structure with maxima at 0° and 180°. This anisotropy is most pronounced for the second channel, tentatively assigned to the 1^1 channel.

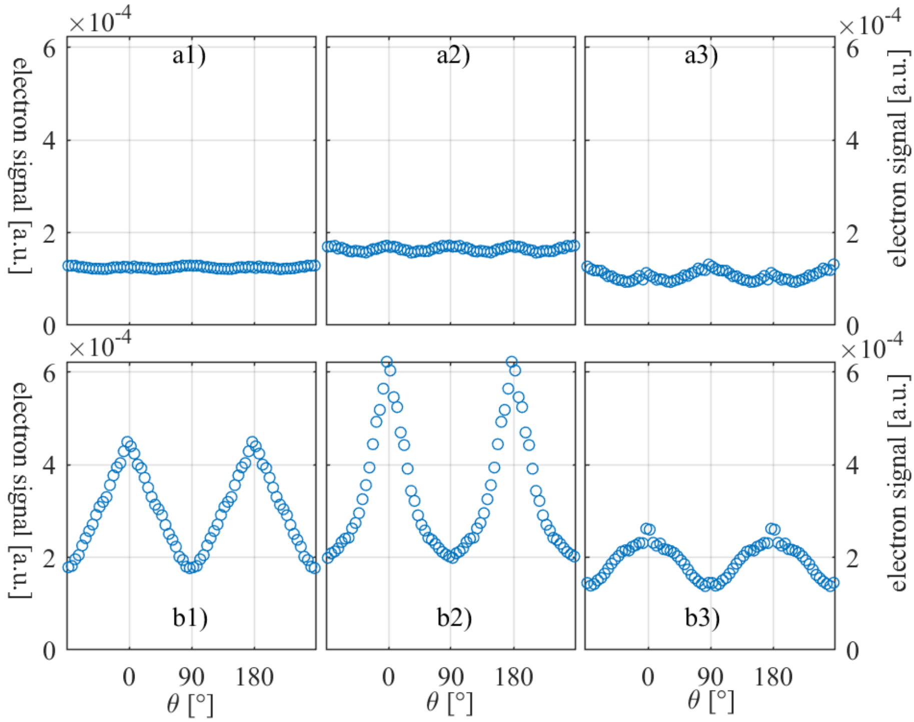

Figure 5.25: Angular distributions from the 1^1 transition of aniline, Abel inverted data (circles); for the three channels: first channel 1), second channel 2), and third channel 3). The upper row a) shows the distribution from unaligned molecules, the lower row b) the distribution from one-dimensionally aligned molecules (MPA ∥ z-axis)

5.3.5 $6a^1$ vibrational mode

The 6a vibrational motion of aniline is an in-plane motion deforming the benzene ring [102]. The probe wavelength to address the 6a vibrational mode of the S_1 state has been set to 289.6 nm (see also fig 5.4, 34530 cm^{-1}, 4.28 eV) with an intensity of 0.09 TW cm^{-2}.

The obtained PADs are shown in fig 5.26. The signal in the electron velocity map image obtained from unaligned molecules, fig 5.26 a), has been doubled to enhance its visibility. Three channels, labelled 1-3, with an isotropic distribution are visible. Upon aligning the molecules, either one-dimensionally with their MPA parallel to the z-axis fig 5.26 b), three-dimensionally with the MPA parallel to the z-axis fig 5.26 c), or the y-axis fig 5.26 e), or one-dimensionally with the least polarizable axis confined to the x-axis fig 5.26 d), an anistropy with an excess of signal parallel to z-axis appears in all three channels. As observed previously, the energy of the channels shifts, when the molecules are aligned. Furthermore, the one-dimensionally aligned molecules with the MPA parallel to the y-axis, exhibit an isotropic distribution.

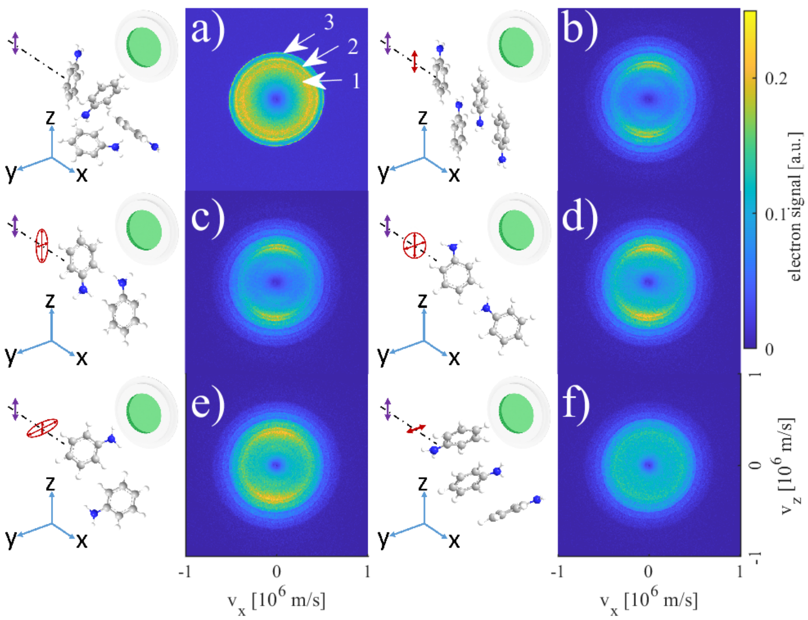

Figure 5.26: PADs from aniline molecules in gas phase $6a^1$ transition, probe wavelength 289.6 nm I=0.09 TW cm^{-2}. a) unaligned, b) 1D aligned MPA ∥ z-axis, c) 3D aligned MPA ∥ z-axis, d) 1D aligned least polarizable axis ∥ x-axis, e) 3D aligned MPA ∥ y-axis, f) 1D aligned MPA ∥ y-axis; 1-3 different channels

The angular distributions of the first channel, labelled 1 in fig 5.26 a), is shown in fig 5.27. The angular distribution of unaligned molecules, fig 5.27 a), is rather isotropic. Aligning the molecules one-dimensionally with their MPA confined parallel to the z-axis, fig 5.27 b), the angular distribution shows a two-fold structure with maxima at 0° and 180°. These maxima increase, when the molecule is three-dimensonally aligned with the MPA parallel to the z-axis, fig 5.27 c). They are only marginally smaller for three-dimensionally aligned molecules with their MPA parallel to the y-axis, fig 5.27 e). Confining the least polarizable axis parallel to the x-axis, 5.27 d), also leads to a two-fold structure with maxima at 0° and 180°. However, the maxima are smaller than in the case of one-dimensional alignment with the MPA parallel to the z-axis. With one-dimensional alignment confining the MPA parallel to the y-axis, the distribution is isotropic again.

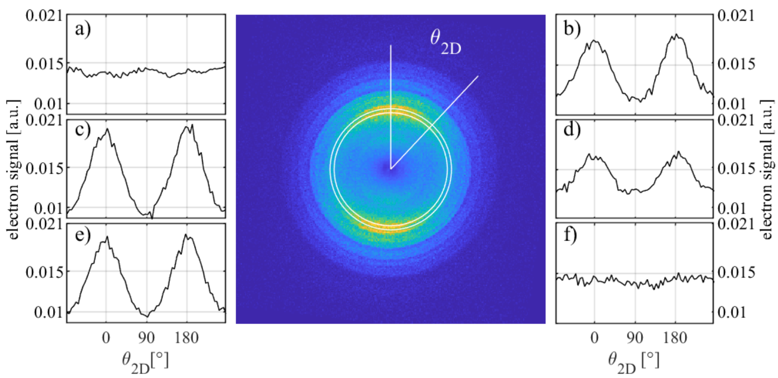

Figure 5.27: Angular distribution of the first channel, labelled 1 in fig 5.26 a). Centre image: 1D ∥ aligned with radial range. The alignment geometries used in the different subfigures are the same as in fig 5.26, i.e. a) unaligned, b) 1D aligned MPA ∥ z-axis, c) 3D aligned MPA ∥ z-axis, d) 1D aligned least polarizable axis ∥ x-axis, e) 3D aligned MPA ∥ y-axis, f) 1D aligned MPA ∥ y-axis.

Figure 5.28 shows the angular distribution of the second channel, labelled 2 in fig 5.26 a). The angular distribution of unaligned molecules, fig 5.28 a), exhibits faint maxima at 90° and 270°, which is perpendicular to the laser polarization axis. Aligning the molecules one-dimensionally with their MPA parallel to the z-axis, fig 5.28 b), reveals a two-fold structure with peaks at 0° and 180°. The confinement increases upon three-dimensional alignment with the MPA parallel to the z-axis, fig 5.28 c). The two maxima are most pronounced in this alignment geometry. Confining the least polarizable axis parallel to the x-axis, 5.28 d), also reveals a two-fold structure with maxima at 0° and 180°. However, they are also smaller than in the case of one-dimensional alignment with the MPA parallel to the z-axis, as it was the case for the first channel, fig 5.27. Aligning the molecules three-dimensionally with their MPA parallel to the y-axis, fig 5.28 e), also gives rise to two pronounced maxima at 0° and 180°. The angular distribution of molecules aligned one-dimensionally with their MPA parallel to the y-axis is isotropic, see fig 5.28 f).

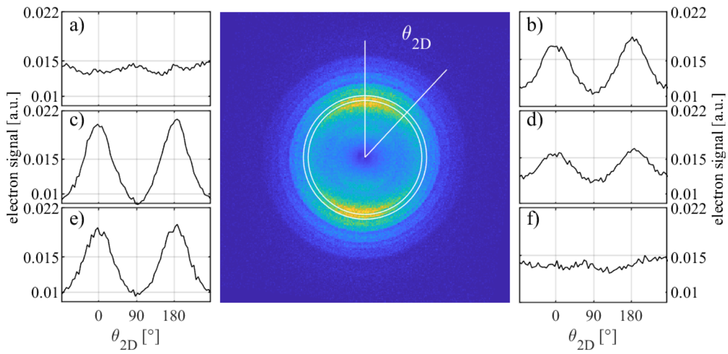

Figure 5.28: Angular distribution of the second channel, labelled 2 in fig 5.26 a). Centre image: 1D ∥ aligned with radial range. The alignment geometries used in the different subfigures are the same as in fig 5.26, i.e. a) unaligned, b) 1D aligned MPA ∥ z-axis, c) 3D aligned MPA ∥ z-axis, d) 1D aligned least polarizable axis ∥ x-axis, e) 3D aligned MPA ∥ y-axis, f) 1D aligned MPA ∥ y-axis.

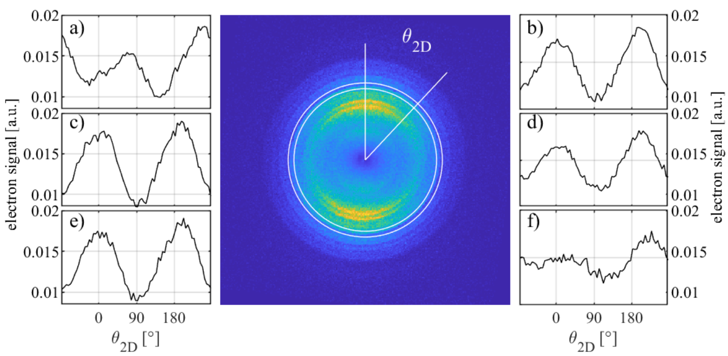

Figure 5.29: Angular distribution of the third channel, labelled 3 in fig 5.26 a). Centre image: 1D ∥ aligned with radial range. The alignment geometries used in the different subfigures are the same as in fig 5.26, i.e. a) unaligned, b) 1D aligned MPA ∥ z-axis, c) 3D aligned MPA ∥ z-axis, d) 1D aligned least polarizable axis ∥ x-axis, e) 3D aligned MPA ∥ y-axis, f) 1D aligned MPA ∥ y-axis.

The angular distributions of the third channel, labelled 3 in fig 5.26 a), are shown in fig 5.29. The unaligned distribution for this channel is not as isotropic, as it occurred in fig 5.26 a). Figure 5.29 a) exhibits clear maxima at 90° and 270°. The maximum at 90° is smaller, potentially due to a detector insensitivity between 0° and 90°. Aligning the molecules one-dimensionally with their MPA parallel to the z-axis, fig 5.29 b), shifts the maxima locations to 0° and 180°. The peaks are more pronounced than in the previous two channels. Aligning the molecules three-dimensionally, either with their MPA parallel to the z-axis, fig 5.29 c) or y-axis fig 5.29 e), enhances the confinement of the two maxima. The angular distribution of the aniline molecules with their least polarizable axis confined to the x-axis, fig 5.29 d), diminishes the two maxima. However, they are still more pronounced as in the previous two channels. Aligning the molecules one-dimensionally with the MPA parallel to the y-axis shows an assymmetric distribution. One Maximum at 225° and two suppressions at 135° and -45° can be observed. This is attributed to be a measurement artefact.

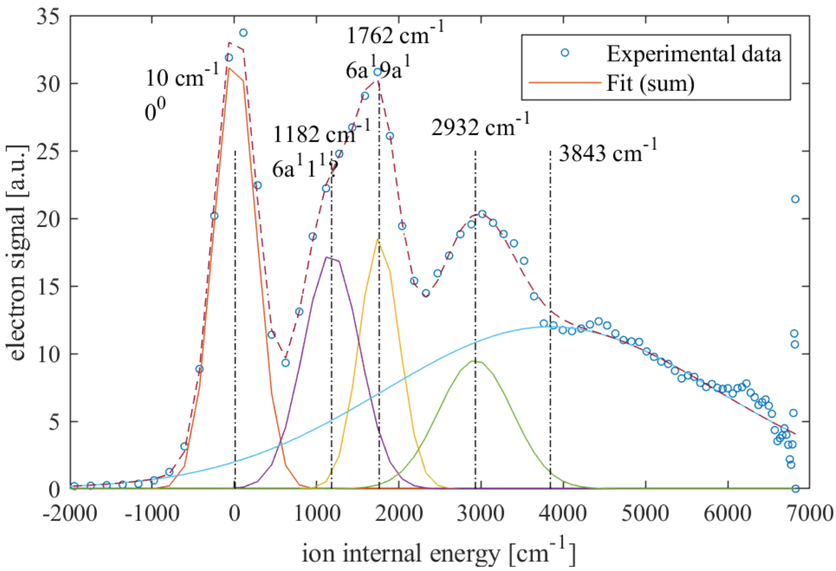

Figure 5.30: [1+1]-Photoionization photoelectron spectrum in units of ion internal energy of unaligned aniline molecules obtained via Abel inversion. $6a^1$ transition, probe wavelength 289.6 nm, I=0.09 TW cm^{-2}. Peak locations according to [102]: $6a^1 1^1$ 1338 cm^{-1}, $6a^1 9a^1$ 1711 cm^{-1}

The photoelectron spectrum of the electron velocity map image obtained from unaligned aniline molecules has been obtained via Abel inversion and is shown in units of ion internal energy in fig 5.30. Three peaks can be observed. The first peak, slightly offset from 0 cm^{-1} is assigned the origin. The second peak is a convolution of two peaks, assigned to the 6a^{1}1^1 and 6a^{1}9a^1 vibrational modes, centred at 1182 cm^{-1} and 1762 cm^{-1}. Qu et al. find the 6a^{1}1^1 vibrational mode at 1338 cm^{-1} and the 6a^{1}9a^1 vibrational mode at 1711 cm^{-1}. The third peak centred at 2932 cm^{-1} could not be assigned.

The photoelectron spectrum of one-dimensionally aligned aniline molecules with their MPA parallel to the z-axis is shown in fig 5.31. Compared to fig 5.30, several new peaks appear, also with electron kinetic energies bigger than the origin channel. As the curve is flattening for electron kinetic energies bigger than 0.83 eV, this is likely the origin. However, mathematically, the peak at 0.98 eV is a better fit (calc. 0.92 eV; two photons 2*34829 cm^{-1} = 69658 cm^{-1}, IP 62271 cm^{-1} [102], 7387 cm^{-1}). The higher energetic channels are reached through the absorption of an alignment photon via the S_2 and S_3 states as intermediate states. With the absorption of another UV-photon, the cation ground state is reached. Table 5.5 summarizes the peak locations and their respective assignments.

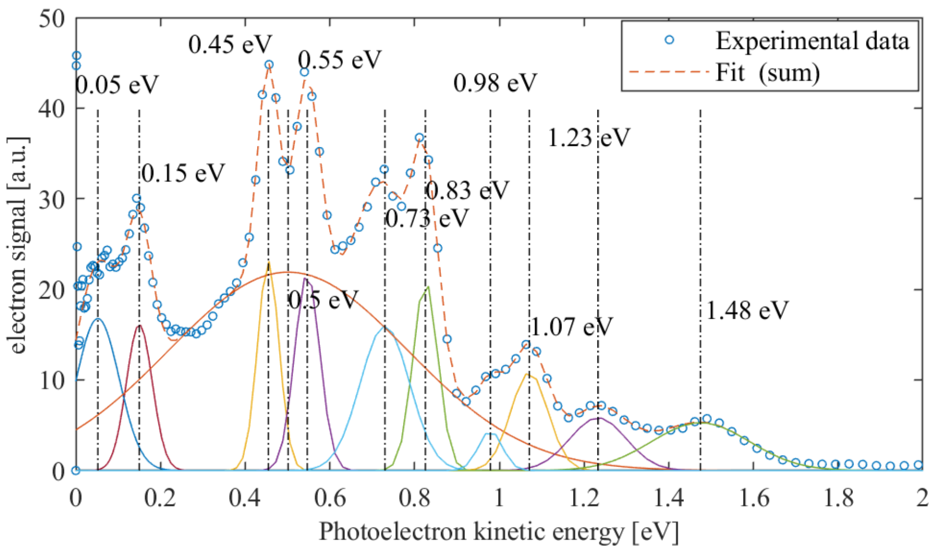

Figure 5.31: Photoelectron spectrum from 1D aligned aniline molecules (MPA ∥ z-axis) in gas phase obtained via Abel inversion. 6a^1 transition, 289.6 nm, I=0.09 TW cm^{-2}. The peaks are assigned in tab 5.5

eKE [eV]	Assignment
0.05	
0.15	
0.45	
0.55	$6a^1 1^1$ and $6a^1 9a^1$ (?)
0.73	
0.83	0^0 (?)
0.98	0^0 (?)
1.07	via S_2, $6a^1$ (?)
1.23	via S_2, 0^0
1.48	via S_3, 0^0 (?)

Table 5.5: Peak locations in photoelectron kinetic energy and assignment

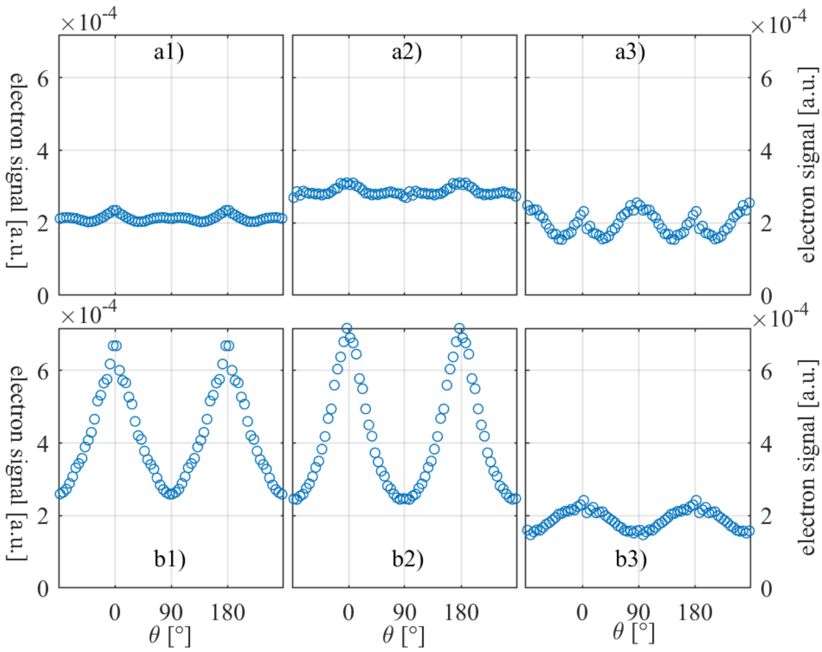

Figure 5.32: Angular distributions from the $6a^1$ transition of aniline, data extracted from the Abel inverted images (circles) for the three channels: first channel 1), second channel 2), and third channel 3). The upper row a) shows the distribution from unaligned molecules, the lower row b) the distribution from one-dimensionally aligned molecules (MPA ∥ z-axis)

The angular distributions of the Abel inverted images have been extracted and are shown in fig 5.32. The two less energetic channels obtained from the Abel inverted images of the unaligned aniline molecules exhibit rather isotropic distributions, see fig 5.32 a1) and a2). The third channel, fig 5.32 a3), exhibits four small maxima at 0°, 90°, 180° and 270°. Aligning the molecules one-dimensionally results in a two-fold structure with maxima at 0°and 180° for all three channels, fig 5.32 b1)-b3). The maxima are most pronounced for the two less energetic channels, fig 5.32 b1) and b2).

5.4 Conclusion and discussion

Aniline molecules in gas phase have been aligned and the PADs have been extracted using resonant [1+1]-photoionization. The addressed resonances were the 0^0, 1^1 and the $6a^1$ vibrational mode of the electronically excited S_1-state.

Each of the three resonances showed three channels in the electron velocity map image of the unaligned molecule. The origin channel of each electron velocity map image of the unaligned molecules exhibited an anisotropy with an excess of signal perpendicular to the probe pulse polarization. Upon aligning the molecule, one-dimensionally with the MPA parallel to the z-axis, three-dimensionally with the MPA parallel to the z- or y-axis or confining the least polarizable axis to the x-axis, the angular distributions showed maxima at 0° and 180°. They were most pronounced for three-dimensional alignment with the MPA parallel to the z-axis. For one-dimensional alignment with the MPA confined parallel to the y-axis, an isotropic distribution was obtained.

Besides aligning the molecules, the alignment pulse had further effects on the molecule. Photons of the alignment pulse have been absorbed and this caused new ionization channels. Furthermore, the energies of the respective channels shifted. This might also be due to photons of the alignment pulse being absorbed.

Korter et al. found that the orientation of the nitrogen lone pair played an important role in the charge transfer [100]. If the amino group and the benzene ring are in plane with one another, the overlap between the lone pair and the π-orbital of the benzene ring is enhanced [100]. This increases the electron transfer from the amino group to the benzene ring. Although, the intensity of the alignment pulse is comparatively weak. Additionally, if the orientation of the lone pair was responsible for this shift, the different forms of alignment should have different effects on the shift. The shift should react differently to one- and three-dimensional alignment. Thus, I deem this explanation unlikely. Another explanation, as mentioned before, is that the absorption of the alignment photons also causes a shift in energy for the respective channels.

This theory could be tested if the two-photon experiment would be repeated as a one-photon experiment. If the channels still shifted, the shift would be caused by the molecule being aligned and not by alignment photons being absorbed. Additionally, the undesired extra channels appearing upon alignment with photoelectron kinetic energies higher than the origin channel would not exist in this experiment. This would be the case since the photons of the alignment pulse in the two-photon experiment were absorbed when the molecule is in the electronically excited S_1-state.

An alignment intensity study with theoretical calculations showed a possible form for the original MFPAD. It has most likely a four-fold structure with twelve lobes. The four lobes with the highest probability of a photoelectron emission are found in the direction of the amino group.

CHAPTER 6

Naphthalene

Naphthalene is an aromatic molecule with D_{2h}-symmetry, see fig 6.1. It has been investigated in various spectroscopy studies [115–122] and also MFPADs from strong-field ionization have been documented [63]. The transition dipole moment of the $S_1 \leftarrow S_0$ transition is parallel to its most polarizable axis (MPA, dashed line in fig 6.1). Comparing naphthalene and aniline, naphthalene is a favourable molecule for laser-induced alignment because of its larger polarizability anisotropy (see section 6.1). The disadvantage of naphthalene compared to aniline is its large variety of vibrational modes with comparatively little separation in energy (see sections 6.2 and 6.3.1).

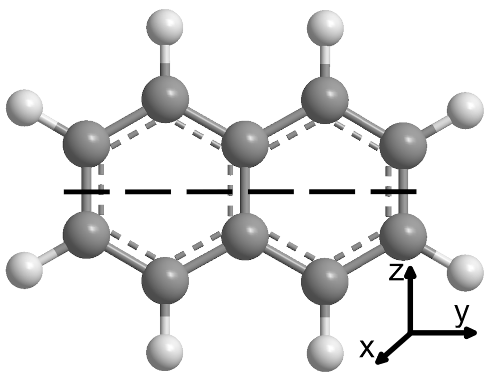

Figure 6.1: Structure of naphthalene, dashed line: MPA

6.1 Laser-induced alignment of naphthalene molecules

In the following section, I will make numerical estimates for the degree of alignment for one-dimensionally aligned naphthalene molecules, analogous to the calculations done for aniline, see section 5.1. As mentioned previously, in order to access MFPADs in the laboratory frame, a high degree of alignment is necessary [48]. One-dimensional alignment is induced by a linearly polarized laser pulse and confines the MPA to the polarization axis of the laser pulse, see also section 2.2. The degree of alignment has been estimated using the alignment calculator briefly explained in section 2.2.3. For this calculation, the actual pulse shape of the truncated alignment pulse is used, see grey area fig 6.2. This pulse turns on in about 150 ps, has a FWHM of 110 ps and rapidly turns off in ca. 10 ps.

	Polarizability [Å^3]			Rotational constants [GHz]
	x	y	z	
x	9.826	0.000	0.000	0.879
y	0.000	**25.712**	0.000	3.106
z	0.000	0.000	**18.700**	1.226

Table 6.1: Polarizability and rotational constants of aniline, most polarizable axis and second most polarizable axis highlighted, B3LYP/aug-cc-pVDZ [123, 124]

Naphthalene is, like aniline, an asymmetric top rotor. In order to use the alignment calculator it needs to be approximated as a symmetric top rotor. As previously done for aniline, two means of approximation have been used. As a conservative estimate the highlighted polarizabilities in tab 6.1 have been used:

$$\Delta\alpha = \alpha_{yy} - \alpha_{zz} = 7.012\,\text{Å}^3 \tag{6.1}$$

Comparing the result with aniline (2.712 Å^3), the polarizability anisotropy is considerably larger – already for the conservative estimate. Thus, it can be expected to achieve higher degrees of alignment with naphthalene than with aniline. However, the conservative estimate is likely to underestimate the true degree of alignment, since the most polarizable axis and the least polarizable axis exhibit a significant difference in polarizability (x- and y-direction, see tab 6.1). Consequently, the least polarizable axis is in all probability oriented perpendicular to the polarization direction, which is not considered with this approximation. The conservative estimate rather focusses on the most and second-most polarizable axis competing with one another, still favouring the most polarizable axis over the second most polarizable axis. Taking the least polarizable axis into consideration, another means of calculating the polarizability anisotropy has been used, eq 6.2. The resulting polarizability, 11.449 Å^3, is expectedly higher than the conservative estimate and twice as much as for aniline with the same approximation (5.509 Å^3).

$$\Delta\alpha = \alpha_{yy} - \frac{\alpha_{xx} + \alpha_{zz}}{2} = 11.449\,\text{Å}^3 \tag{6.2}$$

The resulting calculated degrees of alignment are shown in fig 6.2. As naphthalene has a higher polarizability anisotropy than aniline, less intensities are required to align the molecule. Thus, the alignment pulse peak intensity used in the experiments (0.58 TW cm^{-2}) is smaller than the one used for aligning aniline molecules (0.81 TW cm^{-2}). The alignment traces shown in fig 6.2 are calculated with a peak pulse intensity of 0.58 TW cm^{-2}, which represents the compromise between maximizing the degree of alignment and minimizing unwanted side effects the alignment pulse has on the naphthalene molecule. The conservative estimate is shown as a solid line, the averaged estimate is displayed as a dashed line. The grey area shows the pulse shape of the alignment pulse. When the pulse begins (t=-200 ps), the molecules are randomly oriented ($\langle\cos^2\theta\rangle = 0.33$). As the pulse adiabatically turns on, the degree of alignment increases. The degree of alignment is maximized at the peak of the pulse, resulting in a degree of alignment of $\langle\cos^2\theta\rangle = 0.79$ for the conservative estimate and $\langle\cos^2\theta\rangle = 0.83$ for the averaged estimate. With the truncation of the pulse (t=0 ps), the molecules do not experience the torque of the aligning electric field any more and start to rotate freely again. The degree of alignment decrease is retarded in time compared to the decrease in the alignment pulse. As discussed in section 5.1, this time window is insufficient to conduct a field-free experiment with a probe pulse duration of 6 ps. After 30 ps the degree of alignment converges to around $\langle\cos^2\theta\rangle = 0.42$. Any revivals are missing in the time window considered for this calculation.

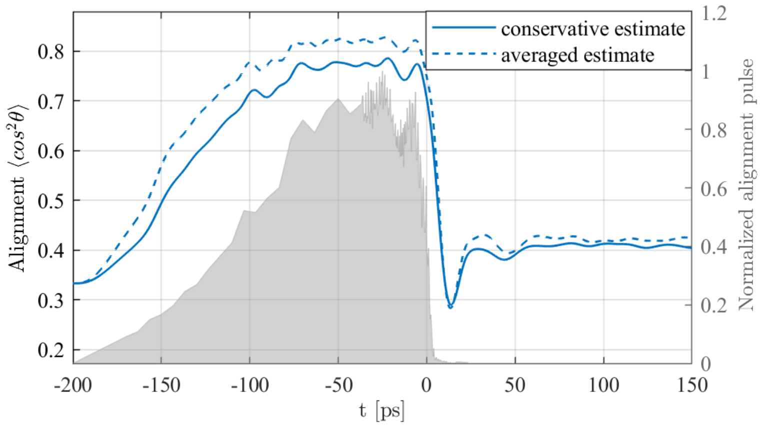

Figure 6.2: Calculated alignment traces, solid line: conservative estimate, dashed line: averaged estimate, grey area: normalized pulse trace

An alignment intensity study as presented for aniline in section 5.3.3 has not been conducted for the naphthalene experiments. The alignment pulse intensity was adjusted on sight with a qualitative data acquisition insufficient for a quantitative analysis.

6.2 Ionization pathways

Naphthalene has a larger number of vibrational modes than aniline. The notation for the vibrational modes used here follows the notation introduced by Stockburger et al. in 1975, who found two different types of modes: a_g modes and b_{1g} modes [117]. They introduced a binary way of notating: b_{1g} modes are numbered with barred numbers ($\bar{8}$ ... $\bar{1}$), while a_g modes are denoted without (9...1). The higher the frequency, the smaller the number. Vibrational modes of the cation in this manuscript are denoted with a plus, e.g. 7^+, as introduced by Hiraya et al. [121]. Cockett et al. also documented a_u, b_{1u} and b_{2u} modes in 1993 [122]. However, the majority of modes are still attributed to modes of either a_g or b_{1g} symmetry. In addition to the greater number of vibrational modes available, they are often also in close vicinity to one another. Although the spectral FWHM of our pulse is only approx. 6 cm^{-1}, the overall width of the pulse is approx. 22 cm^{-1}. Consequently, especially combined vibrational modes, such as $\bar{6}^1 8^1$ at 1862 cm^{-1} [122] with respect to the S_1-state and the $6^1 8^1$ at 1868 cm^{-1} with respect to the S_1-state [122] cannot be addressed without a contribution from the other. The presented addressed vibrational modes, $\bar{8}^1 7^1 8^1$ (2122 cm^{-1} above S_1 [121]), $\bar{8}^1 \bar{7}^1 8^1$ (2049 cm^{-1} above S_1 [122]) and

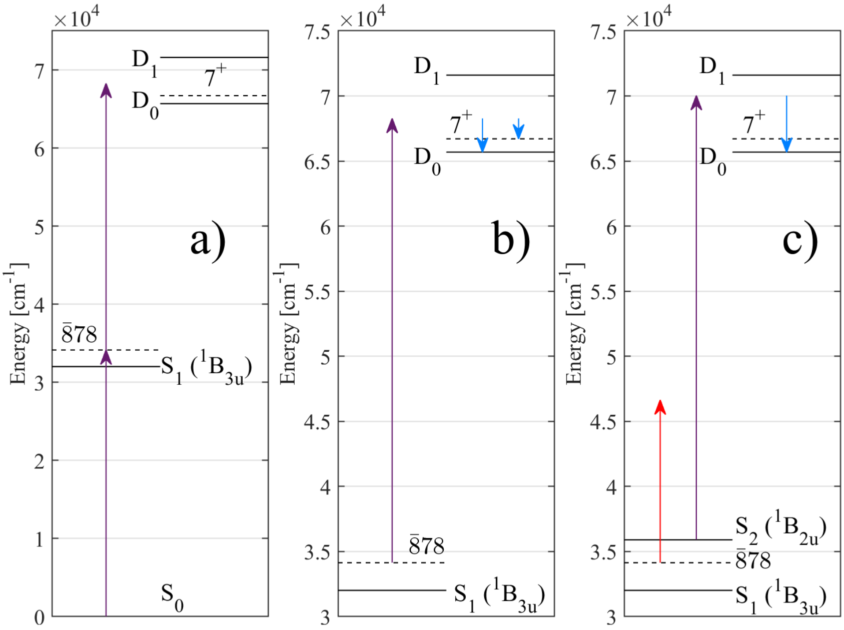

Figure 6.3: a) [1+1] photoionization targeting the $\bar{8}^1 7^1 8^1$-vibrational mode of the S_1-state b) Zoom on the absorption of the second photon, leaving the cation in the ground state and its 7^+-vibrational mode c) Rivalling photoionization channel through the absorption of an alignment pulse photon

3^1 (1435 cm^{-1} above S_1 [122]) have been selected because no other vibrational modes closer than 11 cm^{-1} have been reported.

The conducted experiments were one-colour two-photon ionization experiments. In the presented measurements, the 0^0 transition was not available for two reasons. The ionization potential of naphthalene is 65687 cm^{-1} [122] (8.14 eV), while the origin of the first excited state S_1 is at 32019 cm^{-1} [122] (3.97 eV). Thus three photons with an energy of 32019 cm^{-1} would be necessary to ionize the system. Furthermore, the conversion efficiency of the TOPAS is insufficiently low at this energy and requires a different optical setup for energies smaller than 33000 cm^{-1} (4.0 eV). Therefore, experiments with a [1+1]-photoionization process target the vibrational levels $\bar{8}^1 7^1 8^1$ (2122 cm^{-1} [121]), $\bar{8}^1 \bar{7}^1 8^1$ (2049 cm^{-1} [122]) and 3^1 (1435 cm^{-1} [122]). Figure 6.3 a) shows an illustration of the [1+1]-photoionization (purple arrows), addressing the $\bar{8}^1 \bar{7}^1 8^1$ vibrational mode (dashed line) of the S_1 state. Figure 6.3 b) shows a zoomed version of 6.3 a) with only the second absorbed photon illustrated. The resulting photoelectron kinetic energy, leaving the cation either in the ground state or e.g. in the 7^+ vibrational mode, is shown as two blue arrows. For clarity purposes only one vibrational mode is shown for the S_1 and the cation respectively. Aligning the molecules does not shift the energies, as seen for aniline; however, another ionization channel appears. With the absorption of an alignment photon the naphthalene molecule gets excited to the S_2 state. Another probe pulse photon is afterwards absorbed. Thus, the ascribed photoionization process is a [1+1'+1]-photoionization. The primed numbers denote the IR photon. A further discussion and comparison with other plausible ionization channels can be found in section 6.3.2 with fig 6.6.

6.3 Gas phase experiments

6.3.1 R2PI

Figure 6.4 shows two R2PI spectra with electrons and ions as the observable, respectively. They exhibit a large number of resonances. The probe pulse intensity was not constant over the presented wavelength range, 288.6 nm – 301.5 nm. This introduces a non-resonant contribution to the R2PI spectrum. As the corresponding intensity was not recorded, a Gaussian was subtracted from the data. Since the electron signal was higher than the signal obtained from ions, two different Gaussian curves were employed. However, this difference only concerned the variable a, while b and c were kept identical:

$$f(x) = a \cdot e^{\left(\frac{x-b}{c}\right)^2} \tag{6.3}$$

The red and the blue curve show the R2PI spectra obtained from naphthalene cations as the observable. Interestingly, in the range 291-294 nm, there are three peaks that appear in one spectrum, but not in the other (marked with black arrows). Furthermore, the signal level of the red curve surpasses the other. The R2PI spectra with electrons as the observable (yellow and purple) exhibit more noise, especially in the form of narrow peaks (marked with green arrows). The overall signal level of both curves is on top of each other. The resonances used in the following chapters have been marked with dashed black lines. While the calibration fits well for the $\bar{8}^1 7^1 8^1$ (292.9 nm, 4.23 eV, a in fig 6.4) and the $\bar{8}^1 \bar{7}^1 8^1$ vibrational mode (293.53 nm, 4.22 eV, b in fig 6.4), the calibration does not match for higher wavelength of the 3^1 vibrational mode (298.92 nm, 4.14 eV, c in fig 6.4). As the mixing wavelength of the TOPAS had to be adjusted in order to address this wavelength, another R2PI spectrum was taken to substantiate the optimal conditions for this resonance. The R2PI is not included in this manuscript.

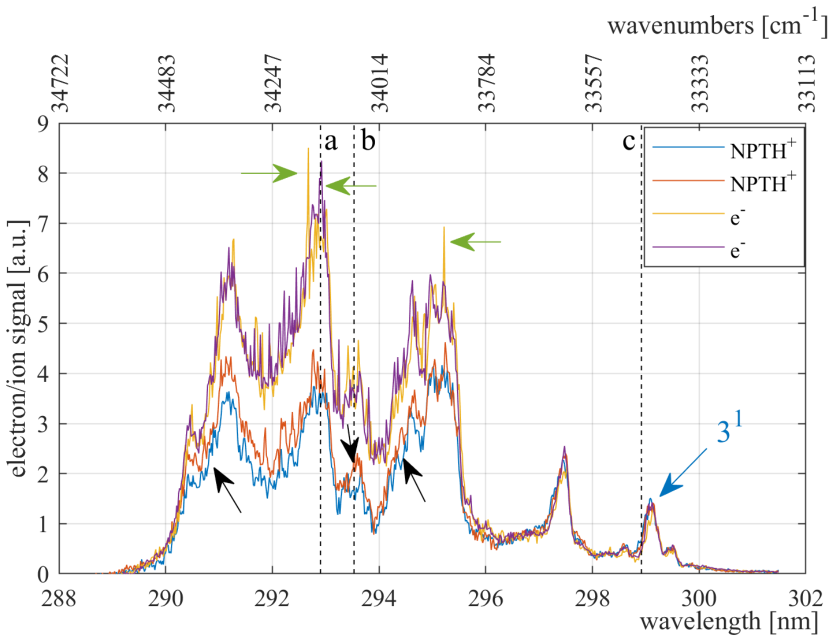

Figure 6.4: R2PI spectra, observable: red and blue curve – ions, yellow and purple curve – electrons; vibrational modes: a $\bar{8}^1 7^1 8^1$, b $\bar{8}^1 \bar{7}^1 8^1$, c 3^1 (actual wavelength). Black arrows: peaks appearing in one ion spectrum, that are not found in the other. Green arrows: Enhanced noise in the electron spectra. Blue arrow: The 3^1 vibrational mode in the recorded spectra (mismatching calibration)

6.3.2 $\bar{8}^1 7^1 8^1$ vibrational mode

The vibrational mode $\bar{8}^1 7^1 8^1$ of the S_1-state has been addressed at 34142 cm^{-1} (S_1 32020 cm^{-1} + 2122 cm^{-1} [121], 292.9 nm, 4.23 eV). The molecules have been aligned with an intensity of 0.58 TW cm^{-2}. The probe pulse had a peak intensity of 0.57 TW cm^{-2}, which is considered high for an attempted weak field experiment. The resulting electron velocity map images are shown in fig 6.5. As in chapter 5, the different alignment geometries are illustrated to the left of each electron velocity map image. All images are normalized and on the same scale. Each of the subfigures exhibits three prominent channels, centred at 0.04 eV (1), 0.14 eV (2), and 0.33 eV (3) and also a multiphoton background resulting from the comparatively high intensity of the probe pulse. The image in fig 6.5 a) shows a mild confinement along the z-axis for all three channels. Upon aligning the naphthalene molecules one-dimensionally along the z-axis, fig 6.5 b), a suppression in the PADs along the direction of the probe pulse polarization parallel to the z-axis takes place for the channels labelled 2 and 3.

Furthermore, the signal increases, which I ascribe to the fact that the transition dipole moment of the $S_1 \leftarrow S_0$ transition is parallel to the MPA, which is now brought along the polarization axis of the probe pulse. Aligning the molecules three-dimensionally with their MPA parallel to the z-axis, the suppression in channel 3 increases, while the signal levels are roughly the same. A suppression in channel 2 is not distinguishable. For three-dimensional alignment with the MPA parallel to the y-axis, fig 6.5 e), any suppression vanishes. This is also the case for one-dimensional alignment with the MPA parallel to the y-axis. Confining the least polarizable axis to the x-axis, fig 6.5 d), the PAD becomes a mixture of three-dimensional alignment parallel to the y-axis and the z-axis. It exhibits less suppression than fig 6.5 c), however still more than fig 6.5 e). When the least polarizable axis is aligned parallel to the x-axis, the benzene planes are confined to the yz-plane. The MPA is just confined to this plane, not to any axis.

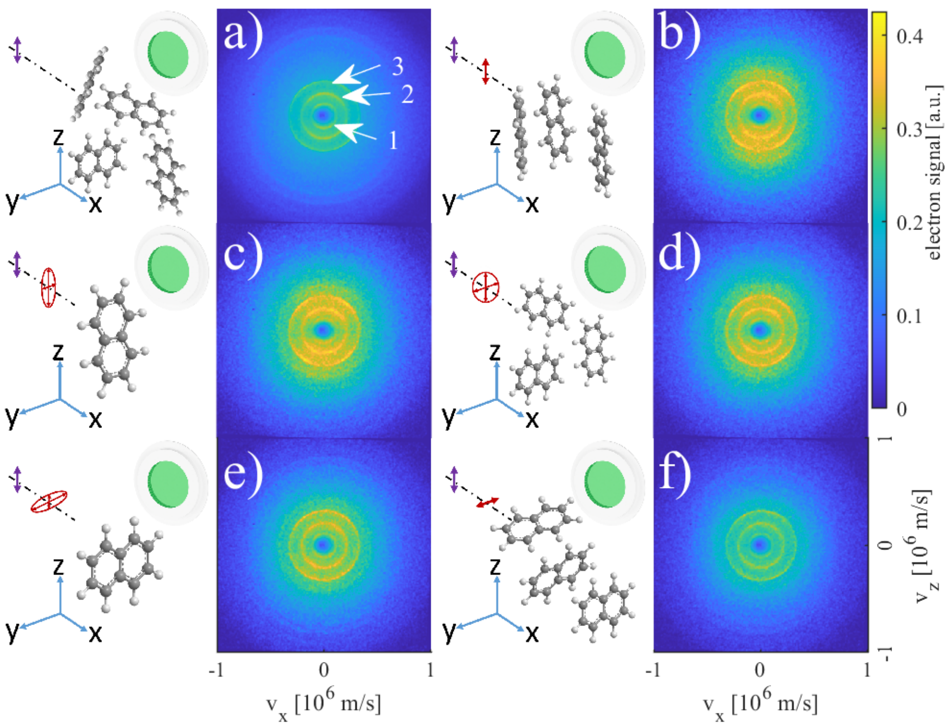

Figure 6.5: Two-dimensional velocity images of electrons produced when the probe pulse (292.9 nm) ionizes the naphthalene molecules. The wavelength of the probe pulse is set to excite the $\bar{8}^1 7^1 8^1$ vibrational state in the S_1 electronic state

The electron velocity map images of fig 6.5 a) and b) have been Abel-inverted to obtain the photoelectron kinetic energy distributions, see fig 6.6. The three channels of fig 6.5 a) and b) are readily seen as three prominent peaks in fig 6.6. The first channel is found at 0.04 eV and can be assigned to the $\bar{8}_1{}^{+}7_1{}^{+}8_1{}^{+}$ vibrational level of the cation, in good agreement with the measurement of Hiraya et al. (0.063 eV [121]). The second prominent channel, 0.14 eV, is assigned to the $\bar{8}_1{}^{+}7_1{}^{+}$ vibrational level (0.146 eV [121]). The origin, i.e. the naphthalene cation left in the vibrational ground state, is found as the third prominent peak, at 0.33 eV (0.332 eV [121]). Hiraya et al. assigned five channels more, which are either not clearly resolved and distinguishable from other peaks in fig 6.6 or not significantly above the noise level. They found the $\bar{8}_2{}^{+}7_1{}^{+}$ vibrational level at 0.094 eV, which could likely be the first dash-dotted arrow. Furthermore, they assigned the $\bar{8}_1{}^{+}8_1{}^{+}$ and the $7_1{}^{+}$ vibrational mode at 0.182 eV and 0.207 eV, which might be the second channel, marked with the second dash-dotted arrow. The last two vibrational modes they assigned are the $8_1{}^{+}$ and the $\bar{8}_1{}^{+}$ vibrational mode, 0.236 eV and 0.273 eV, which are tentatively assigned with dotted arrows, although the peaks do not exceed the noise level. Upon aligning the molecules, a new peak centred at 0.58 eV appears, labelled A in fig 6.6. This peak is observed in all photoelectron kinetic energy spectra of naphthalene at the same kinetic energy, see also fig 6.13 and fig 6.19. This indicates a process involving a particular state of the naphthalene molecule and a photon of the alignment beam. Several possible pathways have been considered, using the ionization potential stated by Hiraya et al. 65665 cm^{-1} [121] (8.142 eV) and Cockett et al. 65687 cm^{-1} [122] (8.144 eV). Ionization directly from the ground state, S_0, requires six IR photons, resulting in a photoelectron kinetic energy of 1.15-1.16 eV, leaving the naphthalene singly ionized. The alignment pulse intensity has been chosen as to avoid ionization with the alignment pulse only. Once the molecule is excited to the S_1 state, it can absorb an IR photon and decay into the S_2 (35900 cm^{-1} [121], 4.45 eV). Another UV photon ionizes the molecule. The resulting calculated photoelectron kinetic energy is 0.54 eV, which is within the VMI resolution. The suggested photoionization process is a [1+1'+1]-photoionization.

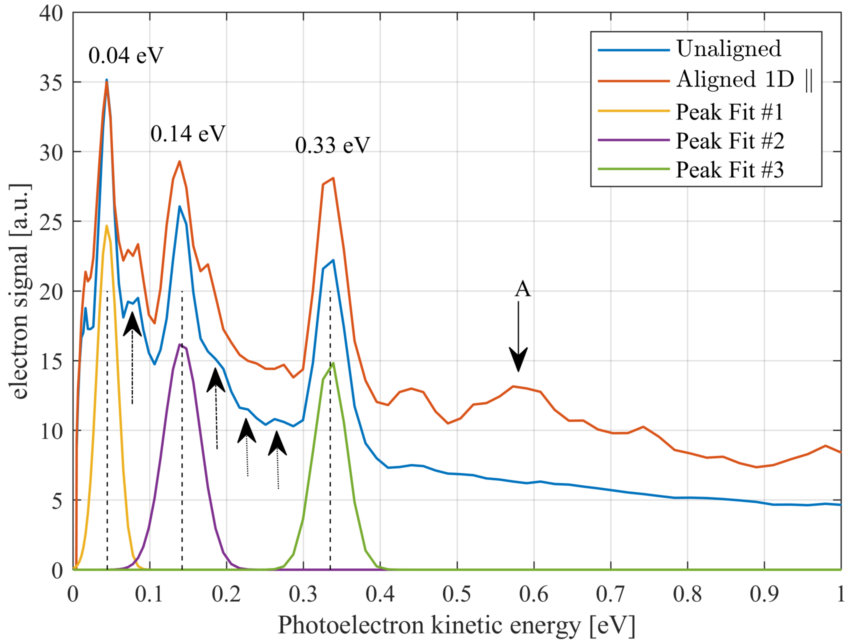

Figure 6.6: Photoelectron kinetic energy distribution obtained through Abel inversion from the electron velocity map images in fig 6.5 a) and b) 1D-aligned (MPA ∥ z-axis). PES of unaligned naphthalene molecules - blue, PES of aligned naphthalene molecules - red. The three channels are fitted with gaussians. The arrows mark smaller maxima, for assignment see text. A - channel ascribed to a [1+1'+1]-photoionization. Probe wavelength: 292.9 nm

The angular distributions of the three most prominent channels, labelled 1, 2 and 3 in fig 6.5 a), have been evaluated and are shown in fig 6.7, 6.8, and 6.9. The labelling a)-f) refers to the same alignment geometries as used in fig 6.5.

The angular distributions of the $\bar{8}_1{}^+7_1{}^+8_1{}^+$ vibrational level (channel 1 in fig 6.5) are shown in fig 6.7. The unaligned distribution, fig 6.7 a), exhibits a two-fold structure with a suppression at 90° and -90°, more pronounced at -90°. Upon three-dimensional alignment, either with the MPA parallel to the z-or y-axis, fig 6.7 c) and e) respectively, the suppression at 90° becomes slightly more pronounced. Aligning the naphthalene molecules one-dimensionally with their MPA parallel to the z-axis, fig 6.7 b), does not change the distribution compared to the unaligned distribution, fig 6.7 a). With one-dimensional alignment of the MPA parallel to the y-axis, fig 6.7 f), the suppression at 90° vanishes as it does when least polarizable axis is fixed to the x-axis, fig 6.7 c).

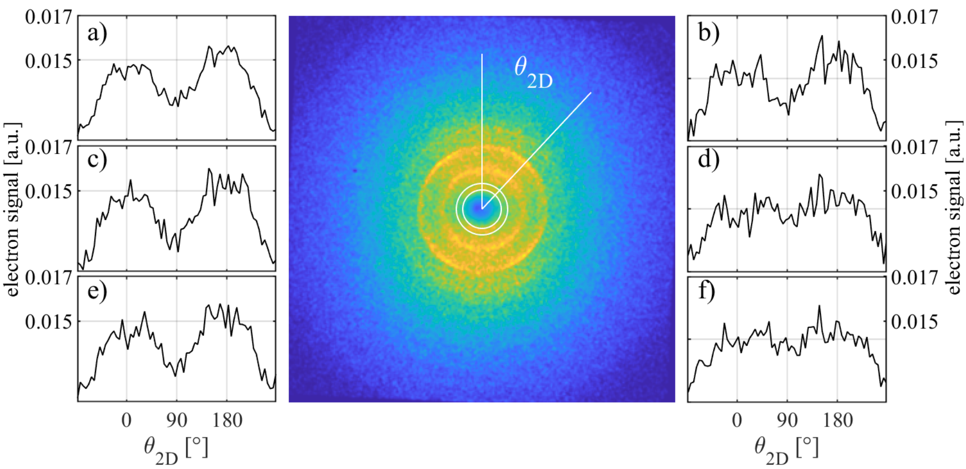

Figure 6.7: Angular distribution of the first channel (labelled 1 in fig 6.5), centre image: 1D ∥ aligned with radial range. The alignment geometries used in the different subfigures are the same as in fig 6.5, i.e. a) unaligned, b) 1D aligned MPA ∥ z-axis, c) 3D aligned MPA ∥ z-axis, d) 1D aligned least polarizable axis ∥ x-axis, e) 3D aligned MPA ∥ y-axis, f) 1D aligned MPA ∥ y-axis.

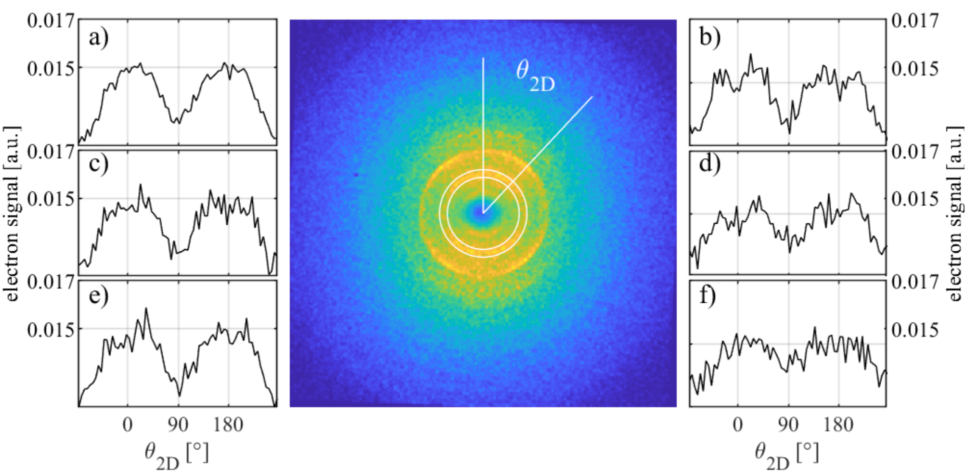

Figure 6.8: Angular distribution of the second channel (labelled 2 in fig 6.5), centre image: 1D ∥ aligned with radial range. The alignment geometries used in the different subfigures are the same as in fig 6.5, i.e. a) unaligned, b) 1D aligned MPA ∥ z-axis, c) 3D aligned MPA ∥ z-axis, d) 1D aligned least polarizable axis ∥ x-axis, e) 3D aligned MPA ∥ y-axis, f) 1D aligned MPA ∥ y-axis.

Figure 6.8 shows the angular distributions of the second channel, labelled 2 in fig 6.5, the $\bar{8}_1{}^{+}7_1{}^{+}$ vibrational mode. The unaligned distribution reveals the two-fold structure with a signal suppression at 90° and -90°. This channel also exhibits a difference in the suppression at 90° and -90°; however, not as significant as in the first channel. Aligning the molecules one-dimensionally with the MPA parallel to the z-axis, fig 6.8 b), results in another suppression at 0° and 180°. It disappears again upon three-dimensional alignment with the MPA parallel to the z-axis, fig 6.8 c). As this is also the electron velocity map image with the highest intensity, the suppression might be overshadowed by the bright origin channel. When the least polarizable axis is confined parallel to the x-axis, fig 6.8 d), the suppression at 0° and 180° reappears, while the suppression at 90° and -90° becomes less pronounced. Upon three-dimensional alignment with the MPA parallel to the y-axis, fig 6.8 e), the suppression at 90° and -90° strongly resembles the three-dimensional case with the MPA parallel to the z-axis. Interestingly, in the case of one-dimensional alignment with the MPA parallel to the y-axis, fig 6.8 f), the distribution resembles almost an isotropic distribution with only a slight suppression at 90° and -90°.

The origin channel's angular distribution is shown in fig 6.9. The detector has a slight detection inefficiency for this energy region between -90° and 0°. The angular distribution of the unaligned molecules, fig 6.9 a), again exhibits the suppression at 90° and -90°. It furthermore shows a slight suppression at 0° and 180°. Upon aligning the molecules one-dimensionally with their MPA parallel to the z-axis, fig 6.9 b), the suppressions at 0° and 180° become more pronounced. With three-dimensional alignment with the MPA parallel to the z-axis, fig 6.9 c), the suppression at 90° and -90°, as well as 0° and 180° becomes most pronounced. The suppression at 90° is less pronounced for three-dimensional alignment with the MPA parallel to the y-axis, fig 6.9 e). However, a suppression at 0° and 180° is still visible. Upon one-dimensional alignment confining the least polarizable axis to the x-axis, fig 6.9 d), or confining the MPA to the y-axis, fig 6.9 f), the suppression at 90° and -90° is less pronounced, while the suppression along the z-axis, 0° and 180°, is missing.

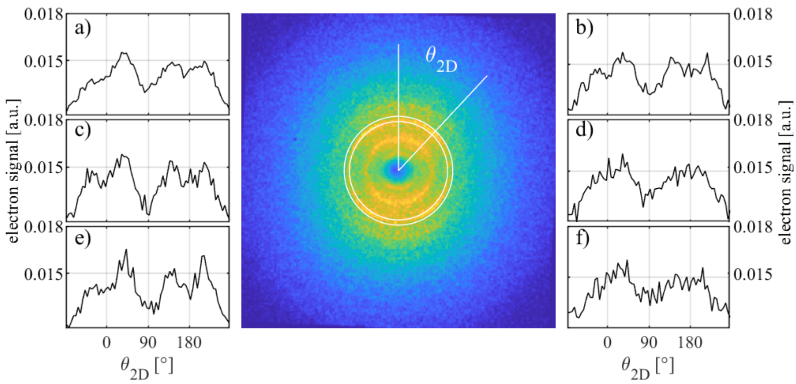

Figure 6.9: Angular distribution of the third channel (labelled 3 in fig 6.5), centre image: 1D ∥ aligned with radial range. The alignment geometries used in the different subfigures are the same as in fig 6.5, i.e. a) unaligned, b) 1D aligned MPA ∥ z-axis, c) 3D aligned MPA ∥ z-axis, d) 1D aligned least polarizable axis ∥ x-axis, e) 3D aligned MPA ∥ y-axis, f) 1D aligned MPA ∥ y-axis.

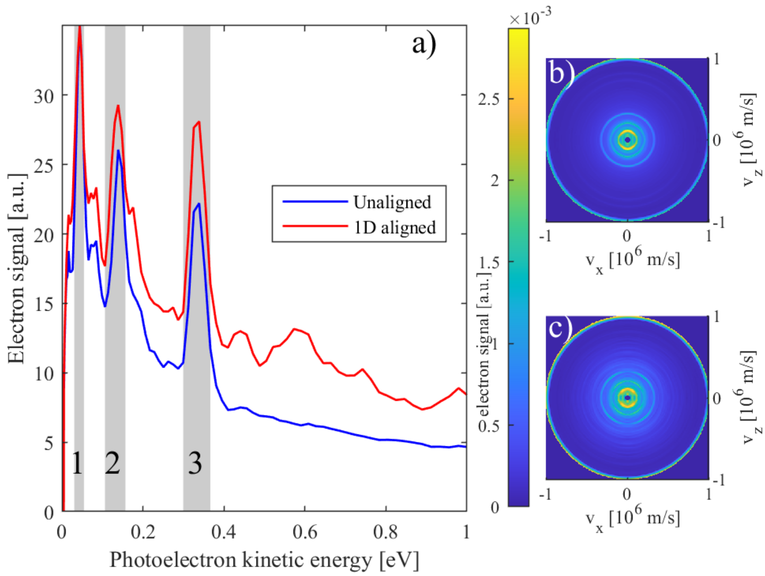

Figure 6.10: a) [1+1]-Photoionization photoelectron kinetic spectrum of aligned and unaligned naphthalene molecules, probe wavelength set to $\bar{8}^1 7^1 8^1$ vibrational state of the S_1 (292.9 nm), grey areas (1-3) used for β-calculation. b) Abel inverted image of the unaligned molecules. c) Abel inverted image of the molecules aligned 1D, MPA ∥ to the z-axis

A normalized version of the photoelectron kinetic energy spectrum is shown in fig 6.10 a). The areas, that have been used for the β-calculation have been marked in grey. The numbers follow the label on the channels in fig 6.5. Compared to the photoelectron kinetic energy spectra of aniline, it is striking that the relative peak intensities do not change significantly. The first channel is the one with the highest intensity, followed by the second channel and the third channel exhibits the least signal. Furthermore the peak positions do not shift. However, there is evidence of an alignment photon being absorbed. A peak at 0.59 eV appears in the photoelectron kinetic energy distribution of one-dimensionally aligned molecules. Figures 6.10 b) and c) show the Abel inverted electron velocity map image of the unaligned and aligned naphthalene molecules, respectively. While only the lower lying two channels in the unaligned case show a two-fold structure, favouring the direction of the z-axis, the origin channels appears rather isotropic. In the aligned case, all three channels exhibit a four-fold symmetry with a suppression along the x- and the z-axis.

Figure 6.11 shows the angular distribution from the Abel inverted images along with a fit through the β-parameters. Figures 6.11 a1)-a3) represent the unaligned case, figs b1)-b3) the aligned one. The numbers follow the labelling in fig 6.10. The channel with the lowest kinetic energy shows a two-fold structure with a favoured emission along the z-axis at 0° and 180°, fig 6.11 a1). Upon aligning the molecules a suppression is introduced at 0° and 180°. This could not be resolved in the raw electron velocity map images for the two-dimensional θ_{2D}, probably due to overshadowing and averaging effects. For the second channel, a broadened two-fold structure, with maxima at 0° and 180° is seen in the unaligned distribution, fig 6.11 a2). When the molecules are aligned, fig 6.11 b2), a clear additional suppression at 0° and 180° can be observed. In the raw electron velocity map images for θ_{2D}, only a slight indication of this effect could be observed. For the third channel, the origin, the effect of the alignment pulse is most remarkable. The unaligned distribution, fig 6.11 a3), appears rather isotropic, with suppressions at 90° and 270°. In contrast, the aligned distribution shows four peaks at -45°, 45°, 135° and 225°.

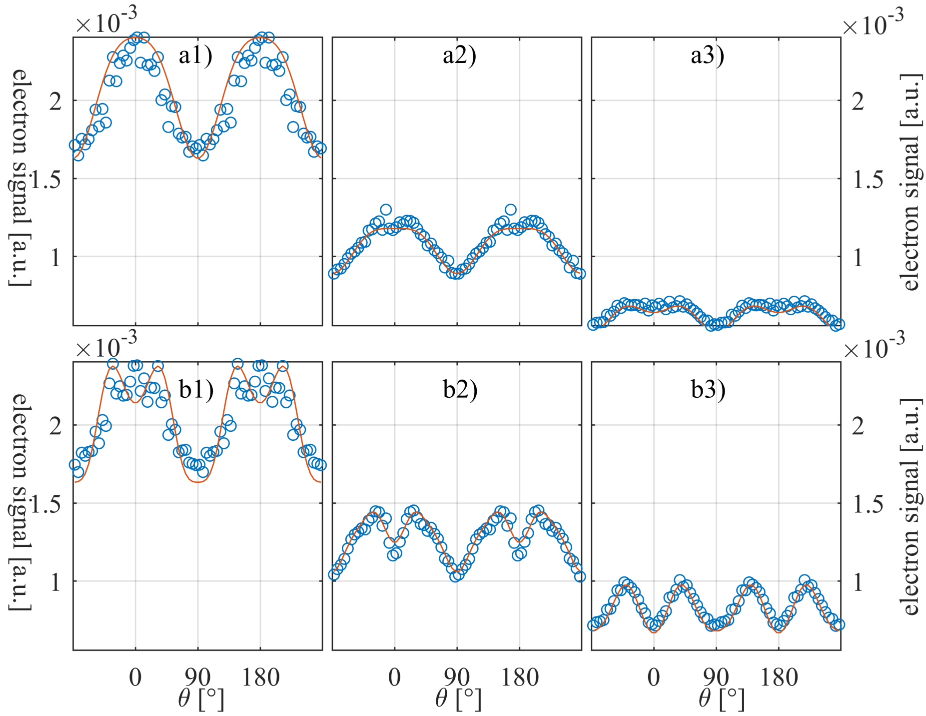

Figure 6.11: Angular distributions from the $\bar{8}^1 7^1 8^1$ transition of naphthalene, raw Abel inverted data (circles) and fit (solid line); for the three channels: first channel 1), second channel 2), and third channel 3). The upper panel a) shows the distribution from unaligned molecules, the lower panel b) the distribution from one-dimensionally aligned molecules (MPA ∥ z-axis)

6.3.3 $\bar{8}^1\bar{7}^1 8^1$ vibrational mode

The vibrational mode $\bar{8}^1\bar{7}^1 8^1$ is 2049 cm^{-1} [122] above the vibrational ground state of the S_1 state (32019 cm^{-1} [122]). Therefore, the probe wavelength to excite this state has been set to 34068 cm^{-1} (293.53 nm, 4.22 eV, I=0.57 TW cm^{-2}). The molecules have been aligned with an intensity of 0.58 TW cm^{-2}.

The electron velocity map images with the respective experimental setup geometry are shown in fig 6.12. The unaligned electron distribution in fig 6.12 a) exhibits two channels, labelled 1 and 2. The channels are centred around 0.13 eV and 0.32 eV. The low energy channel is most likely a combination of the $\bar{8}^+ 8^+$, $\bar{8}^+ 7^+$, and $\bar{8}^+\bar{7}^+$ vibrational mode of the cation. The origin can be assigned to the second channel at 0.32 eV. Both channels exhibit a two-fold structure, favouring an emission along the z-axis, fig 6.12 a). Upon aligning the molecules one-dimensionally with their MPA parallel to the z-axis, fig 6.12 b), the second channel exhibits a clear four-fold structure. Along the z-axis, a clear suppression of photoelectron emission appears. For the second channel, this becomes most pronounced with three-dimensionally aligned molecules, confining the MPA parallel to the z-axis, fig 6.12 c). Confining the least polarizable axis parallel to the x-axis, fig 6.12 d), results in an anisotropy similar to the unaligned distribution; however, with enhanced signal levels. Figure fig 6.12 e) shows the electron velocity map image of three-dimensionally aligned naphthalene molecules with their MPA parallel to the y-axis. A less pronounced four-fold structure as in fig 6.12 c) is visible. Aligning the molecules one-dimensionally with their MPA parallel to the y-axis, fig 6.12 f), results in a distribution that resembles the unaligned case, fig 6.12 a).

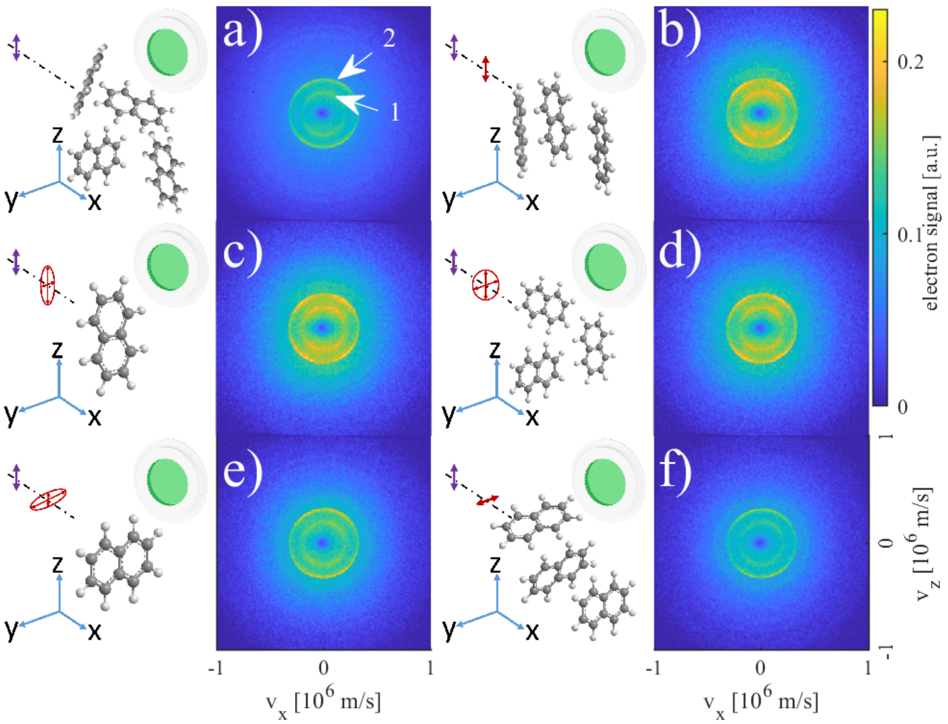

Figure 6.12: Two-dimensional velocity images of electrons produced when the probe pulse (293.53 nm) ionizes the naphthalene molecules. The wavelength of the probe pulse is set to excite the $\bar{8}^1\bar{7}^1 8^1$ vibrational state in the S_1 electronic state.

The photoelectron kinetic energy spectra, obtained through Abel inversion, for the unaligned (blue) and one-dimensionally aligned with the MPA parallel to z-axis (red), are shown in fig 6.13. Both spectra exhibit two prominent peaks, centred at 0.13 eV and 0.32 eV, see fits (purple and yellow curve). The most pronounced peak centred at 0.32 eV is readily assigned to the origin. Besides the prominent peaks, there are five (six) small peaks in the photoelectron kinetic energy spectrum of the unaligned (aligned) naphthalene molecules (dash-dotted arrows).

The measurement of a photoelectron kinetic energy spectrum of a [1+1]-photoionization via the S_1 $\bar{8}^1\bar{7}^1 8^1$ vibrational mode has to the best of my knowledge not been reported before. As such, I could not assign the peaks through a comparison to previous measurements as done in chapter 6.3.2. Thus, I calculated possible candidates for the resulting cation vibration as a sum of the individual vibrational modes (eq 6.4), combining the cation vibrational modes $\bar{8}^+$, $\bar{7}^+$, 8^+ and 7^+:

$$\nu_{nm} = \nu_n + \nu_m \tag{6.4}$$

As a result of this calculation, the peak centred at 0.13 eV can be assigned to a convolution of the $\bar{8}^+8^+$, $\bar{8}^+7^+$, and $\bar{8}^+\bar{7}^+$ vibrational modes of the cation (corresponding calculated photoelectron kinetic energy 0.12 eV, 0.12 eV, and 0.14 eV respectively). Furthermore, the five small peaks (dash-dotted arrows) can be assigned with the same method. The lowest kinetic energy peak, centred at 0.03 eV can be assigned to the $\bar{8}^+7^+8^+$ (calc 0.03 eV). The next peak, centred at 0.04 eV, is assigned to the $\bar{8}^+\bar{7}^+8^+$ (calc 0.05 eV) vibrational mode. The peak centred at 0.07 eV can be assigned to the $\bar{8}_2{}^+7^+$ mode. Higher in energy than the first most prominent peak, another small peak, centred at 0.18 eV, can be found. It is assigned to the 7^+ vibrational mode (calc 0.17 eV). The energetically highest small peak is found at 0.25 eV and can be assigned to the $\bar{8}^+$ vibrational mode (calc 0.25 eV). Upon aligning the molecules another peak appears, labelled A, centred at 0.58 eV, which might originate from a [1+1'+1]-photoionization process, see discussion in section 6.2.

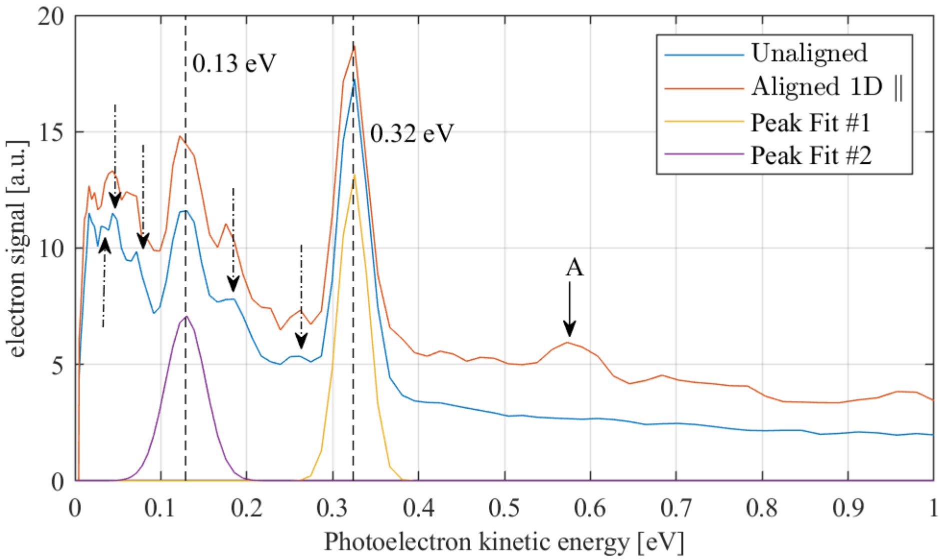

Figure 6.13: Photoelectron kinetic energy distribution obtained through Abel inversion from the electron velocity map images in fig 6.12 a) and b) 1D-aligned (MPA ∥ z-axis). PES of unaligned naphthalene molecules - blue, PES of aligned naphthalene molecules - red. The three channels are fitted with gaussians. The arrows mark smaller maxima, for assignment see text. A - channel ascribed to a [1+1'+1]-photoionization. Probe wavelength: 293.53 nm

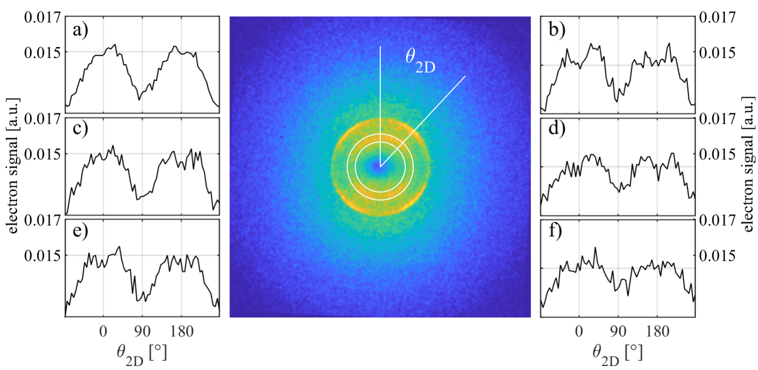

Figure 6.14: Angular distribution of the first channel, centre image: 1D ∥ aligned with radial range. The alignment geometries used in the different subfigures are the same as in fig 6.12, i.e. a) unaligned, b) 1D aligned MPA ∥ z-axis, c) 3D aligned MPA ∥ z-axis, d) 1D aligned least polarizable axis ∥ x-axis, e) 3D aligned MPA ∥ y-axis, f) 1D aligned MPA ∥ y-axis.

The angular distribution of the first channel, labelled 1 in fig 6.12, a convolution of the $\bar{8}^+8^+$, $\bar{8}^+7^+$ and $\bar{8}^+\bar{7}^+$ vibrational modes, is shown in fig 6.14. The angular distribution of the unaligned molecules, fig 6.14 a), shows an anisotropy with enhanced emission along the z-axis, 0° and 180° and a clear suppression at 90° and 270°. Upon aligning the molecules one-dimensionally with their MPA parallel to the z-axis, fig 6.14 b), a suppression along the z-axis, 0° and 180°, can be observed. Three-dimensional alignment of naphthalene molecules with their MPA parallel to the z-axis, fig 6.14 c), results in a distribution without a suppression parallel to the z-axis. The angular distribution of the molecules with their least polarizable axis aligned parallel to the x-axis, shows a slight suppression along the z-axis, 0° and 180°, with less suppression at 90° and 270° than in the unaligned case, fig 6.14 a). With three-dimensional alignment (MPA parallel to y-axis), fig 6.14 e), the suppression at 90° and 270° becomes more pronounced again. Compared to the unaligned distribution, fig 6.14 a), the maxima look flattened. This can be interpreted as a slight suppression along 0° and 180°. Aligning the molecules one-dimensionally with their MPA parallel to the y-axis, fig 6.14 f), results in a rather isotropic distribution. However, a slight suppression at 90° and a more pronounced suppression suppression at 270° can be observed. They are, however, not as pronounced as in the angular distribution of the unaligned case, fig 6.14 a). Since this channel is, as previously argued, most likely a combination of three different vibrational modes of the cation, their preferred ejection angles and directions of suppressed emission are also convoluted. Therefore, one or more of the channels might show a clear suppression at 0° and 180°, while another channel does not. Thus, the signal from the latter channel lessens the suppression of the former.

The angular distribution of the second channel, labelled 2 in fig 6.12, the origin, is shown in fig 6.15. The distribution of the unaligned naphthalene molecules, fig 6.15 a), exhibits a clear suppression of emission at 90° and 270°. Furthermore, there is a minor suppression at 0° and 180°. Between -90° and 0° a detector inefficiency leads to a smaller signal. Aligning the molecules one-dimensionally with their MPA parallel to the z-axis, fig 6.15 b), shows a clear suppression at 0° and 180° and stronger suppressions at 90° and 270°. The suppression parallel to the z-axis gets enhanced upon three-dimensional alignment with the MPA parallel to the z-axis, fig 6.15 c). When the molecules are three-dimensionally aligned with their MPA parallel to the y-axis, fig 6.15 e), the suppressions at 0° and 180°, and 90° and 270°, appear fairly identical. On the other hand, aligning the molecules with their least polarizable axis parallel to the x-axis, fig 6.15 d), leads to a distribution with only a faint reminder of a suppression at 0° and 180° in the form of two flattened peaks. However, the suppression at 0° and 180° is missing. This indicates that two different nodal planes are causing the suppressions in fig 6.15 c) and e), three-dimensional alignment with the MPA parallel to the z-axis and the y-axis, respectively. Aligning the molecules one-dimensionally, with their MPA parallel to the y-axis, fig 6.15 f), demonstrates a distribution similar to the distribution in fig 6.15 d). This indicates that the suppression in fig 6.15 e) is caused by a nodal plane. In fig 6.15 f) this nodal plane is rotated and the suppression is blurred. Thus, the nodal plane includes the molecule's most polarizable axis and its least polarizable axis.

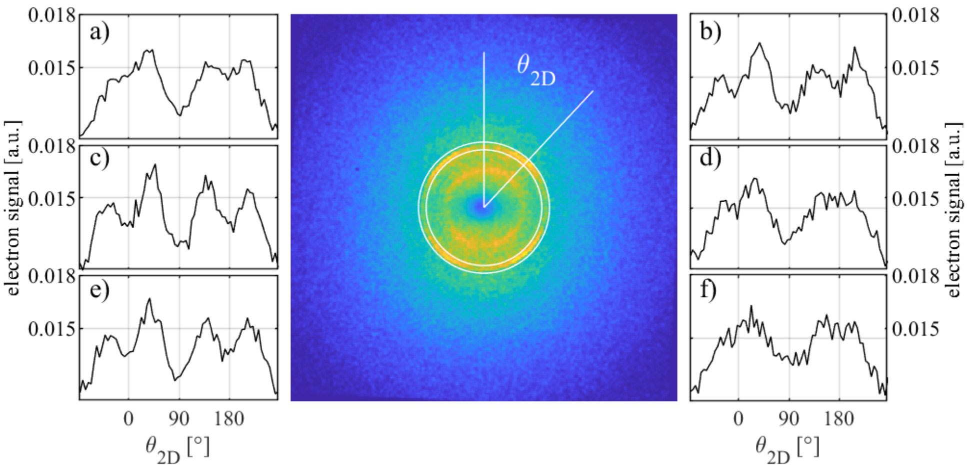

Figure 6.15: Angular distribution of the second channel, centre image: 1D ∥ aligned with radial range. The alignment geometries used in the different subfigures are the same as in fig 6.12, i.e. a) unaligned, b) 1D aligned MPA ∥ z-axis, c) 3D aligned MPA ∥ z-axis, d) 1D aligned least polarizable axis ∥ x-axis, e) 3D aligned MPA ∥ y-axis, f) 1D aligned MPA ∥ y-axis.

The PADs of unaligned and one-dimensionally (MPA parallel to the z-axis) aligned molecules, fig 6.12 a) and b), have been Abel inverted and the betas have been extracted for a fit. Figure 6.16 a) reproduces the electron kinetic energy distribution of fig 6.13. The areas for the weighted beta calculation have been marked in grey and numbered. Two to three channels are visible. The less energetic ones are the channels marked with 1 and 2 in fig 6.16 a). As the channel, centred at 0.58 eV only appears when the molecules are aligned, it has not been analysed further. The Abel inverted images of the unaligned molecules are shown in fig 6.16 b). An anisotropy with a favoured emission along the z-axis is visible in both channels. The high-energetic channel is an artefact, originating from the detector edge. The Abel inverted image of the one-dimensionally (MPA parallel to the z-axis) aligned molecules is shown in fig 6.16 c). The two channels now exhibit a suppression along the z-axis. The artefact, stemming from the detector edge is also visible. Both Abel inverted images are on the same scale.

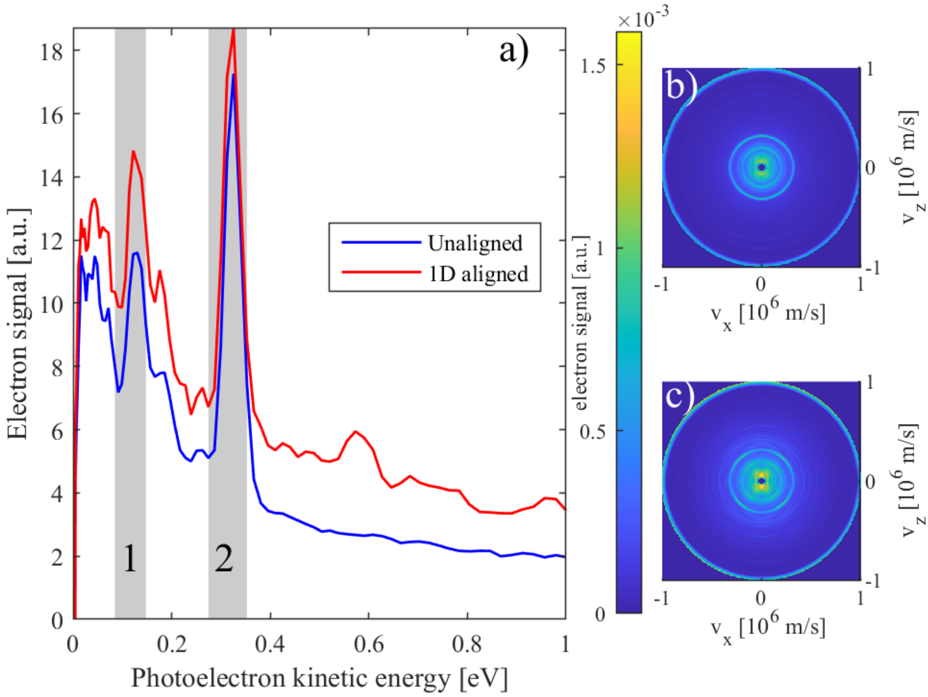

Figure 6.16: a) [1+1]-Photoionization photoelectron kinetic spectrum of aligned and unaligned naphthalene molecules, probe wavelength set to $\bar{8}^1\bar{7}^1 8^1$ vibrational state of the S_1 (293.53 nm), grey areas (1-2) used for β-calculation. b) Abel inverted image of the unaligned molecules. c) Abel inverted image of the molecules aligned 1D, MPA $\parallel$ to the z-axis

The angular distribution of the Abel inverted images is shown in fig 6.17. The upper row shows the angular distribution from the unaligned molecules, the lower row the angular distribution from the one-dimensionally aligned molecules. The data from the Abel inversion is marked with circles. The fit is shown as a solid red line. For the first channel of the unaligned molecules, fig 6.17 a1), an anisotropy peaking at 0° and 180° with clear suppression at 90° and 270° can be observed. Upon aligning the molecules one-dimensionally with their MPA parallel to the z-axis, fig 6.17 b1), the signal level increases. Furthermore, a suppression at 0° and 180° besides the more pronounced supression at 90° and

270° can be observed. The angular distribution of the second channel, the origin, is shown in fig 6.17 a2) and b2). With the unaligned molecules, fig 6.17 a2), a clear suppression at 90° and 270° is visible again. The data points indicate a more pronounced suppression at 0° and 180° than is captured by the fit. Nevertheless, both, the data points and the fit, exhibit a suppression at 0° and 180°. However, the distribution changes dramatically, when the molecules are aligned one-dimensionally with their MPA parallel to the z-axis, fig 6.17 b2). The curve shows four maxima, peaking at -45°, 45°, 135°, and 225°. The former suppression at 0° and 180°, fig 6.17 a2), is now insignificantly less than the suppression at 90° and 270°.

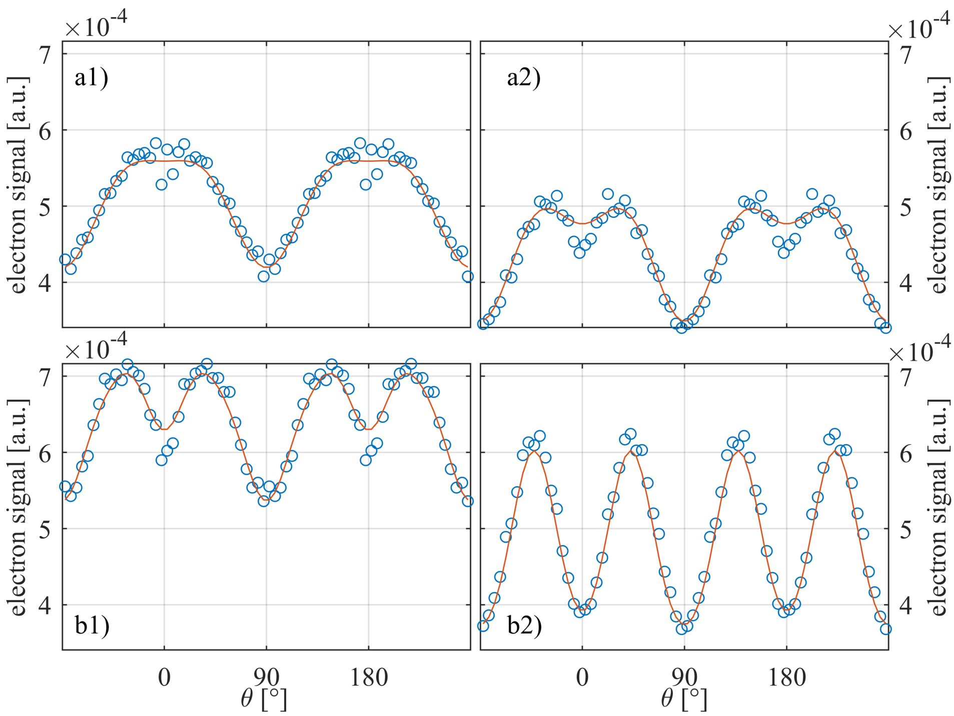

Figure 6.17: Angular distributions from the $\bar{8}^1\bar{7}^1 8^1$ transition of naphthalene, Data from Abel inversion (circles) and fit through betas (solid line) for the two channels: 1) first channel, 2) second channel. The upper panel a) shows the distribution from unaligned molecules, the lower panel b) the distribution from one-dimensionally aligned molecules (MPA ∥ z-axis)

6.3.4 3^1 vibrational mode

The vibrational mode 3 of the S_1 has been addressed at 33454 cm^{-1} (S_1 32019cm^{-1} + 1435 cm^{-1} [122]; 298.9 nm, 4.15 eV). Furthermore, the resulting photoelectron kinetic energies can be expected to be low. To nevertheless obtain a good signal level, the probe pulse peak intensity was set considerably high, 0.74 TW cm^{-2}, while the alignment pulse peak intensity was kept at 0.58 TW cm^{-2}.

Figure 6.18 shows the resulting PADs. The PAD of unaligned naphthalene molecules is shown in fig 6.18 a). The signal has been doubled for better visibility. Two channels, labelled 1 and 2, are observed. Due to the high probe intensity a significant multiphoton background (energies bigger than channel 2 can also be observed. Both channels exhibit a preferred emission of photoelectrons along the z-axis. Upon aligning the molecules one-dimensionally with their MPA parallel to the z-axis, fig 6.18 b), these two channels become overshadowed by the channel appearing at a photoelectron kinetic energy of 0.58 eV. Its possible origin is discussed in sections 6.2 and 6.3.2. This new channel also exhibits a preferred emission of photoelectrons along the z-axis. A suppression straight in the direction of the z-axis as previously observed for other vibrational modes, see sections 6.3.2 and 6.3.3, is missing. Three-dimensional alignment with the molecule's MPA parallel to the z-axis, fig 6.18 c), does not show any significant changes to the one-dimensional alignment PAD. Aligning the naphthalene molecules with their least polarizable axis parallel to the x-axis, fig 6.18 d) leads to less signal in the previously overshadowing channel of 0.58 eV, revealing a rather isotropic distribution in the channels labelled 1 and 2. Figure 6.18 e) shows the PAD obtained from molecules three-dimensionally aligned with their MPA parallel to the y-axis. The signal levels are lower than in fig 6.18 d) and the overall distribution looks more isotropic. This is even more the case for the one-dimensionally aligned molecules with their MPA parallel to the y-axis, fig 6.18 f). The electron yield decreases, while the PAD looks isotropic.

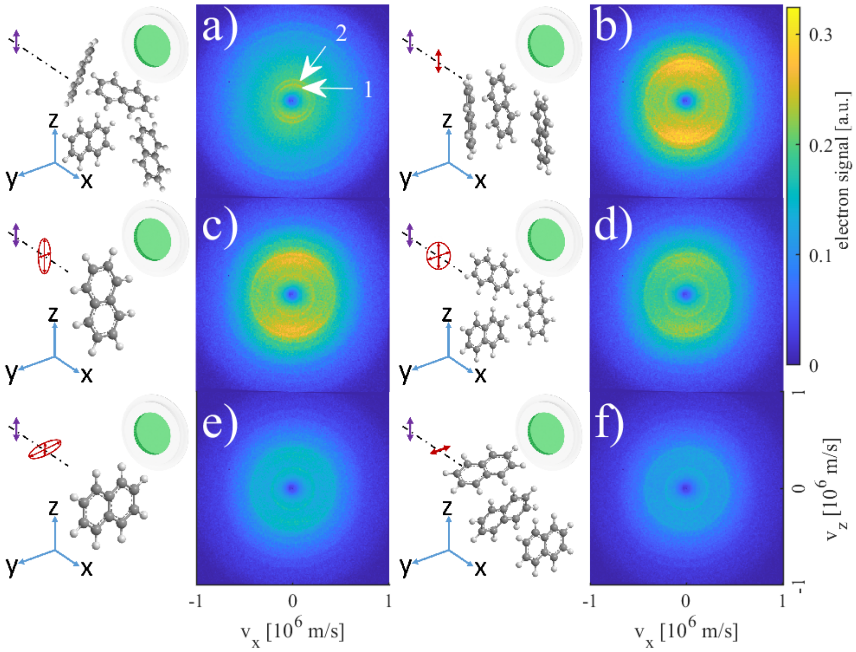

Figure 6.18: Two-dimensional velocity images of electrons produced when the probe pulse (298.92 nm) ionizes the naphthalene molecules. The wavelength of the probe pulse is set to excite the 3^1 transition vibrational state in the S_1 electronic state.

The photoelectron kinetic energy distribution is shown in fig 6.19. The distribution obtained from one-dimensionally aligned naphthalene molecules is given in red, from unaligned molecules in blue. The photoelectron kinetic energy distribution of the unaligned molecules shows two peaks, while the distribution of aligned molecules exhibits three. The two peaks in the unaligned distribution and the three peaks in the aligned distribution have been fitted (green, yellow and purple). The peak at 0.15 eV is readily assigned to the origin. The peak at 0.09 eV can be assigned to a variety of the cation's vibrational modes. It fits the vibrational modes 9 and $\bar{8}$ after ref [121], and modes $\bar{6}$ or $\bar{7}$ after ref [122]. Cockett et al. also lists the b_{1u} 3 vibrational mode at 423 cm^{-1} [122], corresponding to a kinetic energy of 0.10 eV. However, the excited vibrational mode in the S_1 state is of a_g character and the corresponding vibrational mode of same character in the cation is not to be reached by the absorption of two photons (IP 65665 cm^{-1} + vibrational mode 1436 cm^{-1} = 67101 cm^{-1} vs. 2*33454 cm^{-1} = 66908 cm^{-1}). The third peak (0.58 eV), only visible in the aligned distribution is assigned to a [1+1'+1]-photoionization process, involving the S_2-state (calculated 0.53 eV). Another peak at 0.05 eV indicated by a double-headed arrow, could not be assigned and could also be an artefact from the Abel inversion.

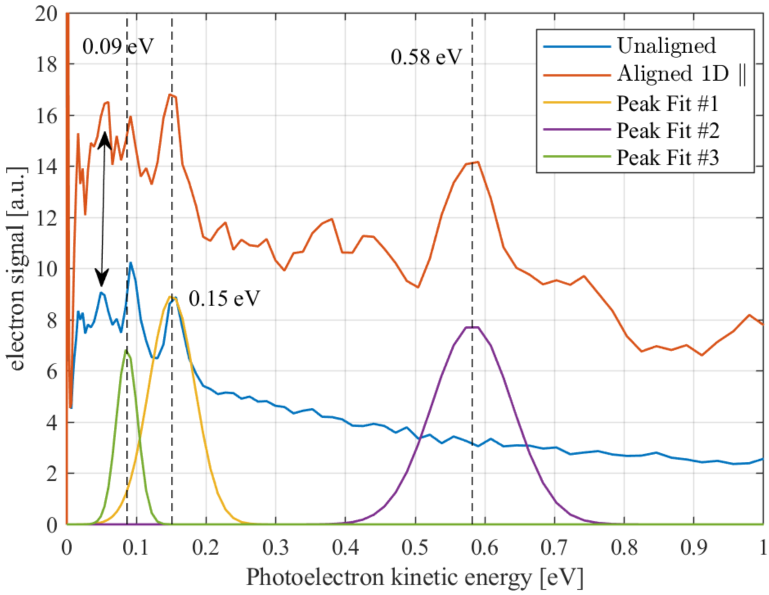

Figure 6.19: Photoelectron kinetic energy distribution obtained through Abel inversion from the electron velocity map images in fig fig 6.18 a) and b) 1D-aligned (MPA || z-axis). PES of unaligned naphthalene molecules - blue, PES of aligned naphthalene molecules - red. The two channels are fitted with gaussians. The channel ascribed to a [1+1'+1]-photoionization is also fitted (purple curve). Double-headed arrow: peak that could not be assigned and could also be an artefact from the Abel inversion. Probe wavelength: 298.92 nm

The angular distributions of the channel, labelled 1 in fig 6.18, is shown in fig 6.20. The angular distribution of the unaligned molecules is shown in fig 6.20 a). It shows a twofold-structure with a favoured emission along the z-axis, 0° and 180°. Upon aligning the molecules with their MPA parallel to the z-axis, fig 6.20 b), the distribution does not change significantly. The suppression at 90° and 270° is slightly less than for the unaligned case. When the molecules are three-dimensionally aligned with their MPA parallel to the z-axis, fig 6.20 c), the suppression becomes less. Confining the least polarizable axis parallel to the x-axis, fig 6.20 d), and three-dimensionally aligning the molecules with their MPA parallel to the y-axis, gives a very similar distribution. With one-dimensional alignment, MPA parallel to the y-axis, the suppression at 90° and 270° decreases further.

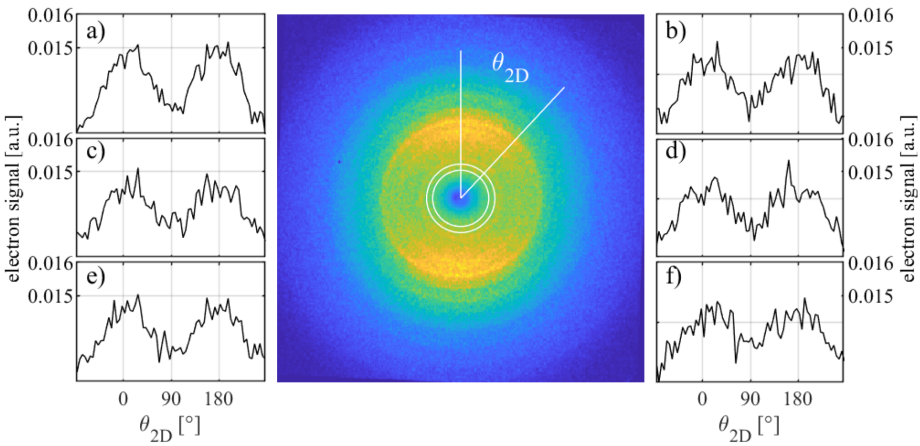

Figure 6.20: Angular distribution of the first channel, centre image: 1D ∥ aligned with radial range. The alignment geometries used in the different subfigures are the same as in fig 6.18, i.e. a) unaligned, b) 1D aligned MPA ∥ z-axis, c) 3D aligned MPA ∥ z-axis, d) 1D aligned least polarizable axis ∥ x-axis, e) 3D aligned MPA ∥ y-axis, f) 1D aligned MPA ∥ y-axis.

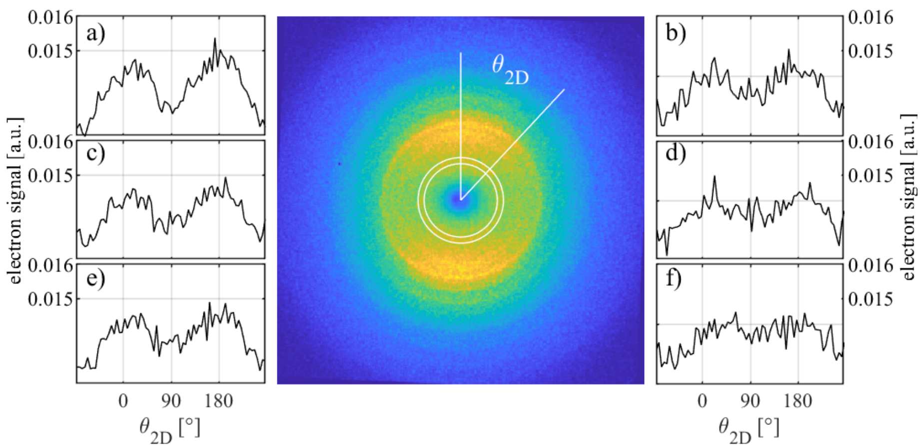

Figure 6.21: Angular distribution of the second channel, centre image: 1D ∥ aligned with radial range. The alignment geometries used in the different subfigures are the same as in fig 6.18, i.e. a) unaligned, b) 1D aligned MPA ∥ z-axis, c) 3D aligned MPA ∥ z-axis, d) 1D aligned least polarizable axis ∥ x-axis, e) 3D aligned MPA ∥ y-axis, f) 1D aligned MPA ∥ y-axis.

Figure 6.21 shows the angular distributions of channel 2 in fig 6.18. The angular distribution of the unaligned molecules, fig 6.21 a), again shows a two-fold structure with a favoured emission along the z-axis (0° and 180°). Upon aligning the molecules one-dimensionally, fig 6.21 b), the suppression at 90° and 270° decreases. Aligning the molecules three-dimensionally with the MPA either parallel to the z-axis, fig 6.21 b), or parallel to the y-axis fig 6.21 e), results in a similar distribution. The least confinement is visible in fig 6.21 d) and e), i.e. aligning the molecules with their least polarizable axis parallel to the x-axis or aligning them one-dimensionally with their MPA parallel to the y-axis. This decline in remarkable features with the angular distributions of the aligned molecules is unexpected. Consulting fig 6.18 delivers a possible explanation for this phenomenon. The aligned electron velocity map images also have a third channel, centred at 0.58 eV. This channel is rather prominent and is likely to overshadow less energetic channels. As the unaligned electron velocity map image does not feature this third channel, the second channel therein cannot be affected by it. Thus, the angular distribution with the most significant structures is the one from unaligned molecules as the angular distributions from aligned molecules suffer from overshadowing effects. At this considerably high probe intensities, it is also possible, that three-photon photoionization processes take place, depleting the two-photon channel. The resulting photoelectron kinetic energy 4.3 eV is out of the detector range (3 eV).

The extra channel appearing upon alignment, centred at a photoelectron kinetic energy of 0.58 eV, has also been analysed in terms of its angular distribution, see fig 6.22. The channel is not existing in the unaligned electron velocity map image, see fig 6.18 a). As such, this angular distribution shows the multiphoton background of the unaligned distribution. It is rather isotropic with a slight increase of photoelectron emission at 0° and 180°, fig 6.22 a). Aligning the molecules introduces the channel attributed to a [1+1'+1]-photoionization process involving the S_2-symmetry at 0.58 eV photoelectron kinetic energy (calculated: 0.45 eV). When the molecules are one-dimensionally aligned with their MPA parallel to the z-axis, the angular distribution shows a clear preferred emission along the z-axis, peaking at 0° and 180°, fig 6.22 b). The maxima surpass the maxima of the multiphoton background in the unaligned angular distribution. Aligning the naphthalene molecules three-dimensionally with their MPA parallel to z-axis, fig 6.22 c) increases the confinement of the maxima. Figure 6.22 d) shows the angular distribution of the naphthalene molecules with their least polarizable axis confined parallel to the x-axis. The angular distribution strongly resembles the angular distribution of the multiphoton background in fig 6.22 a). However, the signal levels are slightly higher. With three-dimensional alignment, MPA parallel to the y-axis, fig 6.22 e), the two-fold structure with maxima at

0° and 180° reappears. The peaks are almost of the same confinement as in the three-dimensionally case with the MPA parallel to the z-axis. However, the suppression at 90° and 270° in fig 6.22 e) is not as strong as in fig 6.22 c) and the maxima are 0° and 180° are marginally smaller. Aligning the molecules one-dimensionally with their MPA parallel to the y-axis, fig 6.22 f), results in a rather isotropic distribution, with less signal between 270° and 0° than in the other four quadrants. This indicates a detector inefficiency in this area.

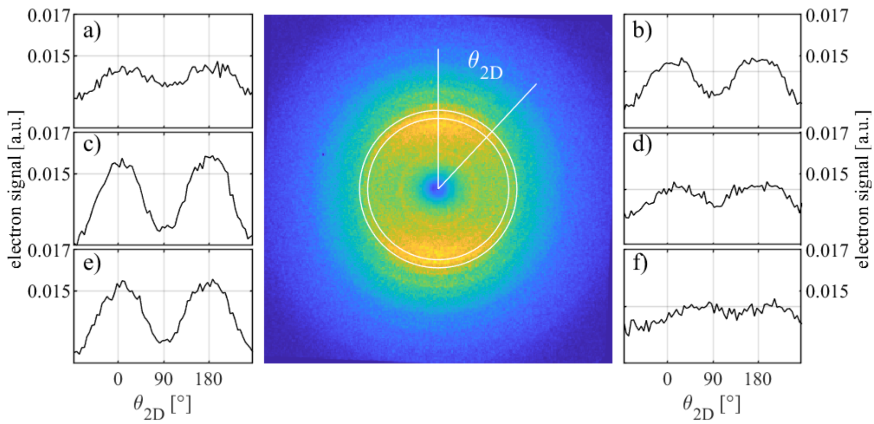

Figure 6.22: Angular distribution of the third channel, centre image: 1D ∥ aligned with radial range. The alignment geometries used in the different subfigures are the same as in fig 6.18, i.e. a) unaligned, b) 1D aligned MPA ∥ z-axis, c) 3D aligned MPA ∥ z-axis, d) 1D aligned least polarizable axis ∥ x-axis, e) 3D aligned MPA ∥ y-axis, f) 1D aligned MPA ∥ y-axis.

Figure 6.23 a) shows the photoelectron kinetic energy distribution obtained via Abel inversion, as shown in fig 6.19. The grey areas mark the range used for the weighted anisotropy parameter calculation, which are used for the fitted data in fig 6.24. Both curves show two or three peaks respectively. The first peak, labelled 1, is centred at 0.09 eV and could not be unambigiously assigned, see discussion of fig 6.19. The second peak, labelled 2, centred at 0.15 eV stems from the origin. The third channel only appears when the molecules are aligned and is tentatively assigned to a [1+1'+1]-photoionization process, see discussion in section 6.2. Figures 6.23 b) and c) show the Abel inverted electron velocity map image of the unaligned PAD, or the one-dimensionally aligned (MPA parallel to the z-axis), respectively. Both Abel inverted images are on the same scale. The Abel inverted electron velocity map image of the unaligned shows the two channels and an inversion artefact from the detector edge. Both channels exhibit a favoured emission along the z-axis. Upon aligning the molecules one-dimensionally, the new channel with a photoelectron kinetic energy of 0.58 eV appears. Since the onion-peeling algorithm, see section 4.2, removes the overshadowing effects partly, the other two channels are better visible than in the raw electron velocity map images. They also show a favoured emission along the z-axis, which appears more confined than in the unaligned Abel inverted electron velocity map image.

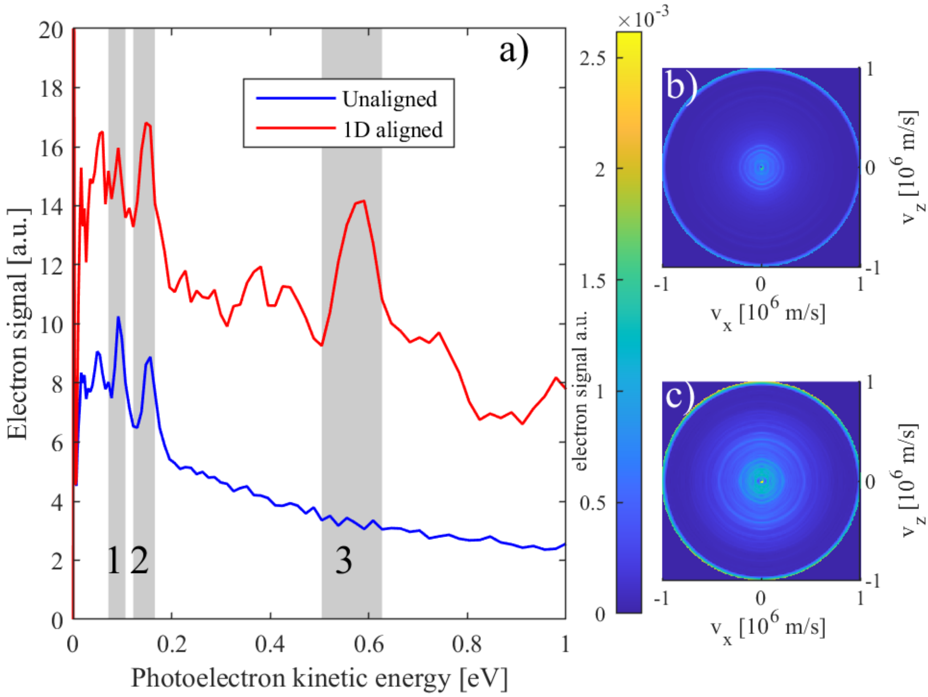

Figure 6.23: a) [1+1]-Photoionization photoelectron kinetic spectrum of aligned and unaligned naphthalene molecules, probe wavelength set to 3^1 vibrational state of the S_1 (298.92 nm), grey areas (1-3) used for β-calculation. b) Abel inverted image of the unaligned molecules. c) Abel inverted image of the molecules aligned 1D, MPA ∥ to the z-axis

Figure 6.24 shows the angular distributions obtained from the Abel inverted electron velocity map image (circles) and a fit with weighted anisotropy parameters (solid red curve). The upper row, a1)-a3) shows the distributions from the unaligned case, following the numbering in fig 6.23. The lower row, b1)-b3), shows the distributions from the one-dimensionally aligned molecules. The distribution of the first channel from the unaligned molecules, fig 6.24 a1), shows a two-fold structure peaking parallel to the z-axis at 0° and 180°. Upon alignment, fig 6.24 b1), these two peaks are still present. However, they also exhibit a small suppression at 0° and 180°. This could not be noticed in the raw electron velocity map images. The angular distribution of the second channel obtained from the unaligned molecules, fig 6.24 a2), also exhibits a two-fold structure as the first channel with maxima at 0° and 180°. However, the two maxima are not as pronounced as in the first channel. Aligning the molecules, fig 6.24 b2), leads to a rather isotropic distribution in the data (circles). The maxima at 0° and 180° are just slightly higher than the signal levels at the suppression 90° and 270°. The fit also exhibits a two-fold structure peaking at 0° and 180°, with a slight suppression at the maxima at 0° and 180°. The multiphoton background in the unaligned distribution is almost perfectly isotropic, fig 6.24 a3). Aligning the molecules introduces the third peak above the background level, peaking at 0° and 180°, fig 6.24 b3).

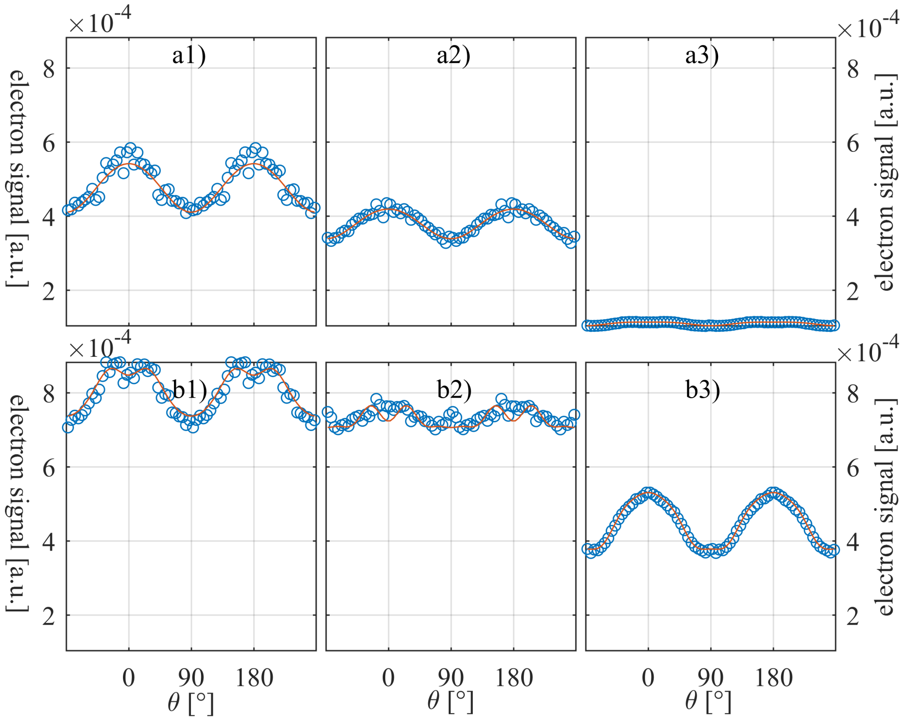

Figure 6.24: Angular distributions from the 3^1 transition of naphthalene, raw data (circles) and Abel inverted (solid line); for the three channels: first channel a), second channel b), and third channel c). The upper pannel 1) shows the distribution from unaligned molecules, the lower pannel 2) the distribution from one-dimensionally aligned molecules (MPA || z-axis)

6.4 Conclusion and discussion

In this chapter, I presented photoelectron angular distributions obtained from resonant [1+1]-photoionization of naphthalene molecules in gas phase. The resonances used were the vibrational states $\bar{8}^1 7^1 8^1$, $\bar{8}^1 \bar{7}^1 8^1$ and 3^1 of the S_1-state at 34142 cm^{-1} (292.9 nm, 4.23 eV), 34068 cm^{-1} (293.53 nm, 4.22 eV) and 33454 cm^{-1} (298.9 nm, 4.15 eV).

I want to highlight especially the four-fold structure obtained in the origin channel appearing for a resonant photoionization via the $\bar{8}^1 \bar{7}^1 8^1$ and the $8^1 \bar{7}^1 8^1$ vibrational mode of the S_1-state. When the molecules are unaligned the origin channel shows a two-fold structure with a preferred ejection of photoelectrons along the polarization of the probe pulse (z-axis). When the molecules are aligned one-dimensionally or three-dimensionally the PADs reveal a four-fold structure with an enhanced electron signal at -45°, 45°, 135° and 225° relative to the z-axis. This four-fould structure becomes most pronounced for the $\bar{8}^1\bar{7}^1 8^1$ vibrational mode of the S_1-state.

The photoelectron kinetic energy distributions of all three vibrational modes have revealed multiphoton effects. The probe intensities were increased significantly compared to the aniline experiments because the electron signal obtained was weaker. For a comparison, the signal levels of aniline even with intensities around 0.06 $\mathrm{TW\,cm^{-2}}$ was as high as the signal obtained from naphthalene with intensities of 0.6 $\mathrm{TW\,cm^{-2}}$. Each of the presented measurements have been acquired over several hours. However, with longer acquisition times and less probe pulse intensity the multiphoton effects could have been avoided.

Furthermore, each electron velocity map image demonstrated that alignment pulse photons also get absorbed. This could be avoided by using a one-photon ionization process. This experiment can be conducted once the VUV light source is connected to the experimental setup and operational.

CHAPTER 7

Molecules embedded in helium droplets

As mentioned previously, in order to access the molecular frame and obtain MF-PADs from laser aligned molecules a high degree of alignment ($\langle\cos^2\theta\rangle > 0.9$) is necessary [48]. Adiabatic alignment, see section 2.2.2, is a good candidate to achieve such high degrees of alignment for a variety of molecules. The disadvantage of adiabatic alignment is that the highest degree of alignment is realized at the peak of the alignment pulse. As seen in the chapters 5 and 6 this can be problematic. Once the aniline and naphthalene molecules are in an electronically excited state, they can also absorb photons from the alignment pulse. This leads to rivalling ionization channels, see sections 5.2 and 6.2, perturbing the intended investigation of a [1+1]-photoionization process. The truncated alignment pulse leaves a short window for field-free alignment, yet it is too short to use a spectrally narrow probe pulse with a pulse duration of 6 ps.

Recently, it was shown that adiabatic alignment of molecules in helium nanodroplets using truncated alignment pulses can provide a time window of 5-15 ps of high degrees of alignment after the truncation edge of the pulse [43]. The laser intensity after truncation is reduced by 2-3 orders of magnitude.

The high degree of alignment under almost field-free conditions render this technique highly interesting for investigating MFPADs. On the other hand, the expected disadvantage of this method is that the photoelectrons will be scattered on their way out of the droplet. One major goal of my PhD project was to explore if this method can be used to obtain MFPADs from molecules embedded in helium nanodroplets. In this chapter, I present the experimental results I managed to record towards the end of my project.

7.1 Aniline molecules in helium nanodroplets

This section is dedicated to the study of aniline molecules embedded in helium nanodroplets. The droplet beam was formed as described in section 2.1.1. Inside the pickup chamber, see section 3.1.3, the vapour pressure of aniline was controlled by the leak valve connected to the sample holder and adjusted such that the droplets were doped with at most one molecule. The doped droplets afterwards travel to the target chamber, where the droplet beam was crossed by the same laser beams (IR - alignment and UV - probe) as used in the experiments on the gas phase molecules.

At first the ionization yield as a function of the frequency of the UV laser pulse was recorded to scan out the origin resonance in the two-photon ionization process. In practice, this was achieved by recording the number of electrons as a function of the wavelengths of the probe pulse. The laser wavelength was varied by adjusting and recording the KDP crystal position, see also section 3.2 for the UV probe pulse generation. The data has been normalized to the intensity by subtracting a two-photon ionization spectrum of the rest gas inside the target chamber. This way, also signal by background electrons is removed. The results are shown in fig 7.1. The curve follows roughly a Gaussian distribution with a maximum at 34200 cm^{-1} and a FWHM of approx. 400 cm^{-1}. This means the origin resonance is blue-shifted by 170 cm^{-1} compared to the gas phase value of 34031 cm^{-1} [102].

Loginov et al. conducted a similar experiment over a broader wavelength range, see fig 7.2 [125]. They also employed a [1+1]-photoionization using UV-light and found the origin-resonance to be blue-shifted by roughly 100 cm^{-1} [125]. The energy shift in fig 7.1 is therefore in good agreement with previous experiments. The sharp zero phonon line (onset blue-shifted by 35 cm^{-1} to the gas phase origin) visible in fig 7.2 is missing in fig 7.1. This might be caused by the difference in observable. In the spectrum in fig 7.1 electrons were detected, while Loginov et al. observed the ion signal instead. Another explanation might be the unfavourable signal-to-noise-ratio, which is addressed in more detail in the next paragraph.

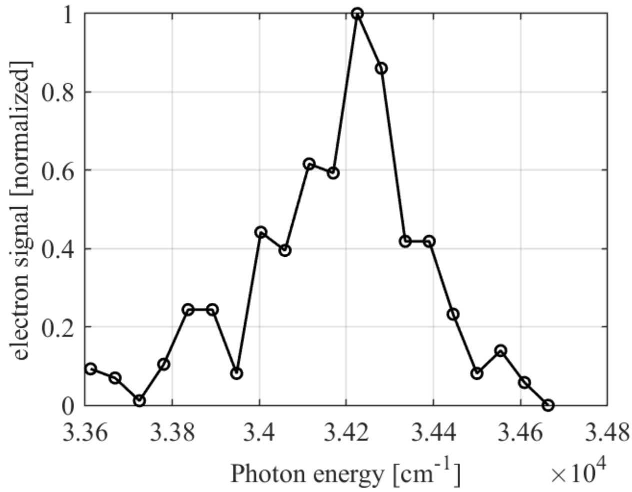

Figure 7.1: R2PI spectrum of aniline molecules embedded in 12 K helium droplets

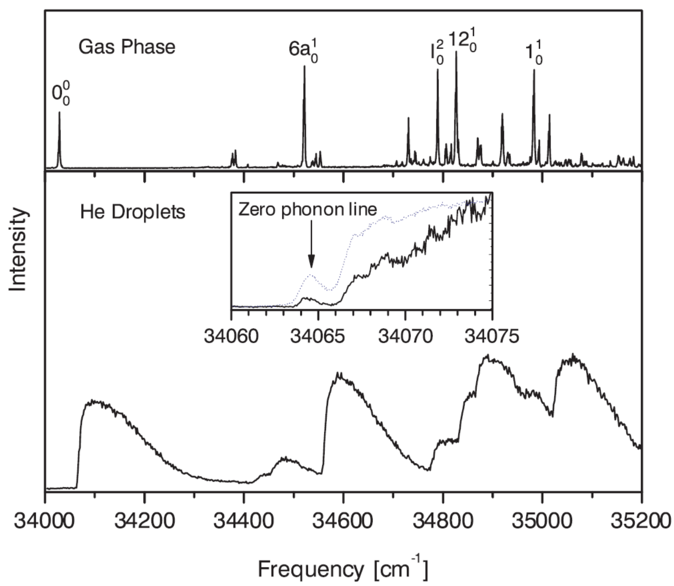

Figure 7.2: $S_1 \leftarrow S_0$ excitation spectrum of aniline. Upper subfigure: gas phase, lower subfigure: in helium droplets. Inset: Zoom on the zero phonon line at smaller wavenumbers than the band origin with different light intensities, solid line –7 MW cm^{-2}, dotted line 150 GW cm^{-2}, figure adopted from [125]

In order to record electron velocity map images, the probe pulse was set to the maximum seen in the R2PI spectrum 34200 cm^{-1} (292.4 nm, 4.24 eV). The probe pulse intensity was smaller than 0.3 $TW\,cm^{-2}$. Figure 7.3 a) shows the electron velocity map image obtained, when only the probe pulse linearly polarized parallel to the z-axis is employed. The image is essentially circularly symmetric with an excess of signal in the inner part. Under the conditions of the experiment, a significant parts of the electrons originate from ionization of gas phase aniline molecules, i.e. molecules that are not captured inside a droplet and diffuse from the pickup cell to the laser interaction region. In fact, the signal rate was 0.11 electrons per frame (1 frame: 10 laser shots) with the helium droplets and 0.10 electrons per frame when the droplets are blocked. Once the molecules are aligned the signal rate rises to 0.14 electrons electrons per frame. To eliminate the signal from this effusive background, an image with the helium droplet beam blocked was recorded, see fig 7.3 b) and subtracted it from the image with the helium droplets. The difference image is shown in fig 7.3 c). It also exhibits an excess signal in the centre.

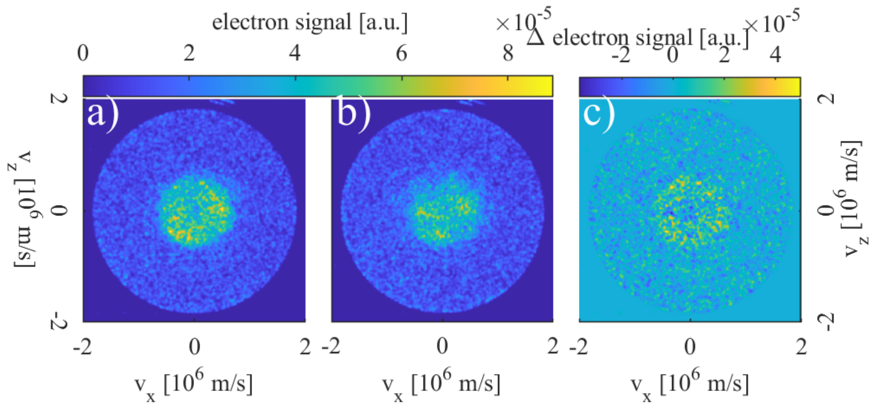

Figure 7.3: a) Electron velocity map image from unaligned aniline molecules in helium droplets b) Signal from effusive molecules c) difference image. Probe wavelength: 292.4 nm with an intensity smaller than 0.3 $TW\,cm^{-2}$, the alignment pulse was excluded

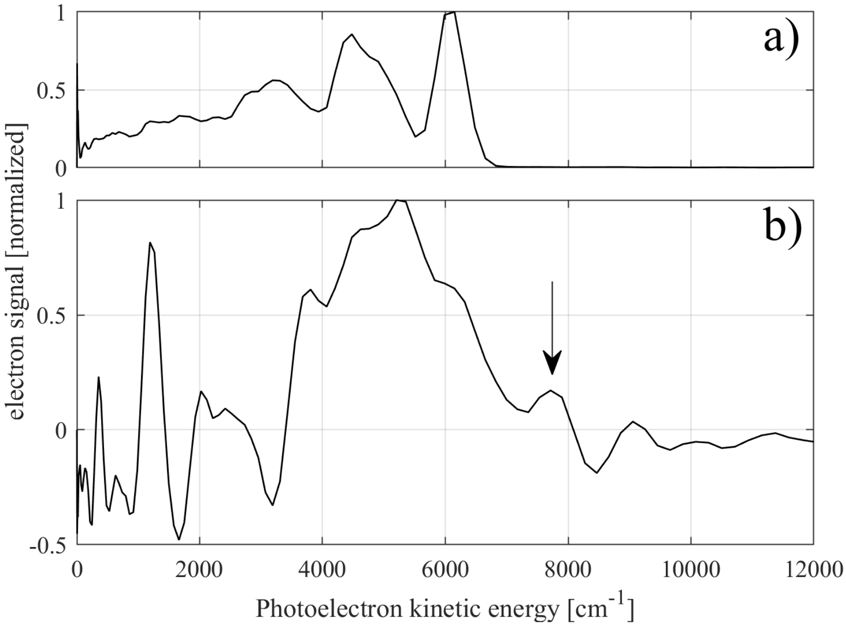

Figure 7.4: a) PES from gas phase aniline molecules. Probe wavelength 293.85 nm, intensity 0.06 TW cm^{-2}. b) PES of aniline molecules embedded in helium nanodroplets, 292.4 nm with an intensity smaller than 0.3 TW cm^{-2}

From both images, the electron velocity map image of the unaligned molecules in helium nanodroplets as well as of the effusive molecules, the kinetic energy distribution has been extracted via Abel inversion as described in section 4.2. The difference between the two kinetic energy distributions is shown in fig 7.4 b). The photoelectron kinetic energy distribution peaks at 5200 cm^{-1} (0.65 eV). As a reference, the gas phase photoelectron kinetic energy distribution is shown in fig 7.4 a). The gas phase origin is found at 6150 cm^{-1} (0.76 eV). The comparison indicates that the photoelectrons from ionization of the molecules inside the helium nanodroplets have about the same kinetic energy as the electrons from ionization of the isolated molecules. Although, the peak is significantly broadened.

These observations are rather consistent with the results of Loginov et al., see fig 7.5. They also found a broad peak centred at roughly 5000 cm^{-1} (0.62 eV). They found the origin to be blue-shifted to ~6500 cm^{-1} (0.8 eV). Comparing the photoelectron kinetic energy distribution in fig 7.4 b) with the results of Loginov et al., this might indicate the peak marked with an arrow in fig 7.4

stems from the origin. As it is centred at 7700 cm^{-1} (0.95 eV), this would be a rather large blue-shift.

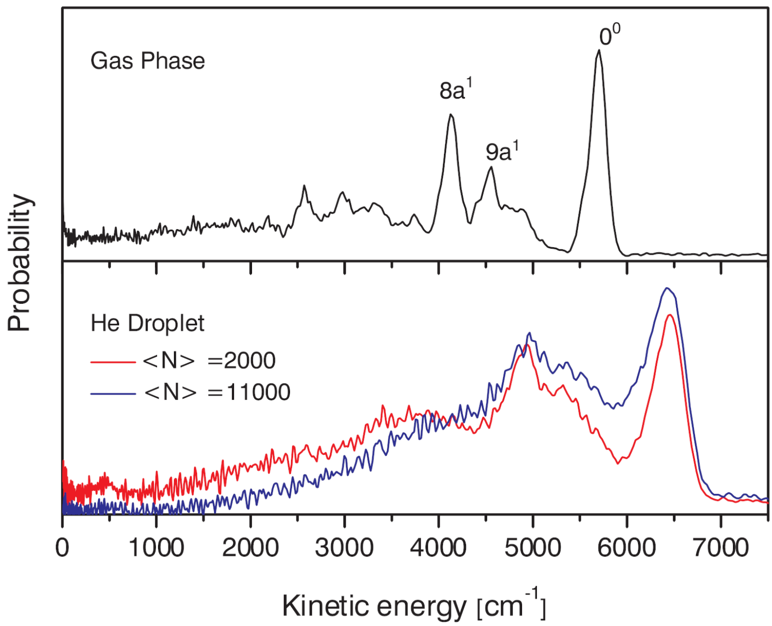

Figure 7.5: [1+1] PES of aniline via the origin of the $S_1 \leftarrow S_0$ transition. Upper subfigure: in gas phase, lower subfigure embedded in helium droplets (size 2000-11000 helium atoms). Figure adopted from [125]

Three different experiments with aniline have been conducted. The molecules have been aligned three- and one-dimensionally. For the one-dimensionally aligned case, they have been probed with the alignment pulse present, and after the truncation edge. The timing of the truncation edge is defined as the time when the intensity has fallen to half its value. Figure 7.6 shows the intensity profile of the alignment pulse and the two times (-24.7 ps and 7 ps) when the probe pulse is send, marked by two vertical dash-dotted lines. At these times the probe pulse realizes its peak intensity. The inset of fig 7.6 shows that at 7 ps the alignment pulse intensity has fallen to 1 % of its peak intensity. The molecules have been aligned with an intensity of 1.1 TW cm^{-2}.

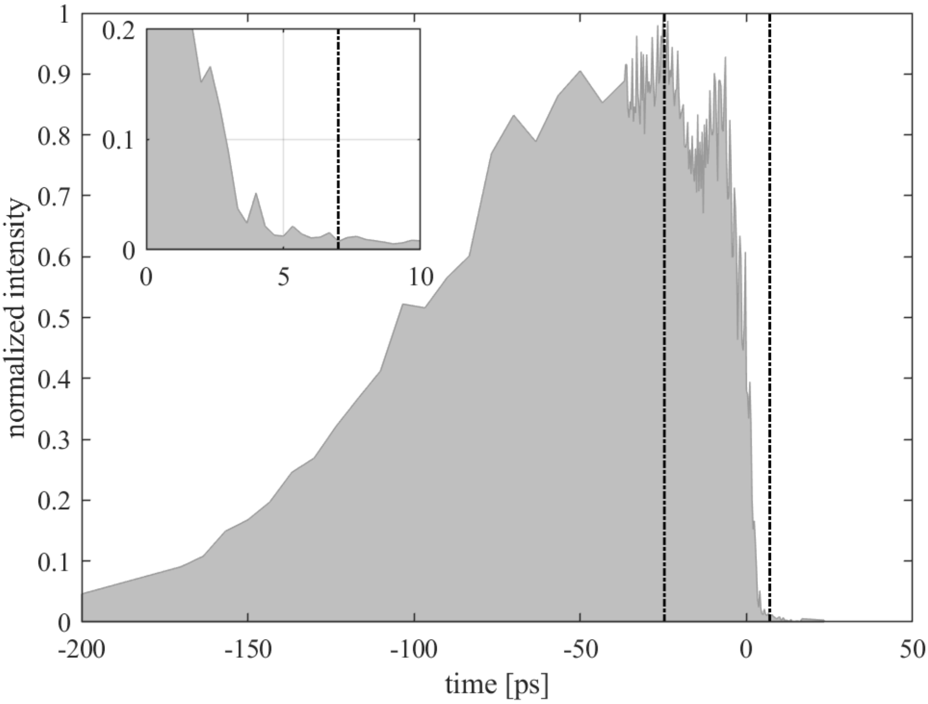

Figure 7.6: Intensity profile of the alignment pulse. The vertical dash-dotted lines mark the timings used for the probe pulse, i.e. at the peak of the alignment pulse (-24.7 ps) and after the truncation edge (7 ps). Inset: Zoom on the 0 to 10 ps range.

The experimental outcome also depends on the droplet sizes. Therefore, different droplet sizes have been investigated to find the optimal droplet size. The optimum is depending on two factors. In order to achieve the highest electron signal the electrons need to be scattered the least possible - for both the photoelectron angular distributions as well as their kinetic energy. Consequently, a small droplet size would be favourable as this introduces less helium atoms as scattering centres. Smaller droplet sizes also have a smaller pickup cross section for the molecules, so the doping pressure needs to be increased. Hence more effusive signal accompanies the droplets and the signal-to-noise ratio decreases. The droplets size was found to be optimal at approx. $3 \cdot 10^3 - 10^4$ atoms, 5 – 10 nm (14 K, 25 bar).

In a first experiment, the aniline molecules inside the droplets were aligned three-dimensionally with their MPA parallel to the y-axis, i.e the MPA perpendicular to the detector screen. The highest signal levels were obtained in this configuration in the gas phase experiments. Since molecules can be aligned field-free inside a helium droplet, see chapter 2.2.4, the molecules have been probed 7 ps after the truncation edge, see fig 7.6. The resulting electron velocity map images are shown in fig 7.7. The subfigures a), b) and d) are normalized and on the same scale. Figure 7.7 a) shows the electron velocity map image from the aligned molecules inside the helium nanodroplets. The image is essentially circularly symmetric, with an excess of signal in the inner part up to a photoelectron kinetic energy of roughly 0.8 eV. This circle is also present in fig 7.7 b), which shows the electron velocity map image obtained from the effusive molecules. However, the edge is less confined than in fig 7.7 a). The difference between the electron velocity map image from aniline molecules inside the helium nanodroplets and the electron velocity map image of the effusive molecules is shown in fig 7.7 c). The circle of excess signal up to 0.8 eV gets enhanced in this representation. However, it does not reveal any anisotropy. Nevertheless, it can readily be seen that the signal levels are higher for aligned, fig 7.7 a), than for the effusive molecules, fig 7.7 b), as both images are on the same scale. The electron velocity map image of unaligned aniline molecules inside helium nanodroplets is shown in fig 7.7 d). Comparing fig 7.7 a) and fig 7.7 d), it is evident that the signal level in the electron velocity map image from the aligned molecules inside the helium droplets are higher than the signal level from unaligned aniline molecules inside the droplets. This implies that the molecules are indeed aligned – 7 ps after the truncation edge, when the alignment pulse has only 1 % of its intensity. This is an indication that almost field-free alignment inside the droplets has indeed been achieved.

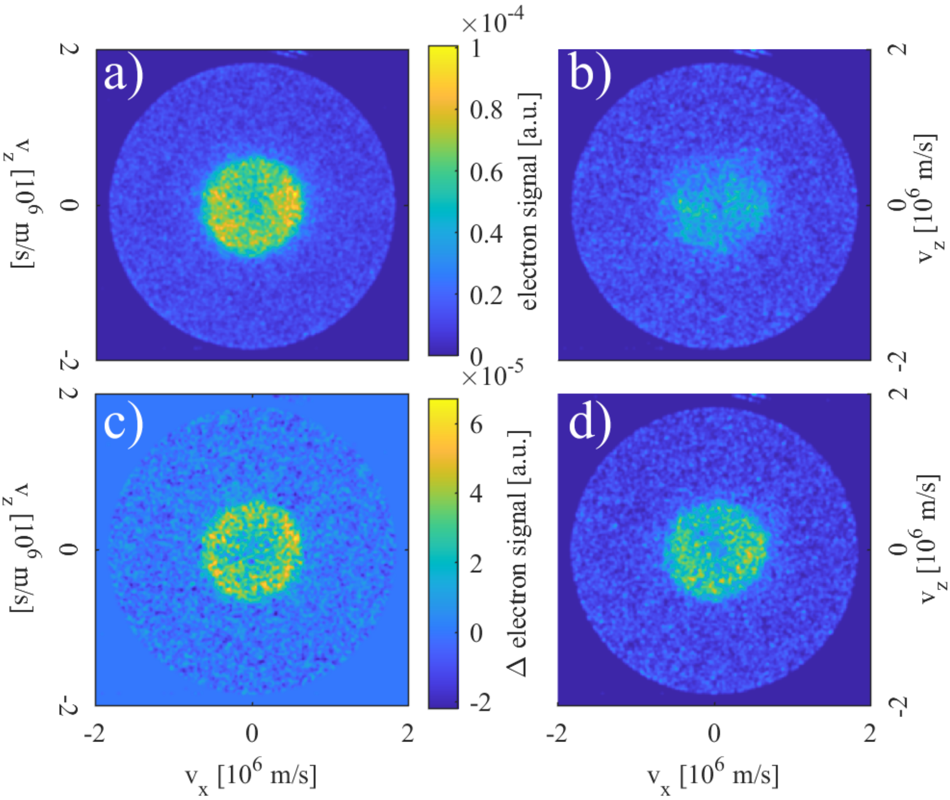

Figure 7.7: Aniline in helium droplets, alignment MPA 3D ⊥ to the y-axis, probed 7 ps after the truncation edge; a) Electron velocity map image from aligned aniline molecules inside the droplets, b) Electron velocity map image of effusive molecules, c) Difference signal between the aligned molecules inside helium nanondroplets and effusive molecules d) Electron velocity map image from unaligned molecules inside helium droplets

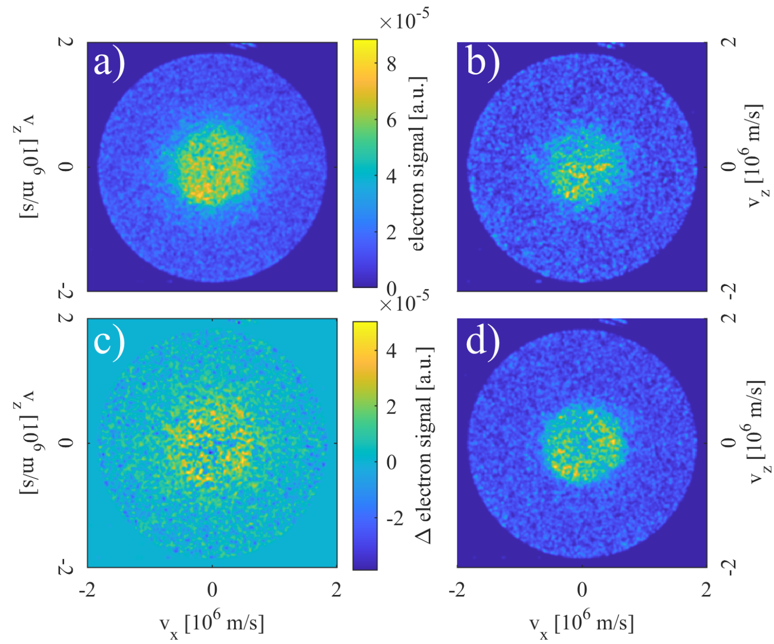

Figure 7.8: Aniline in helium droplets, alignment MPA 1D ∥ to the z-axis, probe and alignment pulse overlap in time; a) Electron velocity map image from aniline inside the droplets, b) Electron velocity map image of effusive molecules, c) Difference signal between the aligned molecules inside helium nanondroplets and effusive molecules d) Electron velocity map image from unaligned molecules inside helium droplets

In the gas phase experiments, the most angular confinement was seen for one- and three-dimensional alignment with the MPA parallel to the z-axis. One-dimensional alignment was chosen over three-dimensional alignment since it is also allowing for Abel inversion. Figure 7.8 a) shows the electron velocity map image obtained from one-dimensionally aligned molecules inside helium droplets. The molecules have been probed while the alignment pulse was still present applying the same conditions as in the gas phase experiment, i.e. t=-24.7 ps, see fig 7.6. Compared to fig 7.7 a), the circle in 7.8 a) is less confined. Furthermore, comparing the electron velocity map image of aligned aniline molecules inside helium droplets, fig 7.8 a), with the electron velocity map image obtained from unaligned aniline inside helium droplets, fig 7.8 d), the confinement of the circle in the latter is more pronounced. This indicates that further channels are appearing because photons from the alignment pulse are being absorbed, similar to what was observed in the gas phase. The electron velocity map image of the effusive molecules is shown in fig 7.8 b). It also shows an excess of signal at the centre. The difference between the aligned molecules inside the helium droplets and effusive molecules, fig 7.8 c), shows an angular isotropic distribution with some excess signal in the centre. However, the edge of this excess signal is not as confined as it was in fig 7.7 c). This also indicates that new ionization channels are appearing, because of alignment photons being absorbed as seen in the gas phase experiments.

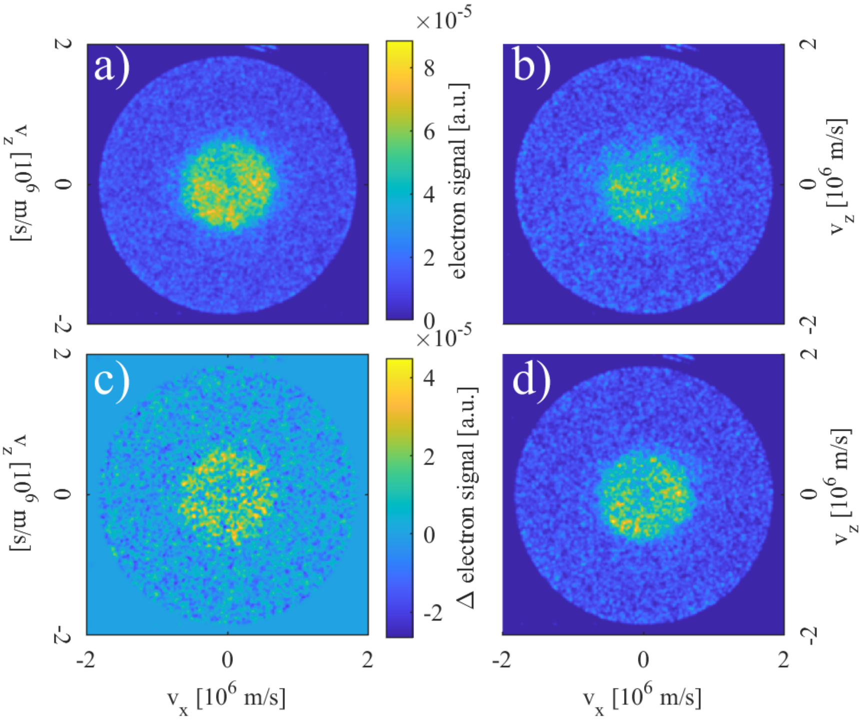

Figure 7.9: Aniline in helium droplets, alignment MPA 1D ∥ to the z-axis, 7 ps after the truncation edge; a) Electron velocity map image from aniline inside the droplets, b) Electron velocity map image of effusive molecules, c) Difference signal between the aligned molecules inside helium nanondroplets and effusive molecules d) Electron velocity map image from unaligned molecules inside helium droplets

The aniline molecules in fig 7.9 have also been one-dimensionally aligned with their MPA parallel to the z-axis. As in fig 7.7, they have been probed 7 ps after the truncation edge of the alignment pulse. Any angular anisotropies visible in the images a), b) and d) are alike and are due to detector inhomogeneities. Figure 7.9 a) shows the electron velocity map image of the aligned aniline molecules inside the helium nanodroplets. Comparing fig 7.9 a) with fig 7.8 a), the circle of the excess signal appears more confined again. This supports the previous observation of potential higher energetic electrons due to the absorption of alignment photons. The electron velocity map image of the effusive signal is shown in fig 7.9 b). It exhibits less signal than fig 7.9 a). The difference image between the aligned molecules and the effusive molecules, fig 7.9 c), is angular isotropic. The electron velocity map image of unaligned aniline molecules inside helium nanodroplets is shown in fig 7.9 d). The signal levels are less than in fig 7.9 a), which indicates, the molecules in fig 7.9 a) are in fact aligned quasi field-free.

Figure 7.10 a) shows the photoelectron kinetic energy of aniline molecules embedded in helium droplet and the effusive signal. As a reference the photoelectron kinetic energy distribution of the gas phase molecules was added as a grey area.

The photoelectron kinetic energy distribution of the unaligned molecules is shown as a black curve. It exhibits a broad peak centred at 0.65 eV, which could be interpreted as a convolution of the separate gas phase peaks.

The photoelectron kinetic energy distribution of the aligned aniline probed with the field of the alignment pulse present is given in red as a solid line. The respective photoelectron kinetic energy distribution of the effusive molecules is shown also in red as a dashed line. Starting at 0.4 eV, the signal from the aligned molecules surpasses the signal from the effusive background. The curve shows a broad peak centred at 0.65 eV. Furthermore the additional peaks, appearing upon alignment in the gas phase (any peak with an energy greater than 0.8 eV), might be there as well. The signal of the aligned distribution above 0.8 eV exceeds the signal of the effusive background.

The electron signal of aligned aniline molecules probed 7 ps after the truncation edge of the alignment pulse is given as a solid blue line and the effusive as a dashed blue line, respectively. There is a broad peak also centred at 0.65 eV in the electron signal of the aligned molecules surpassing the signal of the effusive molecules. Above 0.8 eV, the electron signal from the aligned molecules probed 7 ps after the truncation edge and the effusive are of the same level and below the level of the aligned molecules probed while the field of the alignment pulse is still present. Furthermore, the peak at 0.65 eV is slightly decreased in the red curve compared with the blue curve. This also indicates the absorption of alignment pulse photons, when the alignment pulse is still present.

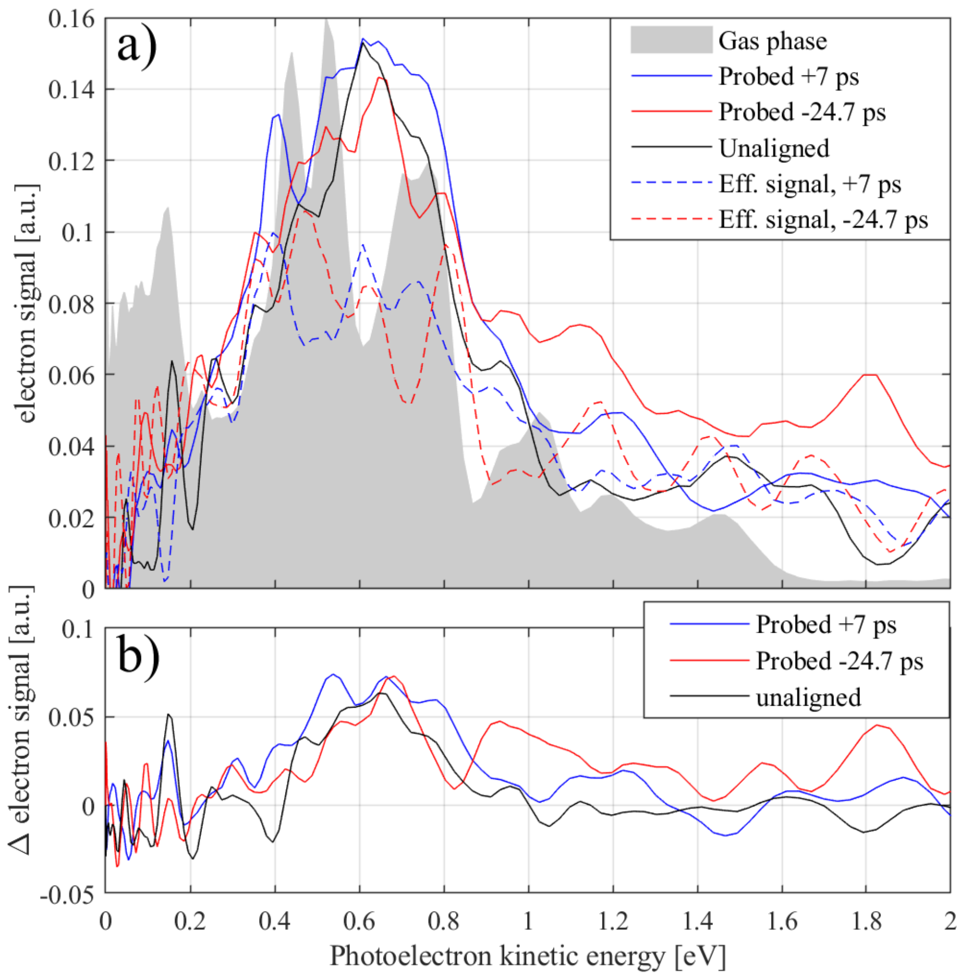

Figure 7.10: a) PES of one-dimensionally unaligned aniline molecules embedded in helium nanodroplets (black), and aligned molecules inside the droplets, probed temporally overlapping with the alignment pulse (red) and 7 ps after the truncation edge (blue) with the distributions of their respective effusive signal, with gas phase PES (grey area) for comparison, b) Difference between the electron signal from molecules inside the helium droplets and the effusive molecules

Figure 7.10 b) shows the difference signal between the molecules inside the droplets and the effusive signal. All three curves exhibit the maximum at 0.65 eV. The maximum seems to be slightly higher in terms of signal levels with the molecules probed 7 ps after the truncation edge of the alignment pulse (blue). With the effusive subtracted, the distribution of the unaligned molecules (black) and the aligned molecules probed with the field of the alignment pulse still present (red) seem to match better than in fig 7.10 a). Above 0.8 eV the distribution of the molecules probed 7 ps after the truncation edge of the alignment pulse follows the unaligned molecules. The signal of the molecules probed with the field of the alignment pulse still present, slightly exceeds the signal of the other two curves.

7.2 Conclusion and discussion

As stated in the introduction of this chapter, the goal of the presented experiment was to evaluate whether the truncated pulses can be used to achieve almost field-free alignment inside helium nanodroplets and obtain MFPADs from aligned molecules embedded in helium nanodroplets.

In the course of this investigation, aniline molecules embedded in helium nanodroplets have been aligned three-dimensionally with their MPA parallel to the y-axis and probed 7 ps after the truncation edge of the alignment pulse. They showed an enhanced signal circularly symmetric ending at approx. 0.8 eV compared to the electron velocity map images of unaligned aniline molecules. Furthermore, the electron velocity map images of aniline aligned one-dimensionally with their MPA parallel to the z-axis and probed 7 ps after the truncation edge of the alignment pulse look rather similar, exhibiting the same circularly symmetric shape of enhanced signal. These results indicate that an almost field-free alignment of aniline molecules inside the helium droplets has been achieved.

Moreover, the aniline molecules aligned one-dimensionally with their MPA parallel to the z-axis and probed while the field of the alignment pulse is still present show indications that alignment photons are absorbed in this case and perturb the measurement. This is consistent with the gas phase experiments. This renders the truncated pulses employed to align molecules almost field-free inside helium nanodroplets highly desirable.

On the other hand, any angular anisotropies in the resulting electron velocity map images were missing in all three cases. One explanation might be that the photoelectron kinetic energy was too small to preserve any angular preference throughout the scattering at the helium atoms. This could be tested with a different species that has a lower ionization potential.

A huge problem with the conducted experiment is the detrimental signal-to-noise ratio. With the aligned molecules only 0.14 electrons per frame were achieved, while 0.10 electrons per frame stem from effusive molecules. This might be caused by the nature of the probe focus. With a wavelength of 292.4 nm and a beam waist of 20 µm, the confocal length is 8.6 mm. The helium droplet beam width is defined by the skimmer in the coldtrap chamber to about 2 mm. Thus, not just the effusive molecules very close to the helium droplet beam, but also the effusive molecules that are present up to 3 mm in distance to the helium droplet beam can be ionized.

A decrease of the effusive molecules accompanying the beam or an increase of the signal from the droplets is thus highly desirable. The helium droplet instrument in the presented experiments did probably not run optimally. Further testing in the last months by Adam Chatterley and Lorenz Kranabetter, in close dialogue and collaboration with myself, revealed that e.g. the nozzle had a scuff mark near the orifice. This mark was not remarkable enough to influence the flow or the pressure, but might nevertheless have lessened the quality of droplet beam. Furthermore, the mounts for the doping cells have been mounted off-centre and crooked by the manufacturer as mentioned in sectin 3.1.3. The doping cell could be mounted nevertheless. A HeNe laser beam was introduced at a window in the target chamber (see section 3.1.5, fig 3.7 A) to align the cell and the laser beam was not clipped, indicating that the droplet beam would not be hindered either. On the other hand, it was a tight fit. This deficit has now been eliminated by replacing the doping cell and its mount with a more flexible doping cell and doping cell mount.

With these improvements, it would be most interesting to repeat the experiments with the optimized helium droplet setup. At present, the results are inconclusive.

CHAPTER 8

Conclusion and outlook

The focus of my PhD work was to explore MFPADs. In pursuit of that goal, I collaboratively built a new vacuum setup. This new setup has been proven to perform better than the former experimental setup. However, in conducting the experiments, possibilities for improvement have been discovered, which are currently being addressed. The new experimental setup has been used to record PADs from laser-aligned molecules in gas phase and in helium droplets via resonant [1+1]-photoionization. Three of the conducted experiments are presented in this thesis and the following three sections are summarizing them and give an outlook for future experiments.

As mentioned in the beginning, the overall goal of my PhD project was to investigate MFPADs resulting from ionization of molecules due to absorption of a single VUV photon. Unfortunately, it became impossible for me to reach this goal due to the extensive number of problems with the central femtosecond laser system and the resulting delay of the VUV source and beamline.

Nevertheless, I still consider this objective extremely interesting and the perhaps most important outlook based on my thesis work. One of the intriguing aspects of ionizing aligned molecules with a single photon and recording the MFPADS is the possibility of imaging the orbitals. In previous experiments in Femtolab, it has been shown that MFPADs created by multiphoton ionization of gas-phase molecules such as benzonitrile, carbonylsulfide [61] and naphthalene [62] with strong near-infrared laser pulses contain direct information about the nodal structure of the orbitals from which electrons are removed. The disadvantage of the strong laser field is that it distorts the inherent electron distribution [64]. This effect should be eliminated by replacing the strong-field ionization with the weak VUV pulses. I think it would be extremely interesting to conduct such experiments. Unlike the two-photon ionization scheme used in the current work, the single-photon mechanism does not involve electronically excited states. Therefore, I do not think that the presence of the alignment field will disturb the ionization process. Thus, adiabatic alignment can be used throughout these experiments. This ensures that very high degrees of alignment can be achieved, including both one-dimensional and three-dimensional alignment for a variety of different molecules.

8.1 Resonant two-photon photoionization of aniline molecules in gas phase

Aniline molecules in gas phase have been aligned using truncated alignment pulses and electron velocity map images using resonant [1+1]-photoionization have been recorded. The addressed resonances were the 0^0, 1^1 and the $6a^1$ vibrational mode of the electronically excited S_1-state.

The channel that could be assigned to leaving the cation in the ground state exhibited an anisotropy with an excess of signal perpendicular to the probe pulse polarization, when the molecules were unaligned. This was the case for all three resonances used, i.e. the 0^0, 1^1 and the $6a^1$ vibrational mode of the electronically excited S_1-state. Once the molecules were aligned three-dimensionally with the MPA parallel to the z-axis the angular distributions showed the most pronounced maxima at 0° and 180°. Besides aligning the molecules, the alignment pulse had further effects on the molecule. Photons of the alignment pulse have been absorbed and this caused new ionization channels. Furthermore, the energies of the respective channels shifted. This could be avoided in a one-photon experiment. The VUV source is tunable from 147 nm (8.44 eV) to 179 nm (6.97 eV) and the ionization potential of aniline is 7.72 eV [102]. Thus, it is possible to ionize aniline molecules with the VUV laser beam.

In section 5.3.3 possible MFPADs corresponding to the recorded PADs have been identified through a simulation of possible electron velocity map images and comparing their anisotropy parameters with the experimentally obtained ones. In order to approach the MFPAD further with the recorded PADs, the molecular frame needs to be coincide better with the laboratory frame. Accordingly, higher degrees of alignment would be favourable. However, the polarizability anisotropy of aniline is unfavourable for high degrees of alignment. Thus, higher alignment intensities are needed to align aniline molecules tightly. In turn, the higher intensities also increase the amount of photons absorbed from the alignment pulse. This can be avoided, if the molecules are aligned field-free inside a helium droplet, also using a truncated alignment pulse.

The theoretical calculation would also become more comparable with the experiment for a one-photon experiment. For the present experiment, the absorption of the first photon, exciting the molecule from the electronic ground state S_0 to the first electronically excited state S_1 is neglected. In a one-photon experiment, the initial state to consider, the S_0-state, would match the experimental ground state. Furthermore, since the VUV light source is tunable, different photoelectron kinetic energies ranging from 0 eV to 0.72 eV could be realized and the respective MFPADs can be compared to investigate possible shape resonances.

8.2 Resonant two-photon photoionization of naphthalene molecules in gas phase

Naphthalene molecules in gas phase have been aligned using truncated alignment pulses and electron velocity map images using resonant [1+1]-photoionization have been recorded. The addressed resonances were the $\bar{8}^1 7^1 8^1$, $\bar{8}^1 \bar{7}^1 8^1$ and 3^1 vibrational modes of the S_1-state.

When the molecules are unaligned the channel that can be attributed to leaving the cation in the vibrational ground state, shows a two-fold structure with a preferred ejection of photoelectrons along the polarization of the probe pulse (z-axis). When the molecules are aligned one-dimensionally or three-dimensionally the PADs reveal a four-fold structure. This four-fold structure obtained in the origin channel appearing for a resonant photoionization of one-dimensionally aligned naphthalene molecules (MPA $\parallel$ z-axis) via the $\bar{8}^1 \bar{7}^1 8^1$ vibrational mode of the S_1-state was most remarkable.

The photoelectron kinetic energy distributions of all three vibrational modes have revealed multiphoton effects. With longer acquisition times and less probe pulse intensity these multiphoton effects could have been avoided. Furthermore, these distributions showed that photons of the alignment pulse also get absorbed. As mentioned in the previous section, this could be avoided in a one-photon ionization experiment.

8.3 Resonant two-photon photoionization of aniline molecules in helium droplets

The main goal of this experiment was to evaluate whether truncated pulses enable to achieve field-free alignment inside helium nanodroplets and obtain MFPADs from the dopant species. The results are hitherto inconclusive. An increase in the signal upon alignment indicated, that the molecules were indeed aligned. Any angular anisotropy in the recorded PADs was missing.

The expected photoelectron kinetic energy was about 0.8 eV. This might have been too small to preserve any angular preference after scattering through the helium shell. As such, higher photoelectron kinetic energies are favourable. A different species with a lower ionization potential could be used. Furthermore, this molecule could be probed with the VUV source. Anthracene (IP 7.43 eV) and tetracene (IP 6.97 eV) are possible candidates for such a study [126, 127]. With these molecules and a probe wavelength of 147 nm, photoelectron kinetic energies of 1 eV and 1.47 eV could be realized –before possible scattering effects with the helium atoms of the droplets. These molecules have already been employed in another setup in femtolab with different probe wavelengths. In order to achieve a sufficient doping of the helium droplets, both species needed to be heated to increase the vapour pressure. With the present manufacturing errors, it was not possible to include the oven in the new experimental setup to do so. With the new, more flexible doping cell mount, this becomes possible. I believe it is most intriguing to conduct such an experiment using the VUV source and a species with a low ionization potential that will allow for higher photoelectron kinetic energies.

Another problem that I faced with the experiment was a detrimental signal-to-noise ratio. With the aligned molecules only 0.14 electrons per frame were achieved, while 0.10 electrons per frame stem from effusive molecules. The alteration of the doping cell and its mount could also improve this ratio. Thus it would already be most interesting, to repeat the presented experiment with the optimized new setup.

Looking further ahead, it would also be interesting to conduct time-resolved experiments using the VUV pulse as the probe pulse and record MFPADs. Obvious cases are dynamics in electronically excited states leading to e.g. isomerization. Since the presence of the alignment pulse can perturb the electronically excited states as shown especially with my studies of aniline, employing field-free aligned molecules is highly advisable. As mentioned before, this (almost) field-free alignment can be achieved for molecules solvated in helium nanodroplets for a time window of 10 ps or more. Therefore, I consider it highly relevant to continue and extend the studies I initiated here. However, it remains to explore, if valuable information from PADs stemming from ionization of aligned molecules in helium droplets can be extracted due to the scattering of the electron at the helium atoms. I believe it will be useful to study cases where the electron energies are several eV rather than a fraction of an eV, which was mainly the case in my preliminary studies on aniline molecules.

Bibliography

[1] K. L. Reid. Photoelectron Angular Distributions. *Annual Review of Physical Chemistry*, 54(1):397–424, 2003.

[2] K. L. Reid. Photoelectron angular distributions: developments in applications to isolated molecular systems. *Molecular Physics*, 110(3):131–147, 2012.

[3] F. Kelkensberg, A. Rouzée, W. Siu, G. Gademann, P. Johnsson, M. Lucchini, R. R. Lucchese, and M. J. J. Vrakking. XUV ionization of aligned molecules. *Physical Review A*, 84(5):051404, November 2011.

[4] J. Adachi, S. Motoki, N. A. Cherepkov, and A. Yagishita. Characterization of ushape resonance in the C 1s ionization continuum of CO2molecules. *Journal of Physics B: Atomic, Molecular and Optical Physics*, 35(24):5023–5033, December 2002.

[5] J. Cooper and R. N. Zare. Angular Distribution of Photoelectrons. *The Journal of Chemical Physics*, 48(2):942–943, January 1968.

[6] J. L. Hall and M. W. Siegel. Angular Dependence of the Laser Photodetachment of the Negative Ions of Carbon, Oxygen, and Hydrogen. *The Journal of Chemical Physics*, 48(2):943–945, January 1968.

[7] S. Yang and A. M. Ellis. Helium droplets: a chemistry perspective. *Chemical Society Reviews*, 42(2):472–484, December 2012.

[8] M. Y. Choi, G. E. Douberly, T. M. Falconer, W. K. Lewis, C. M. Lindsay, J. M. Merritt, P. L. Stiles, and R. E. Miller. Infrared spectroscopy of helium nanodroplets: novel methods for physics and chemistry. *International Reviews in Physical Chemistry*, 25(1):15, 2006.

[9] J. P. Toennies and A. F. Vilesov. Superfluid Helium Droplets: A Uniquely Cold Nanomatrix for Molecules and Molecular Complexes. *Angewandte Chemie International Edition*, 43(20):2622–2648, May 2004.

[10] A. Braun. *Photodissociation studies of CH_3I and CF_3I in fluid ^{4}Helium nanodroplets*. PhD thesis, École Polytechnique Fédérale de Lausanne, 2004.

[11] R. E. Grisenti and J. P. Toennies. Cryogenic Microjet Source for Orthotropic Beams of Ultralarge Superfluid Helium Droplets. *Physical Review Letters*, 90(23):234501, June 2003.

[12] J. Harms, J. P. Toennies, and F. Dalfovo. Density of superfluid helium droplets. *Physical Review B*, 58(6):3341, 1998.

[13] F. Ancilotto, P. B. Lerner, and M. W. Cole. Physics of solvation. *Journal of Low Temperature Physics*, 101(5-6):1123–1146, December 1995.

[14] C. Stark and V. V. Kresin. Critical sizes for the submersion of alkali clusters into liquid helium. *Physical Review B*, 81(8):085401, February 2010. Publisher: American Physical Society.

[15] F. Stienkemeier and A. F. Vilesov. Electronic spectroscopy in He droplets. *The Journal of Chemical Physics*, 115(22):10119, 2001.

[16] D. Verma, R. M. P. Tanyag, S. M. O. O'Connell, and A. F. Vilesov. Infrared spectroscopy in superfluid helium droplets. *Advances in Physics: X*, 4(1):1553569, January 2019.

[17] M. Y. Choi and R. E. Miller. Four Tautomers of Isolated Guanine from Infrared Laser Spectroscopy in Helium Nanodroplets. *Journal of the American Chemical Society*, 128(22):7320–7328, June 2006.

[18] A. Lindinger, J. P. Toennies, and A. F. Vilesov. High resolution vibronic spectra of the amino acids tryptophan and tyrosine in 0.38 K cold helium droplets. *The Journal of Chemical Physics*, 110(3):1429–1436, January 1999.

[19] K. Nauta and R. E. Miller. Nonequilibrium Self-Assembly of Long Chains of Polar Molecules in Superfluid Helium. *Science*, 283(5409):1895 –1897, March 1999.

[20] N. B. Brauer, S. Smolarek, X. Zhang, W. J. Buma, and M. Drabbels. Electronic Spectroscopy of Aniline Ions Embedded in Helium Nanodroplets. *The Journal of Physical Chemistry Letters*, 2(13):1563–1566, July 2011.

[21] S. Grebenev, J. P. Toennies, and A. F. Vilesov. Superfluidity Within a Small Helium-4 Cluster: The Microscopic Andronikashvili Experiment. *Science*, 279(5359):2083 –2086, March 1998.

[22] L. F. Gomez, E. Loginov, R. Sliter, and A. F. Vilesov. Sizes of large He droplets. *The Journal of Chemical Physics*, 135(15):154201, October 2011.

[23] L. F. Gomez, K. R. Ferguson, J. P. Cryan, C. Bacellar, R. M. P. Tanyag, C. Jones, S. Schorb, D. Anielski, A. Belkacem, C. Bernando, R. Boll, J. Bozek, S. Carron, G. Chen, T. Delmas, L. Englert, S. W. Epp, B. Erk, L. Foucar, R. Hartmann, A. Hexemer, M. Huth, J. Kwok, S. R. Leone, J. H. S. Ma, F. R. N. C. Maia, E. Malmerberg, S. Marchesini, D. M. Neumark, B. Poon, J. Prell, D. Rolles, B. Rudek, A. Rudenko, M. Seifrid, K. R. Siefermann, F. P. Sturm, M. Swiggers, J. Ullrich, F. Weise, P. Zwart, C. Bostedt, O. Gessner, and A. F. Vilesov. Shapes and vorticities of superfluid helium nanodroplets. *Science*, 345(6199):906–909, August 2014.

[24] B. Langbehn, K. Sander, Y. Ovcharenko, C. Peltz, A. Clark, M. Coreno, R. Cucini, M. Drabbels, P. Finetti, M. Di Fraia, L. Giannessi, C. Grazioli, D. Iablonskyi, A. C. LaForge, T. Nishiyama, V. Oliver Álvarez de Lara, P. Piseri, O. Plekan, K. Ueda, J. Zimmermann, K. C. Prince, F. Stienkemeier, C. Callegari, T. Fennel, D. Rupp, and T. Möller. Three-Dimensional Shapes of Spinning Helium Nanodroplets. *Physical Review Letters*, 121(25):255301, December 2018.

[25] D. M. Brink and S. Stringari. Density of states and evaporation rate of helium clusters. *Zeitschrift für Physik D*, 15(3):257–263, 1990.

[26] K. K. Lehmann. Rotation in liquid ^{4}He: Lessons from a highly simplified model. *The Journal of Chemical Physics*, 114(10):4643–4648, March 2001.

[27] F. Ancilotto, M. Barranco, F. Coppens, J. Eloranta, N. Halberstadt, A. Hernando, D. Mateo, and M. Pi. Density functional theory of doped superfluid liquid helium and nanodroplets. *International Reviews in Physical Chemistry*, 36(4):621–707, October 2017.

[28] P. Kapitza. Viscosity of Liquid Helium below the λ-Point. *Nature*, 141(3558), January 1938.

[29] G. P. Bewley, D. P. Lathrop, and K. R. Sreenivasan. SUPERFLUID HELIUM: Visualization of quantized vortices. *Nature*, 441(7093):588–588, June 2006.

[30] O. Ghafur, A. Rouzée, A. Gijsbertsen, W. K. Siu, S. Stolte, and M. J. J. Vrakking. Impulsive orientation and alignment of quantum-state-selected NO molecules. *Nature Physics*, 5(4):289–293, April 2009.

[31] H. Stapelfeldt and T. Seideman. Colloquium: Aligning molecules with strong laser pulses. *Reviews of Modern Physics*, 75(2):543–557, April 2003.

[32] V. Kumarappan, S. S. Viftrup, L. Holmegaard, C. Z. Bisgaard, and H. Stapelfeldt. Aligning molecules with long or short laser pulses. *Physica Scripta*, 76(3):C63, 2007.

[33] L. Holmegaard, J. H. Nielsen, I. Nevo, H. Stapelfeldt, F. Filsinger, J. Küpper, and G. Meijer. Laser-Induced Alignment and Orientation of Quantum-State-Selected Large Molecules. *Physical Review Letters*, 102(2):023001, January 2009.

[34] B. Friedrich and D. Herschbach. Alignment and trapping of molecules in intense laser fields. *Physical Review Letters*, 74(23):4623–4626, June 1995.

[35] B. Friedrich and D. Herschbach. Polarization of Molecules Induced by Intense Nonresonant Laser Fields. *The Journal of Physical Chemistry*, 99(42):15686–15693, October 1995.

[36] K. Lin, I. Tutunnikov, J. Qiang, J. Ma, Q. Song, Q. Ji, W. Zhang, H. Li, F. Sun, X. Gong, H. Li, P. Lu, H. Zeng, Y. Prior, I.S. Averbukh, and J. Wu. All-optical field-free three-dimensional orientation of asymmetric-top molecules. *Nature Communications*, 9(1), 2018.

[37] M. Artamonov and T. Seideman. Theory of three-dimensional alignment by intense laser pulses. *The Journal of chemical physics*, 128(15), April 2008.

[38] A. Aspegren Søndergaard. *Understanding Laser-Induced Alignment and Rotation of Molecules Embedded in Helium Nanodroplets*. Thesis, Aarhus University, December 2016.

[39] A. Aspegren Søndergaard, B. Shepperson, and H. Stapelfeldt. Nonadiabatic laser-induced alignment of molecules: Reconstructing $\langle\cos^2\theta\rangle$ directly from $\langle\cos^2\theta_{2\text{d}}\rangle$ by Fourier analysis. *The Journal of Chemical Physics*, 147(1):013905, February 2017.

[40] D. Pentlehner, J. H. Nielsen, L. Christiansen, A. Slenczka, and H. Stapelfeldt. Laser-induced adiabatic alignment of molecules dissolved in helium nanodroplets. *Physical Review A*, 87(6):063401, June 2013.

[41] B. Shepperson, A. S. Chatterley, L. Christiansen, A. A. Søndergaard, and H. Stapelfeldt. Observation of rotational revivals for iodine molecules in helium droplets using a near-adiabatic laser pulse. *Physical Review A*, 97(1):013427, January 2018.

[42] A. S. Chatterley, E. T. Karamatskos, C. Schouder, L. Christiansen, A. V. Jørgensen, Terry Mullins, J. Küpper, and H. Stapelfeldt. Communication: Switched wave packets with spectrally truncated chirped pulses. *The Journal of Chemical Physics*, 148(22):221105, June 2018.

[43] A. S. Chatterley, C. Schouder, L. Christiansen, B. Shepperson, M. Heidemann Rasmussen, and H. Stapelfeldt. Long-lasting field-free alignment of large molecules inside helium nanodroplets. *Nature Communications*, 10(1):1–7, January 2019. Number: 1 Publisher: Nature Publishing Group.

[44] J. G. Underwood, M. Spanner, M. Y. Ivanov, J. Mottershead, B. J. Sussman, and A. Stolow. Switched Wave Packets: A Route to Nonperturbative Quantum Control. *Physical Review Letters*, 90(22):223001, June 2003.

[45] M. Poulsen, E. Péronne, H. Stapelfeldt, C. Z. Bisgaard, S. S. Viftrup, E. Hamilton, and T. Seideman. Nonadiabatic alignment of asymmetric top molecules: Rotational revivals. *The Journal of Chemical Physics*, 121(2):783–791, June 2004.

[46] L. Holmegaard, S. S. Viftrup, V. Kumarappan, C. Z. Bisgaard, H. Stapelfeldt, E. Hamilton, and T. Seideman. Control of rotational wave-packet dynamics in asymmetric top molecules. *Physical Review A*, 75(5):051403, May 2007.

[47] S. Guérin, A. Rouzée, and E. Hertz. Ultimate field-free molecular alignment by combined adiabatic-impulsive field design. *Physical Review A*, 77(4):041404, April 2008.

[48] K. L. Reid. Accessing the molecular frame through strong-field alignment of distributions of gas phase molecules. *Phil. Trans. R. Soc. A*, 376(2115):20170158, March 2018.

[49] E. O. Lawrence and M. A. Chaffee. On the Direction of Emission of Photoelectrons from Potassium Vapor by Ultraviolet Light. *Physical Review*, 36(6):1099–1100, September 1930.

[50] A. Sommerfeld. *Atombau und Spektrallinien: Wellenmechanischer Ergänzungsband*, pages 211–213. F. Vieweg & Sohn AG, 1929.

[51] A. Yagishita. Photoelectron angular distributions from single oriented molecules: Past, present and future. *Journal of Electron Spectroscopy and Related Phenomena*, 200:247–256, April 2015.

[52] D. Dill. Fixed-molecule photoelectron angular distributions. *The Journal of Chemical Physics*, 65(3):1130–1133, August 1976.

[53] N. Chandra. Photoelectron spectroscopic studies of polyatomic molecules. I. Theory. *Journal of Physics B: Atomic and Molecular Physics*, 20(14):3405–3415, July 1987. Publisher: IOP Publishing.

[54] J. G. Underwood and K. L. Reid. Time-resolved photoelectron angular distributions as a probe of intramolecular dynamics: Connecting the molecular frame and the laboratory frame. *The Journal of Chemical Physics*, 113(3):1067–1074, July 2000. Publisher: American Institute of Physics.

[55] R. Dörner, V. Mergel, O. Jagutzki, L. Spielberger, J. Ullrich, R. Moshammer, and H. Schmidt-Böcking. Cold Target Recoil Ion Momentum Spectroscopy: a "momentum microscope" to view atomic collision dynamics. *Physics Reports*, 330(2):95–192, June 2000.

[56] J. B. Williams, C. S. Trevisan, M. S. Schöffler, T. Jahnke, I. Bocharova, H. Kim, B. Ulrich, R. Wallauer, F. Sturm, T. N. Rescigno, A. Belkacem, R. Dörner, Th. Weber, C. W. McCurdy, and A. L. Landers. Imaging Polyatomic Molecules in Three Dimensions Using Molecular Frame Photoelectron Angular Distributions. *Physical Review Letters*, 108(23):233002, June 2012.

[57] A. Rouzée, F. Kelkensberg, W. K. Siu, G. Gademann, R. R. Lucchese, and M. J. J. Vrakking. Photoelectron kinetic and angular distributions for the ionization of aligned molecules using a HHG source. *Journal of Physics B: Atomic, Molecular and Optical Physics*, 45(7):074016, March 2012.

[58] A. Rouzée, A. G. Harvey, F. Kelkensberg, D. Brambila, W. K. Siu, G. Gademann, O. Smirnova, and M. J. J. Vrakking. Imaging the electronic structure of valence orbitals in the XUV ionization of aligned molecules. *Journal of Physics B: Atomic, Molecular and Optical Physics*, 47(12):124017, June 2014.

[59] M. Kazama, T. Fujikawa, N. Kishimoto, T. Mizuno, J. Adachi, and A. Yagishita. Photoelectron diffraction from single oriented molecules: Towards ultrafast structure determination of molecules using x-ray free-electron lasers. *Physical Review A*, 87(6):063417, June 2013.

[60] F. Heiser, O. Geßner, J. Viefhaus, K. Wieliczek, R. Hentges, and U. Becker. Demonstration of Strong Forward-Backward Asymmetry in the C1s Photoelectron Angular Distribution from Oriented CO Molecules. *Physical Review Letters*, 79(13):2435–2437, September 1997.

[61] L. Holmegaard, J. L. Hansen, Line Kalhøj, S. L. Kragh, H. Stapelfeldt, F. Filsinger, J. Küpper, G. Meijer, D. Dimitrovski, M. Abu-samha, C. P. J. Martiny, and L. Bojer Madsen. Photoelectron angular distributions from strong-field ionization of oriented molecules. *Nature Physics*, 6(6):428–432, June 2010.

[62] J. L. Hansen, H. Stapelfeldt, D. Dimitrovski, M. Abu-samha, C. P. J. Martiny, and L. Bojer Madsen. Time-Resolved Photoelectron Angular Distributions from Strong-Field Ionization of Rotating Naphthalene Molecules. *Physical Review Letters*, 106(7):073001, February 2011.

[63] J. Maurer, D. Dimitrovski, L. Christensen, L. Bojer Madsen, and H. Stapelfeldt. Molecular-Frame 3d Photoelectron Momentum Distributions by Tomographic Reconstruction. *Physical Review Letters*, 109(12):123001, September 2012.

[64] D. Dimitrovski, J. Maurer, H. Stapelfeldt, and L. B. Madsen. Strong-field ionization of three-dimensionally aligned naphthalene molecules: orbital modification and imprints of orbital nodal planes. *Journal of Physics B: Atomic, Molecular and Optical Physics*, 48(24):245601, 2015.

[65] M. P. Strand, J. Hansen, R.-L. Chien, and R. S. Berry. Influence of nuclear spin on angular distribution and polarization of photoelectrons: resonant two-photon ionization of Na. *Chemical Physics Letters*, 59(2):205–209, November 1978.

[66] T. Seideman. TIME-RESOLVED PHOTOELECTRON ANGULAR DISTRIBUTIONS: Concepts, Applications, and Directions. *Annual Review of Physical Chemistry*, 53(1):41–65, 2002.

[67] J. A. Duncanson, M. P. Strand, A. Lindgård, and R. S. Berry. Angular Distributions of Electrons from Resonant Two-Photon Ionization of Sodium. *Physical Review Letters*, 37(15):987–990, October 1976.

[68] C. Z. Bisgaard, O. J. Clarkin, G. Wu, A. M. D. Lee, O. Geßner, C. C. Hayden, and A. Stolow. Time-Resolved Molecular Frame Dynamics of Fixed-in-Space CS2 Molecules. *Science*, 323(5920):1464–1468, March 2009.

[69] K. L. Reid, T. A. Field, M. Towrie, and P. Matousek. Photoelectron angular distributions as a probe of alignment evolution in a polyatomic molecule: Picosecond time- and angle-resolved photoelectron spectroscopy of S1 para-difluorobenzene. *The Journal of Chemical Physics*, 111(4):1438–1445, July 1999. Publisher: American Institute of Physics.

[70] P. Hockett, C. Z. Bisgaard, O. J. Clarkin, and A. Stolow. Time-resolved imaging of purely valence-electron dynamics during a chemical reaction. *Nature Physics*, 7(8):612–615, August 2011.

[71] Pubchem. Nitrogen. https://pubchem.ncbi.nlm.nih.gov/compound/947. Accessed: 2018-06-07.

[72] Pubchem. Carbon dioxide. https://pubchem.ncbi.nlm.nih.gov/compound/280. Accessed: 2018-06-07.

[73] J. H. Moore, C. C. Davis, and M. A. Coplan. *Building scientific apparatus*. Addison-Wesley Publishing Company, 1989.

[74] J. Brunet and K. E. Gubbins. Viscosity of binary liquid mixtures near the critical mixing point. *Transactions of the Faraday Society*, 65:1255, 1969.

[75] William J. Schmitt and Robert C. Reid. Solubility of monofunctional organic solids in chemically diverse supercritical fluids. *Journal of Chemical & Engineering Data*, 31(2):204–212, April 1986.

[76] Sumitomo Heavy Industries. Sumitomo Heavy Industries cryocooler product catalog. http://www.shicryogenics.com/wp-content/uploads/2019/08/Cryocooler_Product_Catalogue.pdf. Accessed: 2019-08-20.

[77] The Engineering Toolbox. Thermal conductivity of common materials and gases. https://www.engineeringtoolbox.com/thermal-conductivity-d_429.html. Accessed: 2018-06-08.

[78] Pubchem. Acetylene. https://pubchem.ncbi.nlm.nih.gov/compound/6326. Accessed: 2018-06-07.

[79] El-Mul Technologies Ltd. Double MCP 50 datasheet.

[80] Individual manufacturer. Technical information about the pump. Individual label on each pump. Accessed: 2018-06-06.

[81] Ideal Vacuum products. Edwards EH-500 EH500 blower roots vacuum booster pump - rebuilt. https://www.idealvac.com/product.asp?pid=2591. Accessed: 2018-06-04.

[82] Edwards Limited. Instruction manual, e2m28 and e2m30 rotary vacuum pumps. http://www.idealvac.com/files/ManualsII/Edwards_E2M28_to_E2M30_Users_Instruction_Manual.pdf, 06 2003. Accessed: 2020-04-07.

[83] oerlikon Leybold Vacuum. Turbovac, operating instructions. https://www.ajvs.com/library/Oerlikon_Leybold_TURBOVAC_Manual.pdf, 12 2006. Accessed: 2020-04-07.

[84] Pfeiffer Vacuum. Duo 65 M, 3-phase motor, 3TF, 230/400 V, 50 Hz; 265/460 V, 60 Hz. https://www.pfeiffer-vacuum.com/productPdfs/PKD46035.en.pdf. Accessed: 2020-04-07.

[85] Edwards Limited. Instruction Manual, EH Mechanical Booster Pumps. http://www.idealvac.com/files/manualsII/Edwards_EH_Mechanical_Booster_Pump.pdf, 09 2000. Accessed: 2020-04-07.

[86] oerlikon Leybold Vacuum. Trivac b d 16 b / d25 b. http://www.idealvac.com/files/manuals/Leybold_TRIVAC_D16B-D25B_Operating_Instruction_Manual_2.PDF, 07 2011. Accessed: 2020-04-07.

[87] A. Franzen. Component library. http://www.gwoptics.org/ComponentLibrary/. Accessed: 2020-04-07.

[88] Light Conversion. Optics toolbox. http://toolbox.lightcon.com/tools/SFG/. Accessed: 2020-04-07.

[89] D. W. Chandler and P. L. Houston. Two-dimensional imaging of state-selected photodissociation products detected by multiphoton ionization. *The Journal of Chemical Physics*, 87(2):1445–1447, July 1987.

[90] A. T. J. B. Eppink and D. H. Parker. Velocity map imaging of ions and electrons using electrostatic lenses: Application in photoelectron and photofragment ion imaging of molecular oxygen. *Review of Scientific Instruments*, 68(9):3477–3484, September 1997.

[91] C. Vallance. Multi-mass velocity-map imaging studies of photoinduced and electron-induced chemistry. *Chemical Communications*, 55(45):6336–6352, May 2019. Publisher: The Royal Society of Chemistry.

[92] B. Dick. Inverting ion images without Abel inversion: maximum entropy reconstruction of velocity maps. *Physical Chemistry Chemical Physics*, 16(2):570–580, December 2013. Publisher: The Royal Society of Chemistry.

[93] G. M. Roberts, J. L. Nixon, J. Lecointre, E. Wrede, and J. R. R. Verlet. Toward real-time charged-particle image reconstruction using polar onion-peeling. *Review of Scientific Instruments*, 80(5):053104, May 2009. Publisher: American Institute of Physics.

[94] Natan. Polaronionpeeling, github. https://www.github.com/adinatan/PolarOnionPeeling. Accessed: 2020-04-07.

[95] NIST. iodine in the nist data webbase. https://webbook.nist.gov/cgi/inchi?ID=C14362448&Mask=20. Accessed: 2020-04-07.

[96] NIST. Energy levels of iodine in the nist data webbase. url-https://physics.nist.gov/PhysRefData/Handbook/Tables/iodinetable5.htm. Accessed: 2020-04-07.

[97] T. Ebata, C. Minejima, and N. Mikami. A New Electronic State of Aniline Observed in the Transient IR Absorption Spectrum from S1 in a Supersonic Jet. *The Journal of Physical Chemistry A*, 106(46):11070–11074, November 2002.

[98] X. Song, M. Yang, E. R. Davidson, and J. P. Reilly. Zero kinetic energy photoelectron spectra of jet-cooled aniline. *The Journal of Chemical Physics*, 99(5):3224–3233, September 1993.

[99] J. Lin and W. Tzeng. Mass analyzed threshold ionization of deuterium substituted isotopomers of aniline and p-fluoroaniline: Isotope effect and site-specific electronic transition. *The Journal of Chemical Physics*, 115:743–751, July 2001.

[100] T. M. Korter, D. R. Borst, C. J. Butler, and D. W. Pratt. Stark Effects in Gas-Phase Electronic Spectra. Dipole Moment of Aniline in Its Excited S1 State. *Journal of the American Chemical Society*, 123(1):96–99, January 2001.

[101] B. N. Rajasekhar, A. Veeraiah, K. Sunanda, and B. N. Jagatap. Excited states of aniline by photoabsorption spectroscopy in the 30000 - 90000 cm^{-1} region using synchrotron radiation. *The Journal of Chemical Physics*, 139(6):064303, August 2013.

[102] Z. Qu, Z. Qin, X. Zheng, H. Wang, G. Yao, X. Zhang, and Z. Cui. Slow-electron velocity-map imaging study of aniline via resonance-enhanced two-photon ionization method. *Spectrochimica Acta Part A: Molecular and Biomolecular Spectroscopy*, 173:432–438, February 2017.

[103] R. Montero, Á. P. Conde, V. Ovejas, R. Martínez, F. Castaño, and A. Longarte. Ultrafast dynamics of aniline in the 294-234 nm excitation range: The role of the $\pi\sigma^*$ state. *The Journal of Chemical Physics*, 135(5):054308, August 2011. Publisher: American Institute of Physics.

[104] R. Spesyvtsev, O. M. Kirkby, and H. H. Fielding. Ultrafast dynamics of aniline following 269–238 nm excitation and the role of the S2(π3s/πσ*) state. *Faraday Discussions*, 157(0):165–179, September 2012. Publisher: The Royal Society of Chemistry.

[105] J. O. F. Thompson, R. A. Livingstone, and D. Townsend. Following the relaxation dynamics of photoexcited aniline in the 273-266 nm region using time-resolved photoelectron imaging. *The Journal of Chemical Physics*, 139(3):034316, July 2013.

[106] E. Drougas, J. Philis, and A. Kosmas. Ab initio study of the structure of aniline in the s1 and s2 ππ* states. *Journal of Molecular Structure THEOCHEM*, 758:17, 01 2006.

[107] CCCBDB polarizablilty calculation results, aniline. https://cccbdb.nist.gov/polcalc3x.asp?method=8&basis=17. Accessed: 2020-04-07.

[108] CCCBDB calculated rotational constants, aniline. https://cccbdb.nist.gov/rotcalc2x.asp. Accessed: 2020-04-07.

[109] Avantes. Starline spectrometer. https://www.avantes.com/products/spectrometers/starline/item/208-avaspec-uls2048-starline-versatile-fiber-optic-spectrometer. Accessed: 2020-04-07.

[110] J. Arlt, D. Singh, J. O.F. Thompson, A. S. Chatterley, P. Hockett, H. Stapelfeldt, and K. L. Reid. Photoelectron angular distributions from resonant two-photon ionization of adiabatically aligned aniline and naphthalene molecules. *working title, in preparation*, 2020.

[111] F. A. Gianturco, R. R. Lucchese, and N. Sanna. Calculation of low-energy elastic cross sections for electron-CF4 scattering. *The Journal of Chemical Physics*, 100(9):6464–6471, May 1994.

[112] A. P. P. Natalense and R. R. Lucchese. Cross section and asymmetry parameter calculation for sulfur 1s photoionization of SF6. *The Journal of Chemical Physics*, 111(12):5344–5348, September 1999.

[113] P. Hockett. ePolyScat collected results. https://osf.io/psjxt/wiki/aniline/. Accessed: 2020-04-07.

[114] P. Hockett. post-processing for ePolyScat. https://figshare.com/articles/ePSproc_Post-processing_for_ePolyScat_v1_0_0_/3545639. Accessed: 2020-04-07.

[115] H. B. Klevens and J. R. Platt. Spectral Resemblances of Cata-Condensed Hydrocarbons. *The Journal of Chemical Physics*, 17(5):470–481, May 1949. Publisher: American Institute of Physics.

[116] P. A. Clark, F. Brogli, and E. Heilbronner. The π-Orbital Energies of the Acenes. *Helvetica Chimica Acta*, 55(5):1415–1428, 1972.

[117] M. Stockburger, H. Gattermann, and W. Klusmann. Spectroscopic studies on naphthalene in the vapor phase. I. Fluorescence spectra from single vibronic levels. *The Journal of Chemical Physics*, 63(10):4519, September 1975. Publisher: American Institute of Physics.

[118] S. M. Beck, D. E. Powers, J. B. Hopkins, and R. E. Smalley. Jet-cooled naphthalene. I. Absorption spectra and line profiles. *The Journal of Chemical Physics*, 73(5):2019–2028, September 1980.

[119] B. Dick and G. Hohlneicher. Two-photon spectroscopy of the low-lying singlet states of naphthalene and acenaphthene. *Chemical Physics Letters*, 84(3):471–478, December 1981.

[120] D. E. Cooper, R. P. Frueholz, C. M. Klimcak, and J. E. Wessel. Resonance-enhanced two-photon ionization spectra of naphthalene. *The Journal of Physical Chemistry*, 86(25):4892–4897, December 1982. Publisher: American Chemical Society.

[121] A. Hiraya, Y. Achiba, N. Mikami, and K. Kimura. Vibrationally resolved photoelectron spectra of jet-cooled naphthalene: Intramolecular relaxation processes in S1 and S2 states. *The Journal of Chemical Physics*, 82(4):1810–1817, February 1985.

[122] M. C. R. Cockett, H. Ozeki, K. Okuyama, and K. Kimura. Vibronic coupling in the ground cationic state of naphthalene: A laser threshold photoelectron [zero kinetic energy (ZEKE)-photoelectron] spectroscopic study. *The Journal of Chemical Physics*, 98(10):7763–7772, May 1993.

[123] CCCBDB calculated rotational constants, napthalene. https://cccbdb.nist.gov/rotcalc2x.asp. Accessed: 2020-04-07.

[124] CCCBDB polarizability calculation results, naphthalene. https://cccbdb.nist.gov/polcomp2x.asp. Accessed: 2020-04-07.

[125] E. Loginov, D. Rossi, and M. Drabbels. Photoelectron Spectroscopy of Doped Helium Nanodroplets. *Physical Review Letters*, 95(16):163401, October 2005. Publisher: American Physical Society.

[126] NIST. Gas phase energetics data of anthracene. https://webbook.nist.gov/cgi/cbook.cgi?ID=C120127&Mask=20#Ion-Energetics. Accessed: 2020-04-07.

[127] NIST. Gas phase energetics data of tetracene. https://webbook.nist.gov/cgi/cbook.cgi?ID=C92240&Mask=20#Ion-Energetics. Accessed: 2020-04-07.